

SPECTROSCOPY OF MOLECULAR IONS IN COULOMB CRYSTALS

A Thesis
Presented to
The Academic Faculty

by

René Rugango

In Partial Fulfillment
of the Requirements for the Degree
Doctor of Philosophy in the
School of Chemistry and Biochemistry

Georgia Institute of Technology
December, 2016

Copyright © 2016 by René Rugango

SPECTROSCOPY OF MOLECULAR IONS IN COULOMB CRYSTALS

Approved by:

Professor Joseph E. PERRY,
Committee Chair
School of Chemistry and
Biochemistry
Georgia Institute of Technology

Professor Facundo FERNANDEZ
School of Chemistry and
Biochemistry
Georgia Institute of Technology

Professor Kenneth R. BROWN,
Advisor
School of Chemistry and
Biochemistry
Georgia Institute of Technology

Professor Michael CHAPMAN
School of Physics
Georgia Institute of Technology

Professor Thomas ORLANDO
School of Chemistry and
Biochemistry
Georgia Institute of Technology

Date Approved: October 21, 2016

To The One,

*“.....in whom are hidden all the treasures of wisdom and
knowledge.”*

ACKNOWLEDGEMENTS

When I first came to Georgia Tech I wanted to become a theoretical chemist and had my mind made up. I had never heard of "ion trapping" or "laser cooling". Four years later, I have led, completed, and contributed to multiple projects in experimental atomic and molecular physics thanks to:

Ken Brown, my boss and mentor, who advised me to try experiments when I initially wanted to do theory. Thanks for the chance to work in your group and for your abounding patience. Every interaction I have had with you has been positive and most importantly a great learning experience.

Gang Shu, another mentor and friend, who taught me a lot of physics and how to do experiments in a non-'ghetto' way. Thanks for your programming and technical contributions to my experiments and also for your rides to Costco.

Aaron Calvin, who worked with me on the spectroscopy of CaH^+ ions and the first graduate student I ever mentored. Aaron has also been a great friend whose dedication and work ethic I admire. Thanks for being kind enough to offer me a ride home every day after work.

Smitha Janardan, who helped us with theoretical calculations and the most social person in the group.

My undergraduate mentees especially Thomas Dixon and Mudit Sinhal

who greatly contributed to the work presented in this thesis and unfortunately didn't come to Georgia Tech as graduate students in our group. I wish you guys much success in your graduate work.

John Condoluci, who also contributed a lot to our spectroscopy experiments and taught me much about American culture (things like SpongeBob). Thanks for being cheerful and for always bringing a different perspective to our non-scientific discussions in the lab.

Other group members especially Mauricio Gutierrez, Jyothi Saraladevi and Kisra Egodapitiya who proofread this document, Colin Trout, Natalie Brown, Muyuan Li, Pak Hong (James) Leung, and Piero Chiapina.

Group veterans particularly James Goeders, True Merrill, Graham Vitorini, and Ncamiso Khanyile for their encouragement and advice when I first joined the group, and Chingiz Kabytaev for organizing social events that brought us all together.

My mom, Laurence Uwimana who raised me during hard times, went hungry so I could eat, and the reason I ever became a good student. Thanks for taking me to school young despite dad's objections.

My dad, Sylvain Kayisharaza, my mentor and hero who taught me to believe in myself, to love people and most importantly God. Thanks for your prayers and for teaching me how to pray. I pray for you every day.

The rest of my family for their prayers, support, and encouragement.

Rosine Dushime, the woman who has unwaveringly loved and supported me. Thanks for understanding when I was too busy and couldn't come visit.

Most importantly, my Savior Jesus Christ, my God, my all, and the one who gave me a brain, talents, and abilities. Thanks for enabling me to study even the tiniest chunk of your creation.

TABLE OF CONTENTS

DEDICATION	iii
ACKNOWLEDGEMENTS	iv
LIST OF TABLES	xi
LIST OF FIGURES	xii
SUMMARY	xxi
I INTRODUCTION	1
1.1 Ion traps	2
1.2 Laser cooling and sympathetic cooling	3
1.3 A new age of molecular spectroscopy	5
1.3.1 New goals	5
1.3.2 New spectroscopy methods	7
1.4 Organization of thesis	9
II ION TRAPPING AND LASER COOLING	10
2.1 Ion trapping	10
2.2 Doppler cooling	11
2.3 Sideband Cooling	13
2.4 Sympathetic cooling	17
III EXPERIMENTAL METHODS	23
3.1 The Khanyile setup	23
3.1.1 The Urabe trap	23
3.1.2 Vacuum system	24

3.2	The improved Goeders setup	25
3.2.1	The Goeder's trap	25
3.2.2	Vacuum system	28
3.2.3	Fluorescence detection and ion imaging	30
3.3	Computer control	32
3.4	Lasers	34
3.5	Trapping of Ca^+ ions and compensation of excess micromotion	37
3.5.1	Vaporization of neutral Ca and beam alignment . . .	37
3.5.2	Compensation for excess micromotion	37
IV	THREE-MODE SIDEBAND COOLING OF A SINGLE	
	$^{40}\text{Ca}^+$ ION	43
4.1	State detection	45
4.2	Optimization of Doppler cooling	45
4.3	Spin polarization	46
4.4	Sideband cooling	46
V	SYMPATHETIC SIDEBAND COOLING OF CaH^+	52
5.1	Trapping of the Coulomb crystal and normal mode measure- ment	52
5.2	Sideband cooling	55
5.3	Sideband cooling results	57
5.4	Summary	58
VI	VIBRONIC SPECTROSCOPY OF CaH^+	60
6.1	Resonance enhanced multi-photon dissociation (REMPD) of CaH^+ ions	62

6.2	The vibronic spectrum	64
6.2.1	Theoretical model for estimation of experimental parameters	68
6.2.2	Experimental spectroscopic constants	70
6.3	Summary	71
VII	TRAPPING AND SYMPATHETIC COOLING OF BORON IONS	75
7.1	Loading and detection of boron ions	76
7.2	Results and Discussion	77
7.3	Summary	85
VIII	CONCLUSIONS, CURRENT AND FUTURE PROJECTS	86
8.1	Vibronic spectroscopy of CaD^+ ions and peak reassignment for CaH^+	87
8.2	Measurement of rovibronic transitions in CaH^+	88
8.2.1	Pulse shaping techniques	88
8.2.2	Rovibronic lines using REMPD	90
8.2.3	The rovibronic spectrum	90
8.2.4	Quantum heating rovibronic spectroscopy	94
8.2.5	Quantum heating using an optical dipole force	96
8.2.6	Rotational cooling of CaH^+ ions	98
8.3	Spectroscopy on BH^+	99
8.3.1	Production of BH^+ molecular ions	99
8.3.2	Laser induced fluorescence	102
APPENDIX A	— ELECTRONIC AND VIBRATIONAL LIFETIMES OF BH^+	107

APPENDIX B — CIRCUIT BOARDS DIAGRAMS	109
REFERENCES	114

LIST OF TABLES

1	Comparison of experimentally measured vibronic transition frequencies, $1\ ^1\Sigma(v=0) \longrightarrow 2\ ^1\Sigma(v')$, and theoretical calculations. Experimental peaks were assigned based on agreement with theoretical predictions. With this assignment, the transition to $v'=0$ was not measured and the experimental value is extrapolated from the measured peaks (Equation 36) . . .	66
2	Table comparing the experimental and theoretical values of the anharmonicity constant as well as the harmonic constant for the $2^1\Sigma$ state of CaH^+ based on fitting Equation 36 to the first five states. The uncertainties are the errors from the fit. We observe good agreement between the experimental and theoretical values for all the constants.	72
3	A table showing the trapping of different ion species by ablation and their occurrence for 10 consecutive loading events. The last column shows how many times a species is observed out of ten motional resonance scans on different crystals. The peak observed between 13.6 and 14.6 amu has not been identified but could correspond to BH_2^+ . The $^{10}\text{B}^+$ isotope appears less frequently and its peak is usually shorter than that of $^{11}\text{B}^+$. The shifts from the predicted peak positions are due to Coulombic interactions between the ions.	80
4	Rotational and distortion constants for vibrational states in $1^1\Sigma$ and $2^1\Sigma$ electronic states. They are determined using a Nelder-Mead Minimization Algorithm [102] to the χ^2 value (difference between theoretical and experimental rovibronic peak positions) using a C++ library [103]. Large variations in deduced distortion constants are observed.	93

LIST OF FIGURES

1	A stability diagram for a linear rf trap is shown. The dark gray region corresponds to stable trapping parameters in the x and y directions. The plot is generated by numerically solving the Mathieu equation using Hill's method documented in Ref. [72]. For our experiments we keep the a parameter at 0 for the trapping and more stability of a wide range of ion masses. The diagram also shows our current parameters for trapping Ca^+ and B^+ ions. Our ability to stably hold Ca^+ ions at such a low Mathieu q value indicates that the residual Mathieu a value is vanishingly small.	19
2	Stability plots for various ion species trapped in our experiments. The trapping region for each ion is under the curve. The plot is generated by numerically solving the Mathieu equation using Hill's method documented in Ref. [72]. The lighter ions have smaller trapping regions than heavier ones. .	20
3	Linear Paul trap with diagonally opposed RF and DC wedge-shaped electrodes and 2 mm diameter. The ions are confined in the $x - y$ plane (transverse plane of the trap) by a RF voltage and along the z -axis (trap axis) by a DC voltage. The DC segments can also be used for further motion and position control of the ions in the trap.	21
4	A $^{40}\text{Ca}^+$ ion pair on a CCD camera is shown.	21
5	Frequency scan of the $\text{S}_{1/2}$ ($m_j = -1/2$) \rightarrow $\text{D}_{5/2}$ ($m_j = -5/2$) in $^{40}\text{Ca}^+$ showing the carrier (ν), the axial sidebands (ω_z) and radial sidebands (ω_x and ω_y). The cross-peaks ($\omega_x - \omega_z$) are also observed.	22
6	A schematic of the Urabe trap is shown. The DC electrodes include three segments that are used for axial confinement of ions and compensation for excess micromotion [79].	24

7	The Goeders ion trap mounted on a steel plate that connects it to the chamber is shown. The RF and DC electrodes are wedge-shaped and have a curvature radius of 0.5 mm. The trap structure is held together by four Macor rods. The small screws visible on each electrode hold them firm onto the Macor rods. The compensation rods are diagonally opposed and span the whole length of the trap. The top one is used for compensation for excess micromotion while the bottom one is grounded. A reversed configuration would also work. The voltages are applied on these rods are in the range of 50 V in magnitude and are relatively high because of the shielding caused by the RF electrodes.	26
8	Schematic representation of the waveform applied on each electrode of the Goeders trap. Voltages on electrodes 5 and 7 confine the ions axially in the trap center and are of different magnitudes due to the asymmetry of the trap. Outer electrodes are used to avoid additional trapping regions. We use low confinement voltages particularly for experiments involving large Coulomb crystals. The middle electrodes are used for compensation for excess micromotion.	28
9	A view of inside the chamber through one of the viewports shows various electrical connections. Female socket contacts were crimped onto Kapton-insulated wires and connected to each trap electrode. The calcium oven is also shown with barrel connectors used to hold the oven and connect it to electrical feedthroughs. The oven consists of a thin stainless steel tube 0.1 in in diameter with 0.002 in thick walls that is crimped on one end and filled with elemental calcium metal through the other end. One wire is wrapped on the open end and the other wire crimped on the closed end. This type of oven provided good collimation of the neutral calcium flux and required lower current.	29

10	The chamber assembly is shown. The main chamber sits on a five way cross that also holds the ion pump, the DC feedthroughs, the titanium sublimation pump, the all-metal valve, and the ion gauge. Kodial glass side viewports used for laser input and additional feedthroughs are connected to the main chamber. The manual leak valve used for as a gas inlet is also shown. The titanium sublimation pump is used occasionally to reduce excess background gas, and the ion pump is kept on all the time to maintain UHV pressures of around 1×10^{-10} Torr. It is connected to a dual ion pump controller which also registers the pressure inside the chamber.	31
11	A schematic shows the fluorescence detection setup. The ions located in trap center emit photons that are collected by the lens stack mounted 5 mm above the top window of the chamber. The lens stack firstly forms the image onto the iris and a $f = 30$ mm lens sends the fluorescence to the PMT and CCD camera through a 397 nm filter.	33
12	The laser system used for ionization of Ca and the laser cooling of Ca^+ ions is shown. Each laser beam is transported to the experiments using an optical fiber.	34
13	The setup used for the spectroscopy of CaH^+ ions and the trapping and detection of B^+ ions is shown. The optics around the chamber combine and steer the beams onto the axial and radial axes of the trap. The helical resonator is used as an amplifier and filter for the RF voltage used to trap ions. The Helmholtz coil on top of the chamber generates a magnetic field of a few Gauss used to split the Zeeman levels in Ca^+ . We use the manual leak valve (Kurt J. Lesker VZLVM267) to add hydrogen to the chamber.	36
14	The neutral Ca fluorescence induced by the 423 nm laser is shown. The Ca oven is run hotter than normal to observe enough fluorescence. Initially, the two beams are aligned to the trap center by moving them vertically and horizontally and finding middle points. The camera is aligned to where the two beam cross, and the trapping of ions can follow. . . .	38

15	The fluorescence signal is recorded as a function of photon arrival time. The PMT data is sampled by a 300 MHz clock synchronized by the RF signal. (a) One can observe unevenness in fluorescence which indicates that there is correlation between the photon arrival time and the RF oscillation. (b) The trap is compensated and there is no correlation between photon arrival time and RF oscillation. (c) As the voltage is decreased past the compensation point, a phase change occurs, and there is correlation between photon arrival time and RF oscillation again. The slow drop-off at the longest times is caused by the fact that the clock speed is at the limit of the FPGA clock.	41
16	A diagram shows the transitions used to Doppler cool and sideband cool Ca^+ . Doppler cooling is achieved by using the 397 nm laser and the 866 nm laser to repump the $D_{3/2}$ metastable state. Sideband cooling takes place on the quadrupole 729 nm transition and uses an 854 nm repumper to bring the ion back into the ground state.	44
17	A histogram shows the fluorescence distribution of a bright ion and a dark ion. Below a given threshold the ion is considered excited to the $D_{5/2}$ state (shelved).	48
18	A Rabi scan on the $4S_{1/2} \rightarrow 3D_{5/2}$ transition carrier fitted to equation 30 is shown. In this scan, Doppler cooling reaches 13 quanta which is low enough to initiate sideband cooling.	49
19	Optical pumping into the $S_{1/2}$ ($m_j = +1/2$) spin state is shown. In this figure, 5 excitation cycles on the $S_{1/2}$ ($m_j = +1/2$) \rightarrow $D_{5/2}$ ($m_j = -3/2$) transition are enough to fully prepare the ion in the desired spin state.	50

20	Measurement of the $S_{1/2} (m_j = -1/2) \rightarrow D_{5/2} (m_j = -5/2)$ first-order sidebands for the $^{40}\text{Ca}^+$ ion by electron shelving. Red and blue sidebands are fit to a Gaussian of the same width but variable amplitude. Comparison of sideband heights yields an average mode occupation of $\bar{n}_z = 0.046 \pm 0.02$ ($T_z = 11.2 \pm 0.003 \mu\text{K}$) for the axial mode and $\bar{n}_x = 0.33 \pm 0.092$ ($T_x = 79.4 \pm 2.3 \mu\text{K}$) as well as $\bar{n}_y = 0.32 \pm 0.025$ ($T_y = 77.0 \pm 5.8 \mu\text{K}$) for the radial modes.	51
21	The experimental setup including the vacuum chamber and the trap is shown. The magnetic field of 1.4 Gauss is perpendicular to the trap axis and the direction of the lasers. DC connections include compensation voltages, endcap voltages, and oven current.	53
22	(a) One $^{40}\text{Ca}^+$ reacts with H_2 to make $^{40}\text{CaH}^+$ which is not fluorescent. (b) The experiment sequence begins by Doppler cooling the two-ion crystal followed by optical pumping and sideband cooling cycles. After sideband cooling, we perform electron shelving measurements on the motional sidebands and detect the atomic state.	54
23	Measurement of the $S_{1/2} (m_j = -1/2) \rightarrow D_{5/2} (m_j = -5/2)$ first-order axial sidebands for the $^{40}\text{Ca}^+ - ^{40}\text{CaH}^+$ crystal by electron shelving. Red and blue sidebands are fit to a Gaussian of the same width but variable amplitude. The hollow circles correspond to the Doppler cooling results, and the full circles are the sideband cooling data. Comparison of sideband heights yields an average mode occupation of $\bar{n}_{\text{COM}} = 0.09 \pm 0.04$ for the center of mass mode and $\bar{n}_{\text{BM}} = 0.06 \pm 0.03$ for the breathing mode.	56

24	The three lowest $^1\Sigma$ potential energy curves for CaH^+ are shown [36]. We measure vibrational lines using resonance enhanced dissociation. The first photon excites the molecules on the $1^1\Sigma \rightarrow 2^1\Sigma$ transition. A second photon could then dissociate the ion. The atomic asymptotes of the plotted molecular potentials lead to Ca^+ in different electronic states and H in the ground state. A simplified Ca^+ energy level diagram shows the states involved in Doppler cooling and how they correspond to the limits of the molecular states (energy not to scale) . The 397 nm laser is the main Doppler cooling laser and the 866 nm laser repumps the metastable $D_{3/2}$ state. . . .	63
25	a) Coulomb crystal containing a few hundred Ca^+ ions react with H_2 to make 50 to 100 CaH^+ ions. The reaction is indicated by the darkening of the left side of the crystal. The asymmetry seen in the Coulomb crystal is due to the 397 nm radiation pressure on Ca^+ ions. b) The pulse sequence used to dissociate the molecular ions is shown. The Doppler cooling lasers remain on to avoid ion heating and losses. An AOM switches the dissociation beam.	64
26	The measured fluorescence recovery curves for excitation at 395.5 nm and 397 nm are shown. The data is fit with a single exponential (Equation 32) and the fluorescence is normalized to the steady-state fluorescence parameter, A_∞ , from the fit. .	65
27	The dissociation rate as a function of excitation wavelength. The error bars are standard deviations over the five measurements. A model that assumes the dissociation rate is limited by the absorption of the first photon is used to plot the theoretical curves and to find the experimental fit. The theory model is based on CASPT2 [31] but all peaks are red shifted by a constant 50 cm^{-1}	67
28	Theoretical and experimental values for $\omega_e x_e$ and ω_e for the the $2^1\Sigma$ state of CaH^+ were calculated by fitting the plotted transition energies for $1^1\Sigma(v=0) \rightarrow 2^1\Sigma(v')$. The <i>ab initio</i> theoretical energies are taken from Ref. [96].	72

29	The experimental setup including the main vacuum chamber and the trap is shown. The The 355 nm YAG minilite II is focused on B target is mounted right next to the Ca target about 40 cm from the trap center. The cooling beams (397 nm and 866 nm)used to Doppler cool the ions enter the trap axially and radially.	78
30	Ion crystals containing about 200 Ca^+ ions with their corresponding motional resonance scans before and after ablation of the boron target. The boron species are located towards the center of the crystal due to a lower mass-to-charge ratio, and the secular frequencies for different ions are inversely proportional to their m/q . The vertical bar are the predicted secular frequencies for each ion. One can observe that the peak positions are within 10% of their predicted values. In this figure, ω_{Ca^+} is set to 0.44 MHz and $q_{\text{B}^+}=0.23$	79
31	Motional excitation scans are depicted for 10 consecutive experiments. For each experiment, a new Ca^+ crystals is loaded and the B target is ablated 10 times. On the y-axis the plots are offset from each other by 0.1 units. The features corresponding to B_3^+ and $^{11}\text{B}^+$ are observed in every scan. The difference in peak heights between different scans stems from the fact that ablation does not allow control over the amount of dark ions loaded in each crystal.	83
32	The motional excitation can change with trapping time. As seen in a) and b), the shoulder feature that we associate with B_2^+ can appear a long time after ablation. This could be either due to dissociation of B_4^+ whose presence is hidden by the Ca^+ line or charge exchange with background gas. The shoulder off the $^{11}\text{B}^+$ peak in a) is compatible with BH^+ but the feature has a short lifetime and is rare. The features corresponding to B^+ and B_3^+ are observed to be relatively stable over thirty minutes.	84

33	Plot used to assign vibronic peaks in both CaH^+ and CaD^+ ions. The red plot is the theoretical spectra adjusted to fit both CaH^+ and CaD^+ vibronic experimental data . The blue plot is the experimental fit. The 687 cm^{-1} shift on the theoretical spectra matches both experimental spectra and is consistent with a reassignment of the vibronic peaks.	88
34	A schematic shows a simplified apparatus for pulse-shaping. An incident pulsed beam with a Gaussian frequency profile is diffracted by a grating, and a cylindrical lens focuses the individual Fourier components onto a slit or mask. A mirror behind the slit reflects the beam back through the lens to the grating, which recombines the frequency components of pulse shaped beam. The position of the slit is moved horizontally along the cross-section of the beam to select narrow frequency components.	91
35	Rovibronic lines within the $v'=0, 1, 2, 3$ vibronic transitions shown with the vibronic spectrum of CaH^+ . The rovibronic spectrum matches well the envelope of the vibronic spectrum.	92
36	Assignment of rovibronic lines within the $v' = 0, 1, 2, 3$ vibronic transitions. The percent error is calculated as $\text{error} = \frac{ \text{experiment} - \text{theory} }{\text{experiment}} \times 100$ and is small for all measured lines. . . .	93
37	A diagram shows the simplified structure that will be used for rotational cooling (not to scale). The ions are excited on the $v = 0, J = 2 \rightarrow v = 1, J = 1$ transition using a $6.9 \mu\text{m}$ laser. The vibrational relaxation puts the ions either in the $v = 0, J = 2$ state or the $v = 0, J = 0$ state, but the $v = 0, J = 2$ gets ultimately depleted because of continuous excitation. Its depletion instigates rotational decay from higher rotational states, and the repeated process puts nearly all the population in the ground rovibrational state. The two 408 nm detection photons are used to measure the population in the $v = 0, J = 0$ state before and after rotational cooling. Bluer vibronic transitions can also be used for detection.	100

38	A scheme for the laser induced fluorescence of BH^+ ions is shown. The main cooling laser is the 379 nm which would continuously excite the ions on the $X^2\Sigma, v = 0, K = 1 \rightarrow A^2\Pi, v = 0, K = 1$. The initial $K = 1$ rotational state is judiciously chosen to avoid rotational branching. The 417 nm laser repumps the $v = 1$ state and the 4 μm laser repopulates the $K = 1$ in case there is decay to any of the even parity states from $v = 1$. The 4 μm laser frequency will also need the same modulation as the 379 nm. This scheme would also result in rotational cooling.	103
39	The rotational population distribution at 300 K in the $X^2\Sigma, v = 0$ state is shown. The quantum number K is the total angular momentum not including the spin of the electron. The population for every state is calculated using a Boltzmann distribution function. The large rotational constant (B) of the BH^+ molecule pushes the poluation distribution to the low-lying states.	105
40	The vibrational and electronic transition lifetimes of the BH^+ molecule are shown. The lifetimes of the X-A vibronic transitions are denoted by τ and the vibrational lifetimes in the X state by τ' [62].	108
41	The amplifier board used for DC voltages on the improved Goeders setup is shown.	110
42	The schematic of the amplifier board used for DC voltages on the improved Goeders setup is shown.	111
43	The board used for injecting the RF voltage for motional resonance experiments is shown.	112
44	The schematic of the board used for injecting the RF voltage for motional resonance experiments is shown.	113

SUMMARY

This thesis presents the results of my graduate work which has concentrated on applying laser-cooling techniques to molecular ions, specifically CaH^+ and BH^+ ions for the study of their rovibronic spectroscopy. The goal of my research has been to control external and internal degrees of freedom of these two ions. Each of these molecules is spectroscopically appealing in its own right. For starters, CaH^+ has been identified as a potential system for the test for the time variation of fundamental constants, and it's also been speculated to be in space. BH^+ has a nearly diagonal Franck-Condon structure, and could be directly laser-cooled using only a few lasers. This structure makes it a good candidate for the cooling of internal molecular degrees of freedom.

Each of the experiments described in this review involves the trapping and laser-cooling of ions. We cool the molecular ions sympathetically with laser-cooled Ca^+ . The probing techniques used to collect data are mainly: laser induced fluorescence, mass spectrometry, and resonance-enhanced multiphoton dissociation (REMPD). We have demonstrated the ground state sympathetic cooling of CaH^+ ion to less than $16\ \mu\text{K}$, and we have used to REMPD to measure for the first time four vibronic transitions in CaH^+ ions. Together, these results are important for future quantum logic experiments on

this molecule.

Furthermore, we have also made some progress towards trapping and cooling BH^+ ions by first trapping B^+ ions with Ca^+ ions. We use the motional resonance method to detect the B^+ ions, which can be reacted with H atoms to produce the molecular ions. Following the measurement of the vibronic spectrum of CaH^+ , we have narrowed the linewidth of the laser source to resolve rotational lines.

CHAPTER I

INTRODUCTION

In 1928, while looking at the afterglow of nitrogen gas, G. Herzberg took the first spectrum of a molecular ion N_2^+ using an electric discharge [1, 2]. Several other emission spectra of molecular ions such as O_2^+ and CO^+ [2] were identified soon after. The initial motive for these measurements had been the possible presence of molecular ions in the interstellar medium and their contribution to the overall chemistry in this region of space, especially the notoriously fast ion-neutral molecule chemical reactions [2]. During this early period of molecular spectroscopy, the low density of molecular ions combined with their short storage times made laboratory measurements of their spectra particularly difficult. Many notable techniques including flash discharges, molecular ion beam spectroscopy, and ion traps emerged as a solution to these problems [2, 3, 4].

Another lifelong challenge posed to molecular spectroscopy is the Doppler shifts and low resolution found in molecular spectra. These barriers become more problematic when it comes to identifying diffuse interstellar bands of molecular ions. The high motional temperature of molecular ions is the main cause of Doppler shifts and broadening. Various cooling methods have been

developed over the past century to address this issue. Early cooling techniques for molecular ions employed liquid nitrogen[5] and noble gas matrices [6] as refrigerants and later included buffer gas cooling[7]. Most recently laser cooling methods which have proven to be the fastest and to reach the coldest temperatures. [8].

This thesis presents the combination of various techniques introduced above and previously used in quantum computation experiments with atomic ions to sympathetically cool CaH^+ ions to their motional ground state and measure their vibronic spectrum for the first time. Additionally, it includes the new results on the trapping and sympathetic cooling of boron and boron cluster ions.

1.1 Ion traps

Following the first invention of the Penning trap in 1936 [9] and of the rf quadrupole mass filter in 1953 [10], ion traps quickly became a powerful tool in atomic and molecular physics experiments. The first experiments on trapped molecular ions were performed by H. G. Dehmelt and coworkers on the storage of millions of H_2^+ molecules in a radiofrequency (rf) trap for several seconds [11]. They achieved three-dimensional trapping of ions using an electric field in which the ions undergo a force proportional to its displacement from the center of the trap. The trap used in these experiments consisted of two hyperbolic disc electrodes separated by 25 mm and held in a cylindrical tantalum mesh electrode. The basic operation principle of this

trap is the same as that of Paul traps used in the experiments reported in this thesis. A thorough explanation of ion trapping concepts will be presented in the next chapter.

Dehmlet's experiments on trapping molecular and atomic ions opened new doors for molecular spectroscopy. Mahan and coworkers dedicated their work to laser-induced fluorescence spectroscopy of various trapped molecular ions such as N_2^+ , CH^+ , CD^+ , CO^+ , BrCN^+ , and 1,3,5-trifluorobenzene cation [12, 13, 14]. These experiments also measured radiative lifetimes of various transitions in those molecules. Fluorescence spectroscopy, however, suffered a great disadvantage: Doppler shifts and broadening caused by the high temperature of trapped ions.

Perhaps one of the most notable advantages of ion trapping experiments has been the ability to co-trap multiple species in the same trap. This property has allowed the indirect cooling of molecular ions to near absolute zero temperatures through their Coulombic interaction with laser-cooled atomic ions. As a result, Doppler-free single molecular ion spectroscopy has become feasible despite the intrinsic difficulty of direct laser-cooling techniques on most molecular ions.

1.2 Laser cooling and sympathetic cooling

The notion that the elimination of first and second-order Doppler shifts was necessary for high resolution spectroscopy drove the development of powerful cooling techniques in the 1970s. Various groups launched new experimental

and theoretical studies on different cooling methods. In 1978, Neuhauser *et al.* [15] and Wineland *et al.* [16] reported the laser-cooling of trapped Ba^+ ions and Mg^+ ions, respectively. The first implementation of the trapping of a localized single Ba^+ ion followed suit in 1980 in the Dehmelt group [17]. Multiple experiments subsequently achieved the laser-cooling of other atomic ions including the cooling of a single ion to the motional ground state [18, 19, 20, 21, 22].

Laser-cooling of ions relies on the damping force experienced by an ion upon the absorption-emission cycle of photons. The implementation of laser-cooling experiments therefore depends on the internal structure of the ion to be cooled. Factors such as the presence of closed transitions, the availability of laser sources, and the linewidth of the transitions determine whether or not an ion is amenable to cooling. Atomic ions are generally the easiest to cool while most molecular ions lack the necessary internal closed transitions. As a result, Doppler-free spectroscopy of molecular ions requires an indirect cooling technique known as sympathetic cooling.

The first sympathetic cooling experiment used laser-cooled Be^+ ions to cool Hg^+ ions through Coulombic collisions. They reached temperatures below 1K [23]. Other atomic ions have also been sympathetically cooled by atomic coolants [24, 25]. The sympathetic cooling trapped ions to mK temperatures where the ions are nearly still, and their separation is much larger than their spatial wavepacket leads to the formation of ordered structures otherwise known as Coulomb crystals [26].

The crystallization of molecular ions is a relatively recent milestone. Baba and Waki demonstrated the non-destructive detection of various sympathetically-cooled molecular ions including H_3O^+ , O_2^+ , NH_4^+ , and C_2H_5^+ [27, 28] using refrigerant Mg^+ atoms. Drewsen and coworkers were the first to crystallize translationally cold MgH^+ ions by sympathetically cooling them with laser-cooled Mg^+ ions [29, 30].

1.3 A new age of molecular spectroscopy

1.3.1 New goals

Cooling methods combined with ion trapping techniques have created a new age of molecular spectroscopy, indeed. The initial motives behind the spectroscopy of molecular ions such as their identification in the interstellar medium and the study of ion-neutral chemical reactions have now become more attainable than ever.

Cryogenic buffer gas cooling of trapped ions have recently helped to unravel various mysteries in molecular ion spectroscopy. For instance, new spectroscopic measurements on trapped bucky ball ions (C_{60}^+) were used to confirm their presence in space [31], a nearly century old mystery for astrochemists. In addition, the elusive structure of CH_5^+ [32] has been recently profiled using measurements of rovibrational lines on the molecule.

For experiments involving laser-cooling and ion trapping techniques, a new level of control of internal quantum state as well as high precision spectroscopy have been created. Reactions between laser-cooled atomic ions and

neutral molecules have been investigated and could further explain the mechanism of ion-neutral reactions taking place in the interstellar medium. The observed reactions have produced various molecular ions such as BeH^+ [33], CaH^+ [34], CaO^+ [35], and MgH^+ [29].

Furthermore, the high precision and low noise spectroscopy afforded by trapped and laser-cooled molecular ions make them promising candidates for measuring the time variation of fundamental physical constants such as the electron-to-proton mass ratio [36, 37]. This constant is dependent upon the rotational and vibrational transitions of molecules according to the following equations:

$$\nu_{\text{rot}} \sim m_e/\mu R_\infty, \quad (1)$$

$$\nu_{\text{vib}} \sim \sqrt{m_e/\mu} R_\infty, \quad (2)$$

where R_∞ is the Rydberg energy and μ is the reduced mass [38, 39]. Rovibrational spectroscopy of crystallized molecular ions was first implemented on HD^+ ions in 2006 [40], and many other molecular ions were investigated thereafter [41, 42].

High precision spectroscopy of molecular ions can also allow the determination of the electron electric dipole moment (eEDM) [43]. In the quest to search for the eEDM, molecular ions such as HfF^+ and ThF^+ are sought after. The molecules possess many important advantages including their low magnetic moment that makes them less sensitive to the magnetic field [44], their large internal electric fields that increase eEDM sensitivity [45, 46], and

long coherence times for high precision spectroscopy [43]. The measurement of the eEDM is necessary for the test of time-reversal violation [47] and for probing physics beyond the Standard Model [48].

1.3.2 New spectroscopy methods

Within the past decade, various new experimental and theoretical methods have revolutionized molecular spectroscopy. The most remarkable results were shown on atomic ions using techniques designed for atomic clocks and quantum information experiments [49, 50]. The precision achieved with quantum logic spectroscopy experiments [51, 52, 53] is very desirable for molecular ion spectroscopy in order to achieve the goals mentioned above. Quantum logic spectroscopy and similar approaches [54, 55, 56, 57, 58] require measuring the change in motional energy by observing the control ion fluorescence after the target ion has been excited. Its implementation on molecular ions requires molecular ions prepared in their motional ground state as well as in a specific internal state. There has been tremendous progress on both fronts. Our group has shown the sympathetic sideband cooling of both axial modes of CaH^+ to their motional ground state. A similar experiment was later done by Wan *et al.* [59]. Furthermore, Wolf *et al.* recently demonstrated non-destructive rovibronic state detection on a single MgH^+ ion prepared in its ground state [60].

Moreover, precision spectroscopy requires molecular ions with internal degrees of freedom prepared in specific states. For specific molecular ions, this

may be achievable by direct laser cooling [61, 62], as has been the case for neutral molecules [63, 64], but for most molecular ions a combination of cooling methods is required. The internal degrees of freedom have been controlled using state-selective photoionization [65], optical pumping [66, 67, 68], buffer gas cooling [69], and sympathetic cooling with laser-cooled neutral atoms [70]. Optical pumping methods have shown the highest cooling efficiency, but they require preliminary knowledge of specific transitions in molecular ions.

For CaH^+ , the biggest challenge for internal quantum state control is the lack of experimental spectroscopic data. We have recently measured for the first time vibronic transitions in CaH^+ using resonance enhanced multiphoton dissociation (REMPD), the same technique that was used to produce new vibrational overtones measurements in this molecule by our group [42].

The cooling of internal states of molecular ions is also limited by the rich rovibrational structure which increases the number of repumping lasers required for direct Doppler cooling and fluorescence detection. BH^+ is one of the few ions that has been identified to have internal structures suited for Doppler cooling with few lasers [62]. We have shown the trapping of B^+ and boron cluster ions produced using laser ablation methods. Our current results are vital to the future spectroscopy on boron clusters and the trapping of BH^+ ions using ablation of NaBH_4 salts.

Overall, all the challenges to the realization of high precision spectroscopy

of molecular ions can be addressed by the ability to cool to the lowest quantum limit both external and internal degrees of freedom. The former has been achieved and there is still some work to be done to reach the latter. Both issues have been the focus of my graduate work, and the results presented in this thesis are an important part of a new prospect for high precision and low noise molecular spectroscopy.

1.4 Organization of thesis

The rest of the thesis is organized as follows. Chapter 2 covers background on cooling and trapping techniques. Chapter 3 gives details on the experimental methods used to gather all the data. Chapter 4 describes our results on three-mode sideband cooling of a single Ca^+ ion. Chapter 5 reports sympathetic sideband cooling of CaH^+ to the motional ground state. Chapter 6 describes our newly measured vibronic transitions in CaH^+ . Chapter 7 presents our results on the trapping and cooling of boron ions, and Chapter 8 summarizes the work and discusses current and future experiments.

CHAPTER II

ION TRAPPING AND LASER COOLING

2.1 Ion trapping

Charged particles can be confined in on an axis or a point in space when moving in a parabolic potential which behaves quadratically in cartesian coordinates for an electric quadrupole field [71]:

$$\Phi = \frac{\Phi_o}{r^2}(\alpha x^2 + \beta y^2 + \gamma z^2). \quad (3)$$

For the charged particle to be trapped at a potential null, the Laplacian condition ($\Delta\Phi = 0$) has to be satisfied which means:

$$\alpha + \beta + \gamma = 0 \quad (4)$$

The solution to the equation above yields at least two dimensions having different signs of potential. This configuration makes it impossible for ions to be stably trapped solely with static fields because while they can oscillate harmonically along one axis, their energy will increase exponentially in one of the other dimensions leading to ion loss. This restriction can be addressed by using an oscillating field ($\Phi_o = U + V \cos \omega t$) in the x and y dimensions in which case the equations of motion are governed by Matthieu's differential equations:

$$\frac{d^2x}{d\xi^2} + (a + 2q \cos 2\xi)x = 0, \quad (5)$$

$$\frac{d^2y}{d\xi^2} - (a + 2q \cos 2\xi)y = 0, \quad (6)$$

where the q and a factors are shown below:

$$a = \frac{4QU}{mr_0^2\Omega_{RF}^2}, q = \frac{2QV}{mr_0^2\Omega_{RF}^2}. \quad (7)$$

The variable Q is the charge of the ion while V is the RF amplitude, and U is the DC bias applied to the RF electrodes. The RF frequency also called trap frequency is denoted Ω_{RF} ; m is the mass of the ion, and r_0 is the trap radius.

The values of the a and q parameters determine the conditions in which ions can travel along the z -axis in stable motion, and further confinement along the z -axis can be achieved with an additional static field. Therefore, by tuning the RF potential V and the DC bias U , the ions can be mass-filtered in the trap. In our experiments, no DC bias is applied to the RF electrodes ($a = 0$) so as to permit the trapping of wide range of masses. A stability diagram is shown in figure 2.

2.2 *Doppler cooling*

In 1978, Neuhauser *et al.* [15] detected the resonance fluorescence of a few tens of Ba^+ ions in a rf quadrupole ion trap. The same year, Wineland *et al.*[16] implemented a similar experiment on the Doppler cooling of Mg^{2+} ions confined in a Penning trap reaching mK temperatures. The basics of Doppler cooling can be described using a semi-classical picture that treats the ions trapped in a rf quadrupole trap as harmonic oscillators unaffected by the

fast-driven motion of the RF field also called micromotion. In this case, the velocity of the ion ($v = v_o \cos \omega t$) changes on a much shorter timescale than the absorption-emission cycle of photons by the ions ($\omega \ll \Gamma$) [73]. For an ion oscillating in the trap at room temperature, the absorption of a photon induces a momentum kick on the ion while the averaged momentum transfer for the emission process is zero. As a result, the ion experiences a continuous drag along the wave vector of the laser beam which effectively lowers the ion's velocity.

The radiation force induced on the ion can be expressed as follows:

$$F = \hbar k \Gamma \rho_{ee}, \quad (8)$$

where Γ is the linewidth of the transition, and ρ_{ee} is the absorption probability given by:

$$\rho_{ee} = \frac{s/2}{1 + s + (2\delta_{eff}/\Gamma)^2}, \quad (9)$$

where s is the saturation parameter dependent upon the Rabi frequency (Ω) of the transition. The $\delta_{eff} = \delta - k \cdot v$ parameter is the effective detuning from the transition resonance. It combines the detuning of the laser from the transition wavelength, $\delta = \nu - \nu_o$ and the Doppler shift, $-k \cdot v$. The damping force experienced by the ion is maximized at $\delta_{eff} = \Gamma/2$, and the lowest achievable temperature through Doppler cooling is given in the following equation [74]:

$$T_D = \hbar \Gamma / 2 \quad (10)$$

In case of substantial micromotion where the ion is not located at the pseudopotential minimum, a combination of DC potentials can be used to bring it back to the RF null. Details on compensation of excess micromotion are presented in section 15.

2.3 *Sideband Cooling*

The Hamiltonian of an ion interacting with laser radiation can be written as:

$$H = H_o + H', \quad (11)$$

where H_o is the unperturbed Hamiltonian of the ion which can be written as:

$$H_o = \frac{p^2}{2m} + \frac{m\omega^2 x^2}{2} + \frac{1}{2}\hbar\nu_i\sigma_z. \quad (12)$$

In equation 12, the first two terms describing the kinetic and potential energies can be rewritten using raising and lowering operators (Hamiltonian for a harmonic oscillator), and the third term represents the energy of an internal state of an atom. For a two-level state system of an atom with energy levels $|a\rangle$ and $|b\rangle$, H_o can be expressed as follows [75]:

$$H_o = \hbar\omega(aa^\dagger + \frac{1}{2}) + \frac{1}{2}(|a\rangle\langle a|\hbar\nu_a + |b\rangle\langle b|\hbar\nu_b), \quad (13)$$

where ω is the secular frequency of the ion in the trap, and a and a^\dagger are the lowering and raising operators respectively. The part of the Hamiltonian describing the ion-laser interaction can be expressed as:

$$H' = \hbar\Omega\sigma_x(e^{i(kx-\nu_L t)} + e^{-i(kx-\nu_L t)}), \quad (14)$$

where $\Omega = \mu E/\hbar$ is the Rabi frequency of the transition, and $\sigma_x = \sigma + \sigma^\dagger \equiv |a\rangle\langle b| + |b\rangle\langle a|$ is the transition operator. By taking into account the time evolution of the internal states, we can use the interaction picture generated by H_o to write the interaction Hamiltonian as:

$$H_I = e^{iH_o t/\hbar} H' e^{-iH_o t/\hbar}. \quad (15)$$

The propagator in the above equation can take the form:

$$U_o = (e^{-i\nu_a t}|a\rangle\langle a| + e^{-i\nu_b t}|b\rangle\langle b|)(e^{-i\hbar\omega(aa^\dagger + \frac{1}{2})}) \quad (16)$$

upon using the eigendecomposition of the H_o matrix ($f(A) = Qf(\Lambda)Q^{-1}$, where Λ is a diagonal matrix). By combining the last three equations we can express H_I as:

$$H_I = \hbar\Omega(e^{i\hbar\omega(aa^\dagger + \frac{1}{2})})(e^{i\nu_a t}|a\rangle\langle a| + e^{i\nu_b t}|b\rangle\langle b|) \times (e^{i(kx - \nu_L t)} + e^{-i(kx - \nu_L t)}) \times (|a\rangle\langle b| + |b\rangle\langle a|)(e^{-i\nu_a t}|a\rangle\langle a| + e^{-i\nu_b t}|b\rangle\langle b|)(e^{-i\hbar\omega(aa^\dagger + \frac{1}{2})}). \quad (17)$$

The equation above yields:

$$H_I = \hbar\Omega(e^{i\hbar\omega(aa^\dagger + \frac{1}{2})})(e^{ikx}e^{-i(\nu + \nu_L)t}|a\rangle\langle b| + e^{-ikx}e^{-i\Delta\nu t}|a\rangle\langle b| + e^{-ikx}e^{i(\nu + \nu_L)t}|b\rangle\langle a| + e^{ikx}e^{i\Delta\nu t}|b\rangle\langle a|)(e^{-i\hbar\omega(aa^\dagger + \frac{1}{2})}), \quad (18)$$

where $\nu = \nu_b - \nu_a$ is the transition frequency and $\Delta\nu = \nu - \nu_L$ is the detuning of the laser from the transition resonance frequency. The terms in $e^{i(\nu + \nu_L)t}$ oscillate too fast and can be neglected (rotating wave approximation), and the expression for H_I then becomes:

$$H_I = \hbar\Omega(e^{i\hbar\omega(aa^\dagger + \frac{1}{2})})(e^{-ikx}e^{-i\Delta\nu t}\sigma + e^{ikx}e^{i\Delta\nu t}\sigma^\dagger)(e^{-i\hbar\omega(aa^\dagger + \frac{1}{2})}). \quad (19)$$

We can also express $k \cdot x$ in terms of the raising and lowering operators using the following equation:

$$k \cdot x = \eta(a + a^\dagger), \quad (20)$$

where $\eta = k\sqrt{\frac{\hbar}{m\omega}}$ is the Lamb-Dicke parameter, which is a measure of the spatial extension of the ground-state oscillator wavefunction.

The propagator $(e^{-i\hbar\omega(aa^\dagger + \frac{1}{2})})$ only acts on the spatial component of the perturbation Hamiltonian, and it can be shown that:

$$(e^{i\hbar\omega(aa^\dagger + \frac{1}{2})})e^{ikx}(e^{-i\hbar\omega(aa^\dagger + \frac{1}{2})}) = e^{i\eta(ae^{-i\omega t} + a^\dagger e^{i\omega t})}. \quad (21)$$

By combining equations 19 and 21, the final form of the interaction Hamiltonian can be written as:

$$H_I = (e^{-i\eta(ae^{-i\omega t} + a^\dagger e^{i\omega t})})e^{-i\Delta\nu t}\sigma + e^{i\eta(ae^{-i\omega t} + a^\dagger e^{i\omega t})}e^{i\Delta\nu t}\sigma^\dagger \quad (22)$$

At the Doppler cooling limit, the spatial component of the ion's final motional state is usually much shorter than the wavelength of the laser. The ion has therefore reached the Lamb-Dicke regime where $\eta \lll 1$. Here, a Taylor series of the right hand side of equation 21 truncated at the first order is appropriate:

$$e^{i\eta(ae^{-i\omega t} + a^\dagger e^{i\omega t})} = 1 + i\eta(ae^{-i\omega t} + a^\dagger e^{i\omega t}) + O(\eta^2). \quad (23)$$

Both terms of the interaction Hamiltonian in equation 22 include transitions that change the electronic state of the ion and transitions that change its motional state. Those transitions that change the motional state correspond

to sidebands which are the result of the modulation of the laser frequency by the motion of the ion. In the Lamb-Dicke regime ($\eta \ll 1$), the excitation on the red sidebands (RSB) and blue sidebands (BSB) is weaker compared to the carrier excitation, and their Rabi frequencies can be approximated by [58]:

$$\Omega_{RSB} = \eta\Omega\sqrt{n}, \quad (24)$$

and

$$\Omega_{BSB} = \eta\Omega\sqrt{n+1}, \quad (25)$$

In case where sidebands can be resolved ($\Gamma \ll \omega$), it is possible to choose a detuning that makes only one sideband is resonant. Therefore, one can simply excite the red secular sideband continuously in order to lower the motional state of the ion. Upon excitation, the ion will occupy a higher electronic state, but a lower motional state, and the emission process on the carrier transition is the most probable in the Lamb-Dicke regime. In principle, every absorption-emission cycle reduces the motional state of the ion by one, and multiple repeated cycles can effectively prepare the ion in its motional ground state [73].

The final temperature after cooling can also be determined using various methods, but this review only focuses on two techniques that were employed in our experiments:

- The mean motional state of the ion can be determined based on excitation probabilities of the red and blue sidebands. In this case, the

ion's ground state population (p_0) can be estimated by the ratio of the sideband peak heights [18]:

$$p_0 = 1 - \frac{p_{RSB}}{p_{BSB}} \quad (26)$$

We rely on this technique only after sideband cooling when the ion is mostly in the motional ground state since it would otherwise result in high uncertainties in the determined temperature.

- To evaluate the temperature after Doppler cooling, one can also make use of the fact that carrier Rabi frequencies slightly vary with the mean motional state of the ion. By exciting on the carrier transition with varying pulse length at constant laser intensity, the excited state population (p_e) oscillates in time, and damped oscillations for longer excitation times are observed due to high motional energy [58]:

$$p_e = \frac{1}{2} \left\{ 1 - \sum_n \rho_{n,n} \cos(\Omega(1 - \eta^2 n)t) \right\}. \quad (27)$$

2.4 *Sympathetic cooling*

For non-fluorescent ions, we can take advantage of their Coulomb interaction with laser-cooled atomic ions to crystallize them [24]. When co-trapped with laser-cooled atomic ions, the non-fluorescent species can be sympathetically cooled to reach the Doppler limit. The cooling efficiency depends on the rate of interaction and the efficiency ϵ of energy exchange per interaction

between the laser-cooled species and the non-fluorescent ions [27]. The energy exchange rate can be expressed as follows:

$$\epsilon = \frac{4r}{(1+r)^2}, \quad (28)$$

where r is the ratio of masses of the refrigerant and the laser-cooled ions. The rate of crystallization of dark ions also depends on their initial temperature, and the time it takes to sympathetically cool an initially hot ion can be approximated as [76]:

$$\tau_{cool} = \frac{m_c}{24m_h} \left(\frac{E_i}{E_C} \right)^3 \frac{2\pi}{\omega_h}, \quad (29)$$

where m_c and m_h are the masses of the cold and hot ion respectively, E_i is the initial temperature of the hot ion, E_C is the Coulomb energy between the two ions, and ω_h is the secular frequency of the hot ion. The above equation shows how the method of ion loading into the trap matters when it comes to crystallization time. For experiments that rely on laser vaporization techniques, the extremely high initial temperature of the ablation plume can make it difficult to load ions into the trap. Thus, certain experiments have precooled the ablated ions with buffer gas before sympathetically cooling them with laser-cooled ions [77].

For sideband cooling experiments, the secular sidebands of a Coulomb crystal are shifted from the normal modes of a single ion; therefore, the appropriate detuning the corresponding normal mode has to be made for efficient sideband cooling. Further details on sympathetic sideband cooling are discussed in Chapter 5 of this thesis.

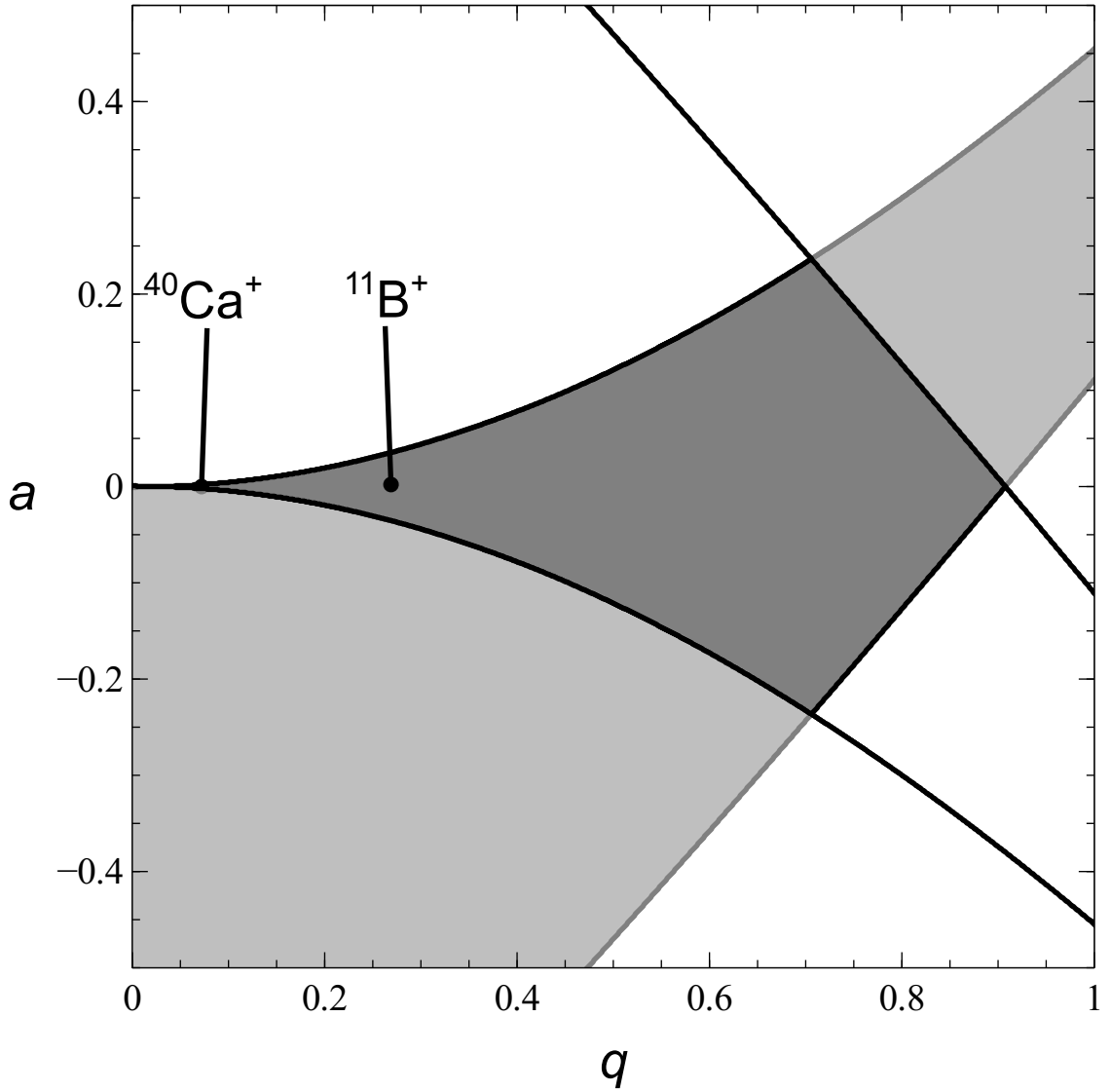


Figure 1: A stability diagram for a linear rf trap is shown. The dark gray region corresponds to stable trapping parameters in the x and y directions. The plot is generated by numerically solving the Mathieu equation using Hill's method documented in Ref. [72]. For our experiments we keep the a parameter at 0 for the trapping and more stability of a wide range of ion masses. The diagram also shows our current parameters for trapping Ca^+ and B^+ ions. Our ability to stably hold Ca^+ ions at such a low Mathieu q value indicates that the residual Mathieu a value is vanishingly small.

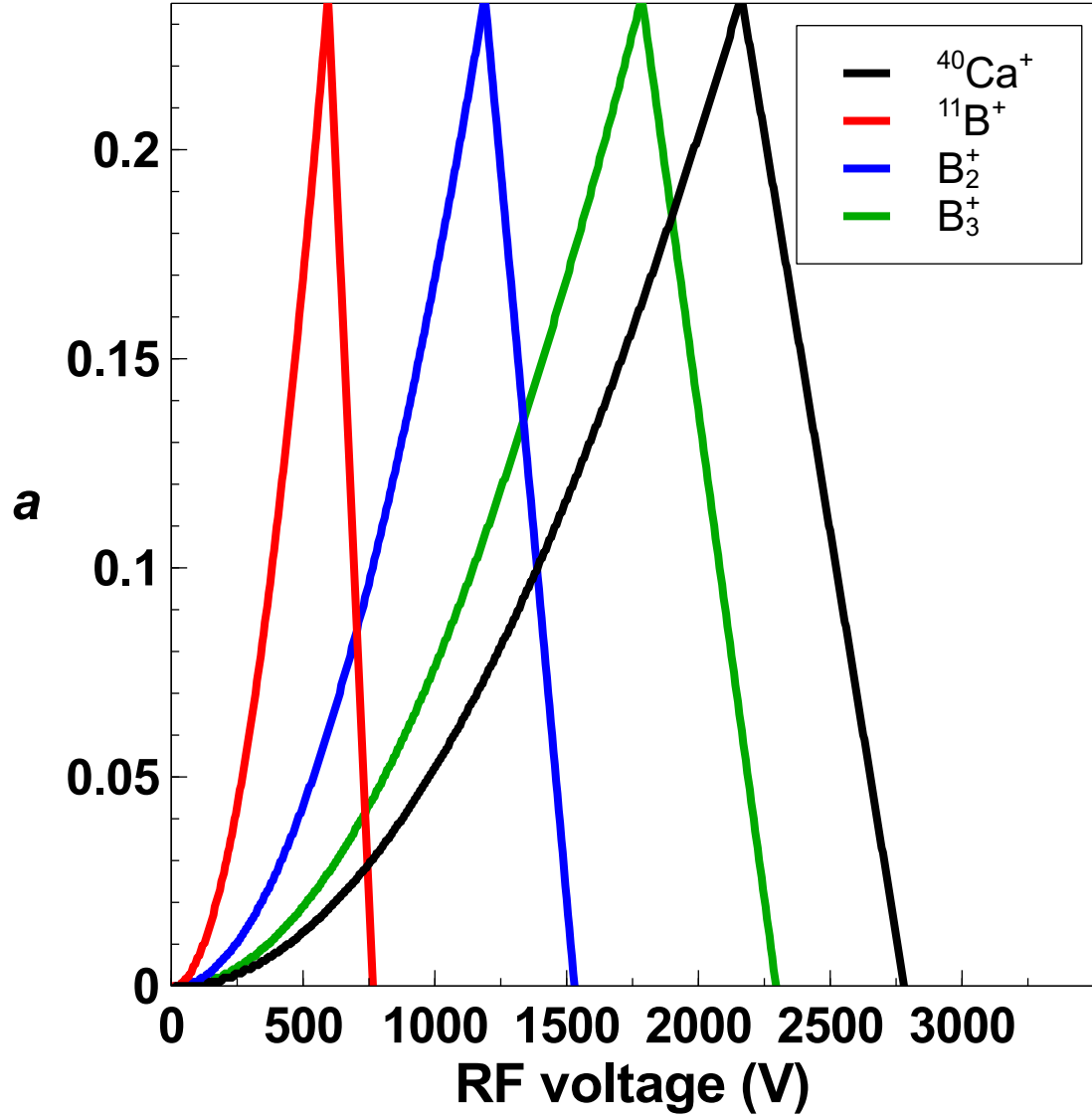


Figure 2: Stability plots for various ion species trapped in our experiments. The trapping region for each ion is under the curve. The plot is generated by numerically solving the Mathieu equation using Hill's method documented in Ref. [72]. The lighter ions have smaller trapping regions than heavier ones.

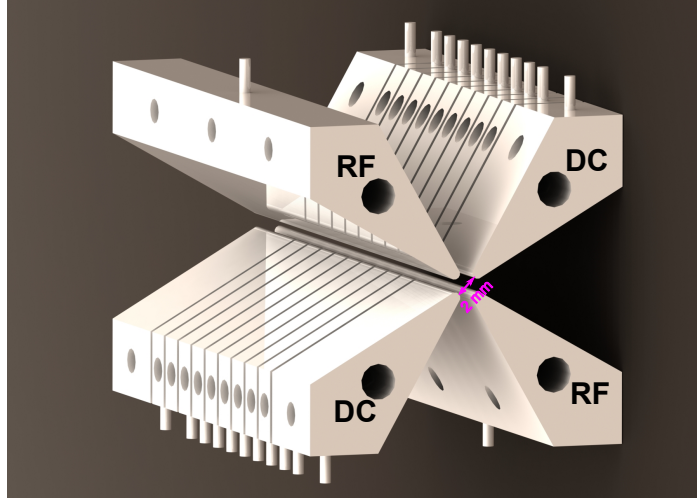


Figure 3: Linear Paul trap with diagonally opposed RF and DC wedge-shaped electrodes and 2 mm diameter. The ions are confined in the $x - y$ plane (transverse plane of the trap) by a RF voltage and along the z -axis (trap axis) by a DC voltage. The DC segments can also be used for further motion and position control of the ions in the trap.

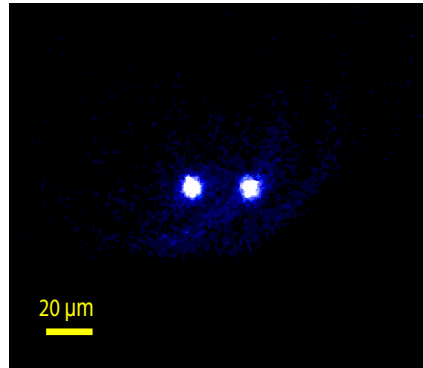


Figure 4: A $^{40}\text{Ca}^+$ ion pair on a CCD camera is shown.

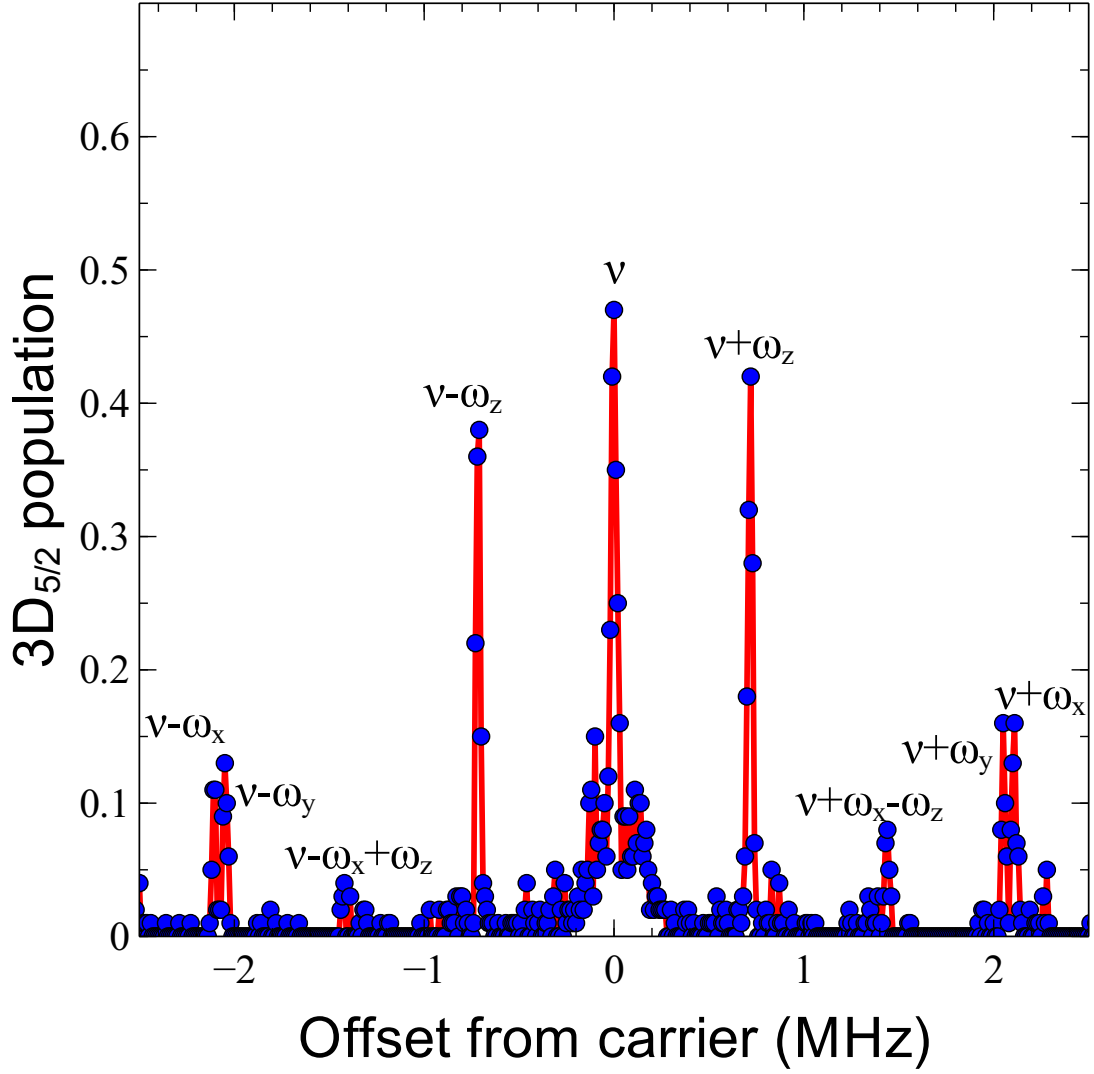


Figure 5: Frequency scan of the $S_{1/2}$ ($m_j = -1/2$) \rightarrow $D_{5/2}$ ($m_j = -5/2$) in $^{40}\text{Ca}^+$ showing the carrier (ν), the axial sidebands (ω_z) and radial sidebands (ω_x and ω_y). The cross-peaks ($\omega_x - \omega_z$) are also observed.

CHAPTER III

EXPERIMENTAL METHODS

Two different experimental setups have produced the data presented in this document. My graduate work has included rebuilding and improving a setup that has been previously described in detail in reference [78]. The other setup was slightly modified to fit the experimental needs and the data collection described in Chapter 5 and it has since been completely rebuilt.

3.1 The Khanyile setup

3.1.1 The Urabe trap

For sympathetic sideband cooling results, we used the Urabe trap, a five-segment linear Paul trap with $r = 0.5$ mm previously used for sympathetic heating spectroscopy experiments [54] and described in detail in [79]. The RF voltage with an amplitude of 122 V oscillated at 14.426 MHz and resulted in a secular frequency of 1.419 MHz in the x-direction and 1.475 MHz in the y-direction for $^{40}\text{Ca}^+$ and a Mathieu q of 0.29. All DC voltages were applied through a low pass filter to reduce the RF pickup on the DC electrodes. We measured an axial frequency of 568 kHz for $^{40}\text{Ca}^+$ with slightly unbalanced DC voltages to align the axial RF and DC electric field nulls.

The Urabe trap has some technical advantages. Its small radius allowed

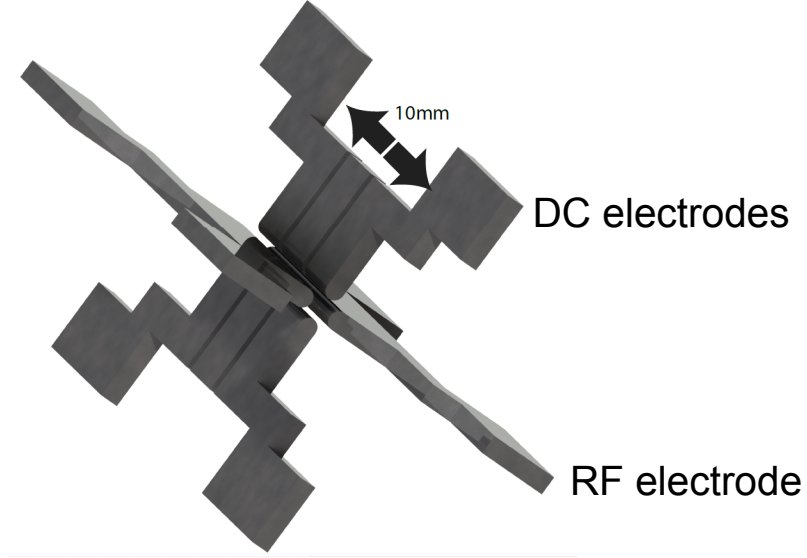


Figure 6: A schematic of the Urabe trap is shown. The DC electrodes include three segments that are used for axial confinement of ions and compensation for excess micromotion [79].

strong confinement of ions with low voltages, and low Mathieu q necessary for high cooling efficiency are attainable. This trap, however, is slightly asymmetric which made compensation of excess micromotion a bit challenging.

3.1.2 Vacuum system

The Urabe trap is housed in a 4.5" spherical octagon vacuum chamber with six windows used for optical access and electrical connections. The pressure inside the chamber was kept at less than 1×10^{-11} Torr using a Duniway 50L/s ion pump (DSD-050-5125-M) and a Ti sublimation pump (Gamma Vacuum 360819). An additional mechanical pump was used for differential

pumping to further reduce collisions of the trapped ions with background gas.

3.2 The improved Goeders setup

The rest of the experiments were carried out using the Goeder's trap also described in further details in [78]. The setup surrounding this trap was improved upon from its initial version discussed in [80]. No changes, however, were made to the trap itself. The improvements made to the setup had several goals to achieve:

- Greater number of accessible viewports for lasers,
- Shielding DC connections from RF pickups for more efficient compensation of micromotion
- Improved computerized control of experiments
- Ion loading using ablation of calcium and boron targets

3.2.1 The Goeder's trap

The Goeder's trap is an eleven-segment ion trap with a relatively large radius ($r = 1$ mm), which makes it more suited for trapping large Coulomb crystals. Each segment is 3 mm in width and spaced by 0.5 mm from the next. The whole trap extends 86 mm in length. This trap is also equipped with two compensation rods mounted along the axis of the trap. The electrode blades

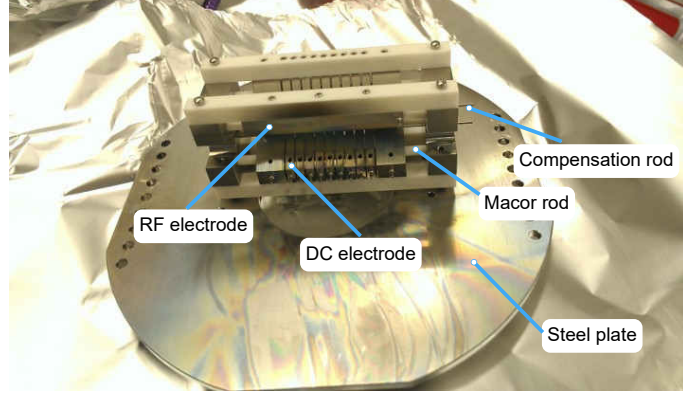


Figure 7: The Goeders ion trap mounted on a steel plate that connects it to the chamber is shown. The RF and DC electrodes are wedge-shaped and have a curvature radius of 0.5 mm. The trap structure is held together by four Macor rods. The small screws visible on each electrode hold them firm onto the Macor rods. The compensation rods are diagonally opposed and span the whole length of the trap. The top one is used for compensation for excess micromotion while the bottom one is grounded. A reversed configuration would also work. The voltages are applied on these rods are in the range of 50 V in magnitude and are relatively high because of the shielding caused by the RF electrodes.

are mounted to two stainless steel frames by four Macor rods as shown in Figure 7.

3.2.1.1 RF electronics

The trapping RF signal is generated by a function generator (BK Precision 4087) and amplified by a RF amplifier (Bruker BLAX300RS), which couples the voltage signal into a helical resonator. The helical resonator filters out

harmonics and matches the impedance. For the experiments described in this thesis, RF voltage oscillates at 19.35 MHz, a frequency high enough for low Mathieu q values (lower than 0.1) necessary for trapping boron and boron hydride ions.

The amplified voltage from the resonator is applied to the RF electrodes of the trap through two-pin copper feedthroughs (Kurt J Lesker EFT0123053). A pair of 20 gauge Kapton insulated high-voltage wires (Accu-Glass 112716) connects the feedthroughs to the RF electrodes of the trap.

3.2.1.2 DC electronics

A new DC voltage system was built to allow computer-controlled voltage adjustment, and future automated compensation for micromotion. The DC potentials for all eleven electrodes are controlled by a Labview program and converted to analog signals via a digital to analog converter (DAC) board (Analog Devices EVAL-AD5370). The converted signal is amplified by a 25-channel amplifier to meet the voltage needs up to 70V per channel. The DC voltage goes through a low-pass filter board connected directly to the chamber. A DB-25 connector (Accu-Glass 100460) bridges the filter board and the vacuum system through Kapton-insulated wires (25 AWG, Accu-Glass 100761), which send voltage waveforms to all 22 DC electrodes of the trap.

The RF voltage used for motional resonance experiments is capacitively coupled to the middle top DC electrode of the trap. An injection board for

1	2	3	4	5	6	7	8	9	10	11
10.000	10.000	10.000	5.000	5.000	-0.159	12.400	5.000	10.000	10.000	10.000

10.000	10.000	10.000	5.000	5.000	0.000	12.400	5.000	10.000	10.000	10.000
1	2	3	4	5	6	7	8	9	10	11


Voltage (V) 

Figure 8: Schematic representation of the waveform applied on each electrode of the Goeders trap. Voltages on electrodes 5 and 7 confine the ions axially in the trap center and are of different magnitudes due to the asymmetry of the trap. Outer electrodes are used to avoid additional trapping regions. We use low confinement voltages particularly for experiments involving large Coulomb crystals. The middle electrodes are used for compensation for excess micromotion.

this signal bypasses the filter board and sends the signal generated by a direct digital synthesizer (DDS) (Analog Devices AD9959) and amplified by a low noise RF amplifier (Mini Circuits TIA-1000-1R8).

3.2.2 Vacuum system

The vacuum system for this setup consists of a larger (8") vacuum chamber (Kimball Physics MCF800-SphOct-G2C8) with eight windows used for optical input and electrical connections. Five of the six side viewports (Kurt

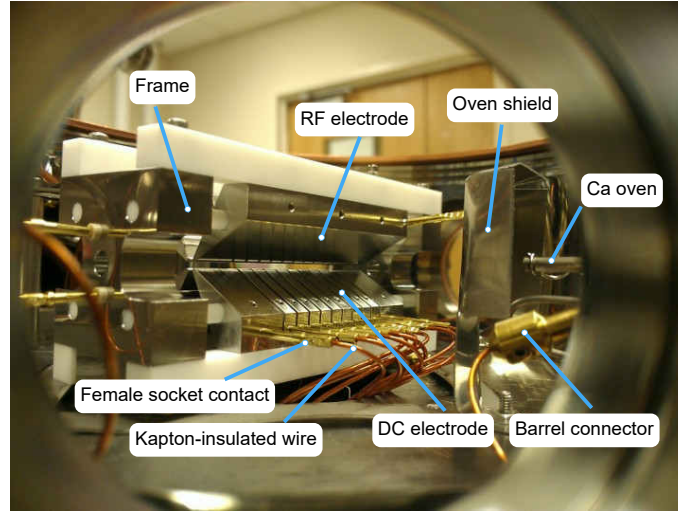


Figure 9: A view of inside the chamber through one of the viewports shows various electrical connections. Female socket contacts were crimped onto Kapton-insulated wires and connected to each trap electrode. The calcium oven is also shown with barrel connectors used to hold the oven and connect it to electrical feedthroughs. The oven consists of a thin stainless steel tube 0.1 in in diameter with 0.002 in thick walls that is crimped on one end and filled with elemental calcium metal through the other end. One wire is wrapped on the open end and the other wire crimped on the closed end. This type of oven provided good collimation of the neutral calcium flux and required lower current.

Lesker VPZL-275) as well the top glass (Kurt Lesker VPZL-800) are Kodial glass reserved mainly for UV/Visible photon transmission. The other side viewport made of CaF_2 was reserved for future IR laser input. The main chamber sits on a 4.5" five-way cross (Kurt J. Lesker C5-0450). One end of the cross connects to a 55L/s diode ion pump (Varian 9191320), and an other end holds the feedthroughs used for DC connections. The rest of the cross is connected to two 2.75" nipples holding a titanium sublimation pump (Gamma Vacuum 360819) and an ion gauge (Duniway I-NUDE-F).

An additional mechanical pump is used for differential pumping when hydrogen gas is added to the chamber. While the ion pump is always running, the titanium sublimation pump is only occasionally turned on to decrease the pressure of background gas molecules especially when collision-induced heating on trapped ions surges. Furthermore, the use of the titanium sublimation pump is kept at a minimum to maximize its lifetime. Pressures of 1×10^{-10} Torr are typical in this system.

3.2.3 Fluorescence detection and ion imaging

For this setup the photon detection system consists of a home-made lens stack for photon collection, a CCD camera for imaging (Princeton Instruments Cascade 1K), and photomultiplier tube for photon counting (Hamamatsu H7360-02 PMT). The 397 nm photons from Ca^+ ions go through a narrow band filter to reduce background. The lens stack with a numerical aperture of 0.25 is mounted 5 mm from the top viewport of the chamber and collects

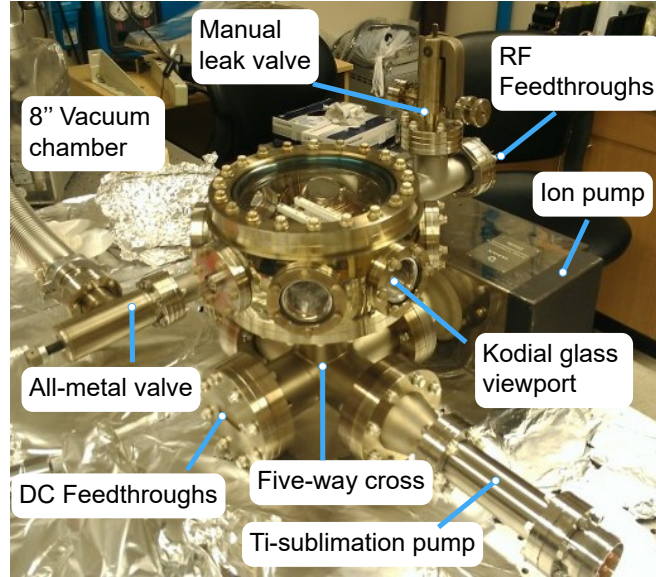


Figure 10: The chamber assembly is shown. The main chamber sits on a five way cross that also holds the ion pump, the DC feedthroughs, the titanium sublimation pump, the all-metal valve, and the ion gauge. Kodial glass side viewports used for laser input and additional feedthroughs are connected to the main chamber. The manual leak valve used for as a gas inlet is also shown. The titanium sublimation pump is used occasionally to reduce excess background gas, and the ion pump is kept on all the time to maintain UHV pressures of around 1×10^{-10} Torr. It is connected to a dual ion pump controller which also registers the pressure inside the chamber.

the fluorescence of the trapped ions. The ions' fluorescence is then focused onto an iris used to reduce background scatter. Due to limited vertical space, we use a mirror before the iris to reflect the fluorescence horizontally. An additional lens located at 37 mm from the iris is used for further magnification and forms the image of the ions onto the camera. A large fraction of the fluorescence (70 %) goes to the PMT after the beam splitter.

The photon detection system is one of the components of the setup that was modified from the previous setup described in [78]. The major changes include the horizontal configuration, additional relay lens, and swappable filter mount. The previous system had to be taken apart to replace filters, and there was no easy control on the amount of light transmitted. The 2-D adjustable iris was added to allow the viewing of either large crystals or a single ion with very low background.

3.3 Computer control

All the experiments described in this thesis required some level of automation using a computer for fast data collection and analysis. One computer was used to control a direct digital synthesizer (DDS) used to generate an oscillating voltage. The AC signal from the DDS controls acoustic-optical modulators (AOM) that switch various laser beams. The DDS is switched by a field-programmable gate array (FPGA) board. This board is also responsible for the timing of experiments and counting fluorescence.

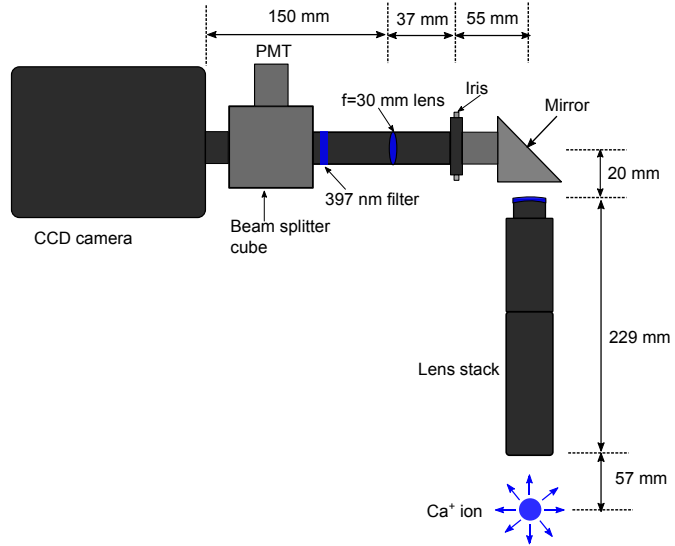


Figure 11: A schematic shows the fluorescence detection setup. The ions located in trap center emit photons that are collected by the lens stack mounted 5 mm above the top window of the chamber. The lens stack firstly forms the image onto the iris and a $f = 30$ mm lens sends the fluorescence to the PMT and CCD camera through a 397 nm filter.

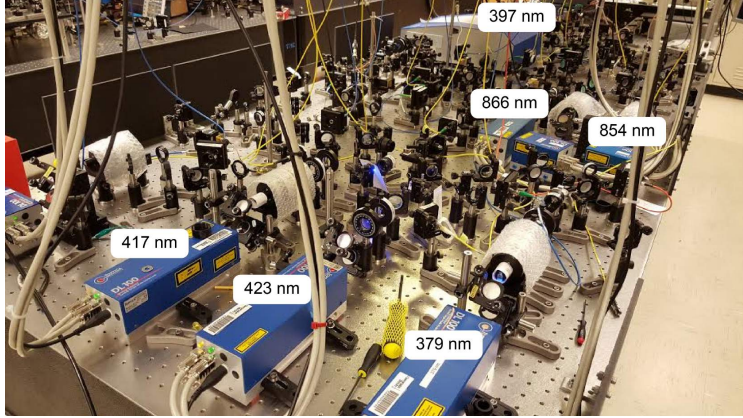


Figure 12: The laser system used for ionization of Ca and the laser cooling of Ca^+ ions is shown. Each laser beam is transported to the experiments using an optical fiber.

3.4 Lasers

Our laser system consists of lasers used to ionize neutral Ca and to cool $^{40}\text{Ca}^+$ ions, a HeNe laser used as a frequency reference, a Ti-Sapphire laser (Coherent Mira 900) used for the spectroscopy of CaH^+ ions, and a frequency-tripled YAG laser (Continuum minilite II) used for ablation loading.

All the lasers used for the ionization and the cooling of Ca^+ ions are external-cavity diode lasers (ECDLs) preferred for their narrow linewidths and lower cost. Doppler cooling lasers and the 854 nm laser used for sideband cooling are frequency-stabilized to a scanning cavity stabilized by the He-Ne laser. For more details on this cavity system, the reader is referred to reference [79]. The laser system is shown in figure 12.

For the 729 nm laser, a high finesse cavity is used to narrow the laser linewidth necessary for resolved sideband measurements. The laser is locked to the cavity using a Pound Drever Hall (PDH) scheme. The finesse of this cavity is around 100,000, and the linewidth of the laser is lowered to less than 1 kHz. A Toptica Fast Analog Circuit (FALC) sends feedback to the laser for frequency adjustments. We have also acquired an EagleYard tapered amplifier (TA)(Eagle Yard EYP-TPA-0735-00500-3006-CMT03-0000) to generate more 729 nm power. The TA has its own temperature (Thorlabs TED 200 C) and current (Thorlabs LDC 240 C) controllers, and it is kept at 19.5 °C for optimal power output.

The temperature control system of this diode was built based on a design from the Kuzmich Lab. The diode is held by a Thorlabs cage plate which is mounted to an aluminum base. A thermoelectric cooler (TEC) connected to the temperature controller stabilizes the temperature of the diode, and is also connected to an aluminum heatsink. A fan is mounted on the top of the heat sink to avoid overheating. The temperature is measured using a thermistor which is also connected to the temperature controller. The operational current is 1.5 A, but lower currents are preferable to maximize the lifetime of the diode. High powers are necessary to induce stimulated emission in the device and thus provide amplification, so our TA is seeded with 20 mW of power, and it is able to output 500 mW. However, the TA high output power can generate optical feedback into the master laser and destabilize the lock. To avoid this problem, we used a Conoptics Model 716

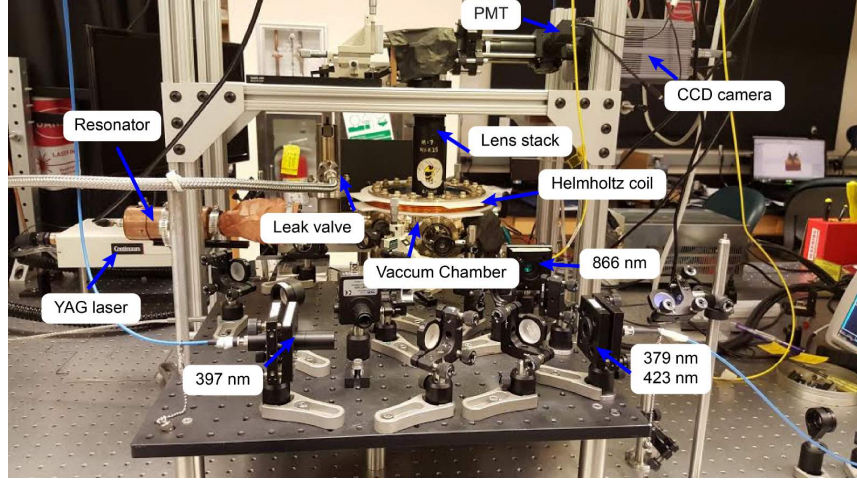


Figure 13: The setup used for the spectroscopy of CaH^+ ions and the trapping and detection of B^+ ions is shown. The optics around the chamber combine and steer the beams onto the axial and radial axes of the trap. The helical resonator is used as an amplifier and filter for the RF voltage used to trap ions. The Helmholtz coil on top of the chamber generates a magnetic field of a few Gauss used to split the Zeeman levels in Ca^+ . We use the manual leak valve (Kurt J. Lesker VZLVM267) to add hydrogen to the chamber.

double isolator with 60 dB of isolation. An additional isolator is used to protect the TA from back reflections.

For laser ablation experiments, we used a 355 nm nanosecond YAG laser (Continuum Minilite II) is focused onto the target through one of the axial viewports. Our Ti-Sapphire laser is frequency-doubled using a 0.1 mm thick Foctek BBO crystal for the spectroscopy of CaH^+ ions.

3.5 Trapping of Ca^+ ions and compensation of excess micromotion

3.5.1 Vaporization of neutral Ca and beam alignment

The trapping of single atomic ions requires the sublimation of Ca metal using a stainless steel oven described in the previous section. Neutral Ca vapor can be detected by looking at the fluorescence of Ca atoms excited by a 423 nm laser. Initially, the laser beams used for ionization and ion cooling are coaligned both along the trap axis and at 45° from the trap axis. To align the beams to the trap center, they are moved both vertically and horizontally to the edges of the trap or chamber viewports and fixed at the intersection of the two directions. This method is effective of 3D traps and requires the beams to be aligned on a distant wall.

After the initial alignment process, the search of neutral Ca fluorescence follows. The crossing point of the axial and radial beams detected on the camera should be very close to the trap center. At this point, the search for ions can begin.

3.5.2 Compensation for excess micromotion

The cooling efficiency of trapped ions can be substantially reduced the ion's excessive motion when it's synchronized with the RF oscillation of the trap. Various stray fields in the trap, trap asymmetries, and any phase between between RF signals applied on trap electrodes can push the ion from the pseudopotential minimum. Stray electric fields are usually the result of the

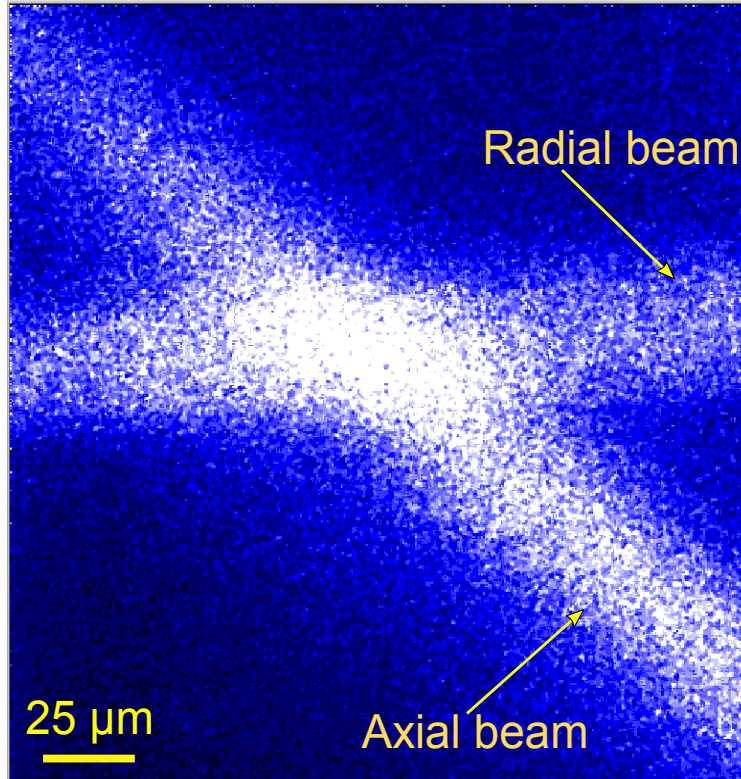


Figure 14: The neutral Ca fluorescence induced by the 423 nm laser is shown. The Ca oven is run hotter than normal to observe enough fluorescence. Initially, the two beams are aligned to the trap center by moving them vertically and horizontally and finding middle points. The camera is aligned to where the two beam cross, and the trapping of ions can follow.

photoelectric field on the trap electrodes especially when they have been coated with calcium, which has a relatively low work function. This effect can be observed when UV photons used for ionization or ion cooling hit the trap. In addition, imperfections in trap symmetries can tilt the potential thus shifting the minimum from the expected point. Phase shifts between RF voltages on trap electrodes are also a source stray fields that cause excess micromotion. These shifts can result from a difference in thickness or lengths of the two trap wires or in electrode size.

In our experiments, these phase differences are minimized by choosing the same length for RF wires and by shielding both the wires and the electrodes from coating by calcium metal. To detect and eliminate excess micromotion, we employ two methods that are usually iterated.

3.5.2.1 The averaged-ion position technique

This method uses the image of the ion to monitor its position as the RF amplitude is changed. The direction in which the ions need to be moved to reach the RF null corresponds to the direction they move upon increase of the RF amplitude. A DC voltage applied to a center electrode of the trap is used to move ions in the appropriate direction for micromotion compensation. The compensation voltage is tuned until the ions remain still on the camera when the RF potential amplitude is changed. This technique is rather coarse and needs to be combined with the photon correlation technique.

3.5.2.2 *The photon correlation technique*

Excessive micromotion happens when the ion's motion synchronizes with the trap RF field which engenders large Doppler shifts that can be detected on the PMT signal. When the ion is not located in the trap center in one of the radial directions, it unevenly experiences an oscillating force induced by the oscillating field which pushes it back and forth in the direction of the cooling beam. This motion induces Doppler shifts, and if the PMT counting is synchronized with the RF drive, the correlation between the fluorescence level and the RF field direction can be detected. By applying a DC voltage on the top compensation rod, the ion can be pushed towards the center to minimize the unevenness in fluorescence. The micromotion can also be detected by looking at the phase between the RF signal and the arrival of the photons on the PMT. A constant phase is a sign of high micromotion while a highly-varying phase is indicative of a well-compensated trap. The fluorescence modulation method is also applicable to the elimination of excess micromotion in the axial direction of the trap [81]. Figure 15 shows the photon correlation data from the PMT when different voltages are applied to the top compensation rod of the trap.

Elimination of excess micromotion using the methods outlined above is required for daily operation and is achievable for long chains of ions, an advantage afforded by linear Paul traps. For the Goeters trap, little daily variation in compensation voltages has been observed, and this property makes

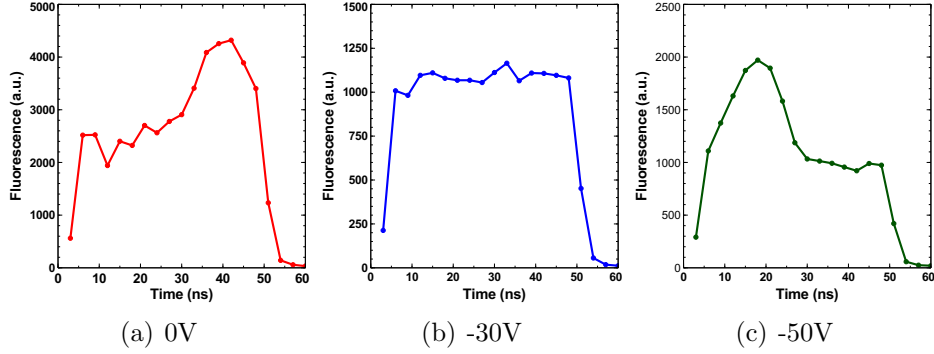


Figure 15: The fluorescence signal is recorded as a function of photon arrival time. The PMT data is sampled by a 300 MHz clock synchronized by the RF signal. (a) One can observe unevenness in fluorescence which indicates that there is correlation between the photon arrival time and the RF oscillation. (b) The trap is compensated and there is no correlation between photon arrival time and RF oscillation. (c) As the voltage is decreased past the compensation point, a phase change occurs, and there is correlation between photon arrival time and RF oscillation again. The slow drop-off at the longest times is caused by the fact that the clock speed is at the limit of the FPGA clock.

it a reliable system for both high precision experiments requiring sideband cooling, as well as experiments involving large Coulomb crystals.

CHAPTER IV

THREE-MODE SIDEBAND COOLING OF A SINGLE $^{40}\text{Ca}^+$ ION

As previously mentioned, direct laser cooling methods are difficult to implement on molecular ions due to their lack of closed transitions. As a result, most molecular species require sympathetic cooling to reach temperatures where precise spectroscopy methods can be done. For CaH^+ , the most efficient refrigerant ion is $^{40}\text{Ca}^+$ because the Coulombic interaction is strong due to mass similarities. We therefore implemented the ground state cooling of all three modes of motion of a single $^{40}\text{Ca}^+$ ion as a step towards the sympathetic sideband cooling of CaH^+ .

The system used for this experiment is outlined in reference [78] and is similar in many ways to the setup described in the previous Chapter. Both Doppler cooling lasers (397 nm and 866 nm) were co-aligned with the photo-ionization lasers as well as the 854 nm laser used to deshelve the ion during sideband cooling. The 729 nm laser beam used for sideband cooling was sent into the trap at a 45° angle from the trap axis. A magnetic field of a few Gauss perpendicular to the axis and the 729 nm polarization was used to split the Zeeman levels.

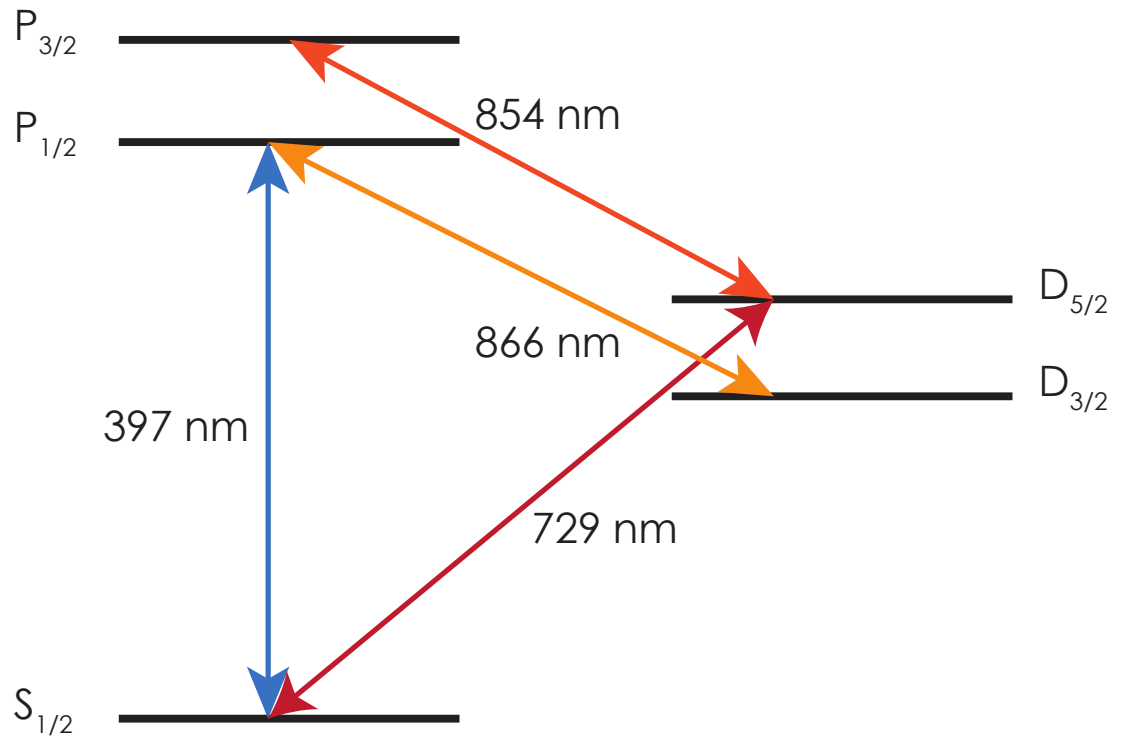


Figure 16: A diagram shows the transitions used to Doppler cool and sideband cool Ca^+ . Doppler cooling is achieved by using the 397 nm laser and the 866 nm laser to repump the $D_{3/2}$ metastable state. Sideband cooling takes place on the quadrupole 729 nm transition and uses an 854 nm repumper to bring the ion back into the ground state.

4.1 *State detection*

The electronic state of the ion was detected based on the fluorescence of the ion. Once excited to the metastable $D_{5/2}$ state, the ion becomes dark and can be distinguished from its ground state by using the histogram shown in figure 17. Low fluorescence counts indicate that the ion is not being excited from the ground electronic state by the 397 nm cooling laser. The population of the $D_{5/2}$ state was measured as the number of dark events (below the bright ion fluorescence threshold) registered out of 200 measurements. The ambiguity between bright and dark events was further reduced by multiplying the fluorescence counts of consecutive measurements.

4.2 *Optimization of Doppler cooling*

To efficiently cool all the the ion's normal modes, we optimized Doppler cooling by varying the 397 nm cooling power and frequency. Optimal Doppler cooling was at relatively low powers and at frequencies 11 MHz detuned from resonance. A 729 nm scan on the carrier transition shows Rabi flops or population oscillations between the two electronic states as the interaction time is varied. To evaluate our Doppler cooling efficiency, the Rabi scan was fitted to the following equation [58] which approximated the thermal state $\rho_D(t)$ of the ion:

$$\rho_D(t) = \frac{1}{2} \left(1 - \frac{1}{\bar{n} + 1} \frac{\cos(2\Omega_0 t)(1 - x \cos(2\Omega_0 t \eta^2)) + x \sin(2\Omega_0 t) \sin(2\Omega_0 t \eta^2)}{1 + x^2 - 2x \cos(2\Omega_0 t \eta^2)} \right), \quad (30)$$

where Ω_0 is the Rabi frequency, x is the ion's displacement and \bar{n} is the final number of quanta after Doppler cooling.

4.3 Spin polarization

We used the $4S_{1/2} \rightarrow 3D_{5/2}$ to sideband cool the ion. With the Zeeman levels lifted, the ion needed to be prepared in one of the spin states of the electronic ground state before initiation of the cooling process. Excitation on the $S_{1/2} (m_j = +1/2) \rightarrow D_{5/2} (m_j = -3/2)$ transition prepared the ion in the $S_{1/2} (m_j = -1/2)$ Zeeman state. During this process, the 729 nm laser shelved the ion for a few μs into the $D_{5/2} (m_j = -3/2)$ metastable state, and then the 854 nm was used to deshelve the ion. The cycle was repeated a few times to reach a $> 99\%$ population in the $S_{1/2} (m_j = -1/2)$ Zeeman state.

4.4 Sideband cooling

The sideband cooling scheme proceeded by first Doppler cooling the ion for 500 μs with the 397 nm laser detuned 10 MHz from resonance and then continuously exciting with the 729 nm laser on the axial or radial sidebands for 2.4 ms with the 854 nm laser on. Each cooling cycle was preceded by a spin polarization phase, which was alternated with the cooling and repeated every 40 μs . After cooling, the two-ion crystal was probed with the same technique used to measure motional sidebands. The average motional quanta after cooling is determined through the ratio of the heights of the red and blue sidebands [18].

We achieved a mean motional state of $\bar{n}_z = 0.046 \pm 0.02$ ($T_z=11.2 \pm 0.003 \mu\text{K}$) in the axial direction, and $\bar{n}_x=0.33 \pm 0.092$ ($T_x=79.4 \pm 2.3 \mu\text{K}$) as well $\bar{n}_y=0.32 \pm 0.025$ ($T_y=77.0 \pm 5.8 \mu\text{K}$) for the radial directions. The less efficient cooling observed in the radial direction could be due to excess micromotion. This experiment was carried out using the Goeder's trap before the setup was rebuilt. At the time of this data collection, compensation for excess micromotion became unusually difficult due to a phase between the two RF electrodes [81]. The potential cause of this phase was the coating of one of the RF wires by the Ca oven, and this problem was one of the reasons the setup had to be rebuilt and modified.

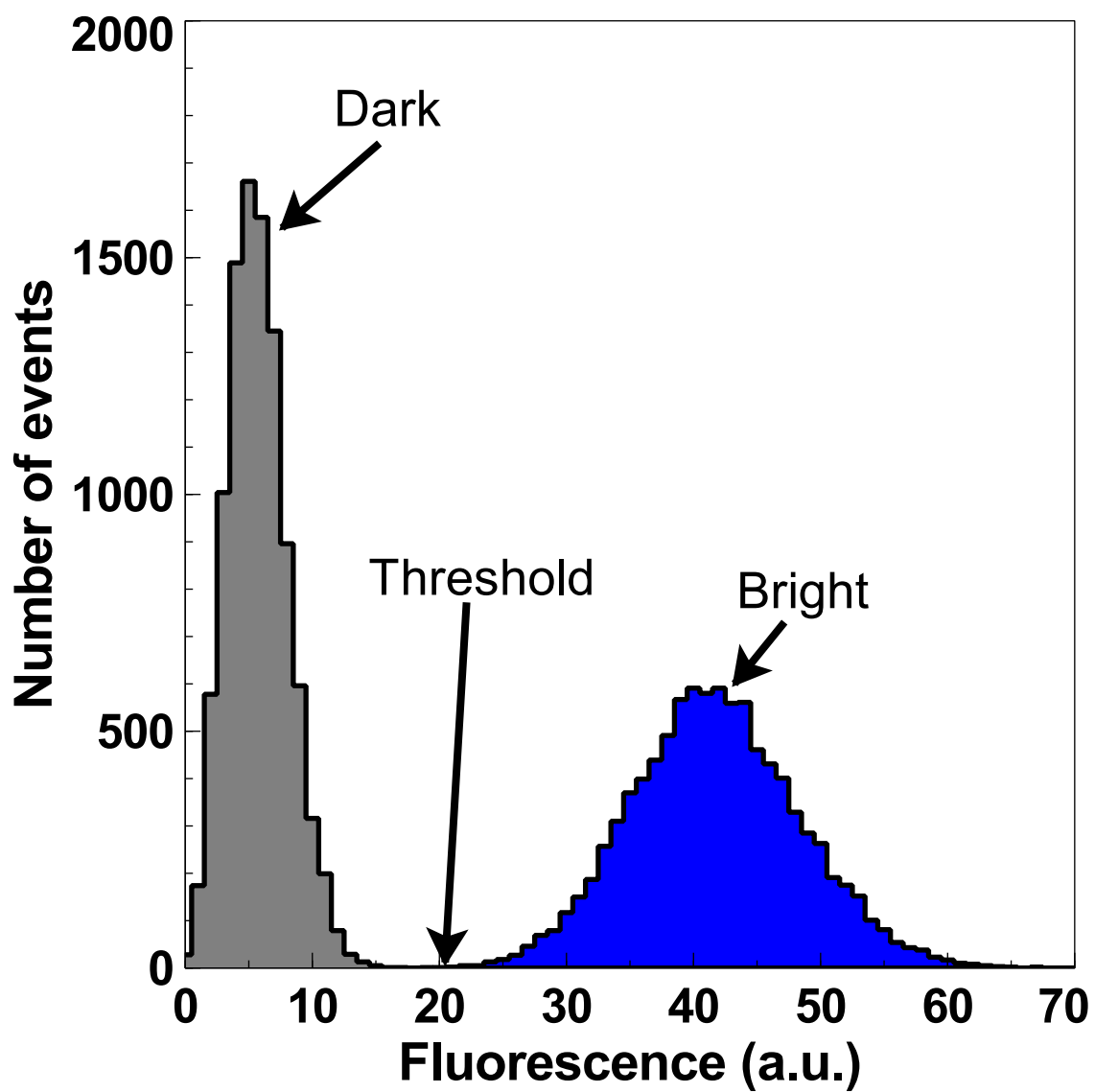


Figure 17: A histogram shows the fluorescence distribution of a bright ion and a dark ion. Below a given threshold the ion is considered excited to the $D_{5/2}$ state (shelved).

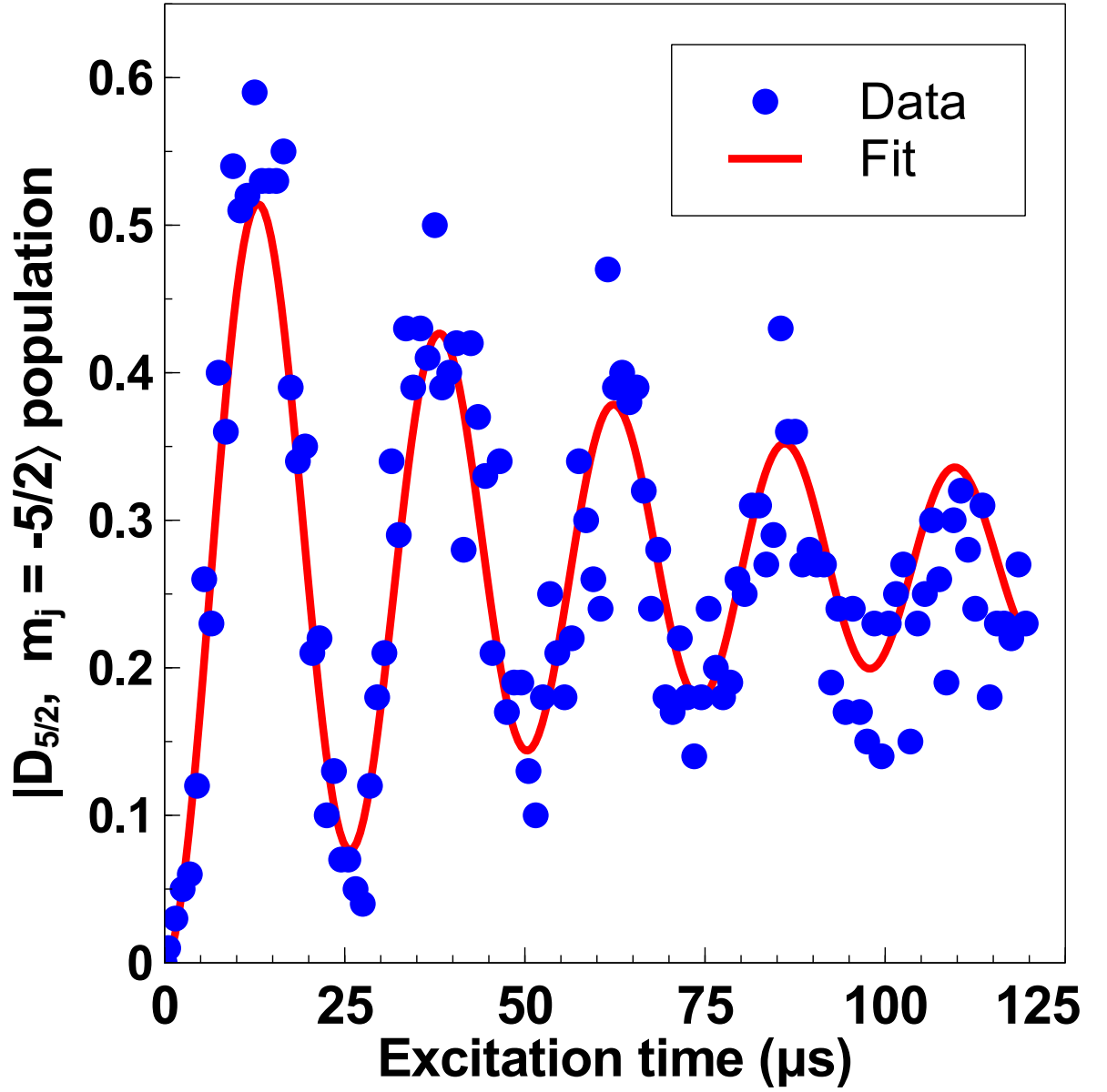


Figure 18: A Rabi scan on the $4S_{1/2} \rightarrow 3D_{5/2}$ transition carrier fitted to equation 30 is shown. In this scan, Doppler cooling reaches 13 quanta which is low enough to initiate sideband cooling.

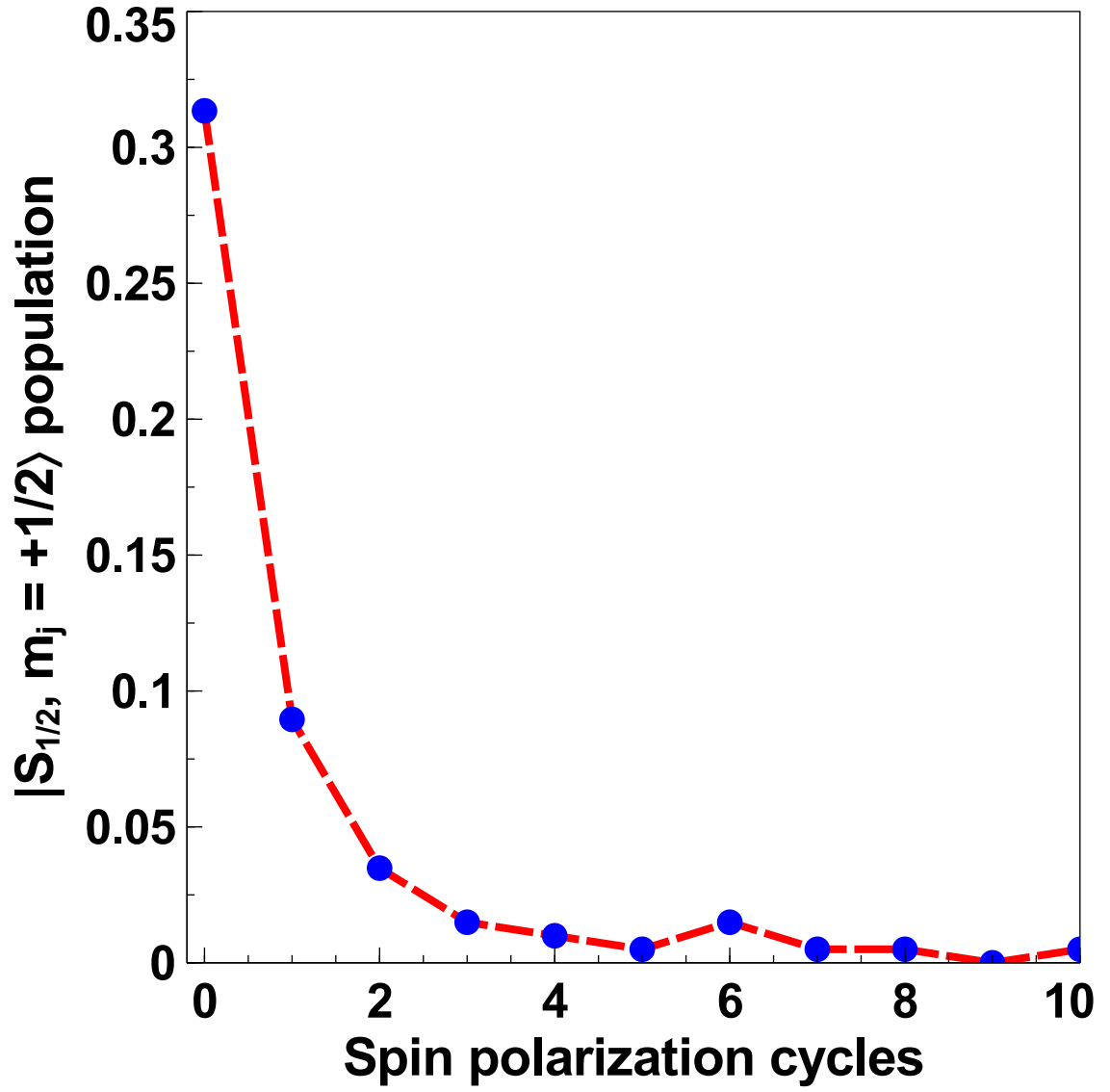


Figure 19: Optical pumping into the $S_{1/2}$ ($m_j = +1/2$) spin state is shown. In this figure, 5 excitation cycles on the $S_{1/2}$ ($m_j = +1/2$) \rightarrow $D_{5/2}$ ($m_j = -3/2$) transition are enough to fully prepare the ion in the desired spin state.

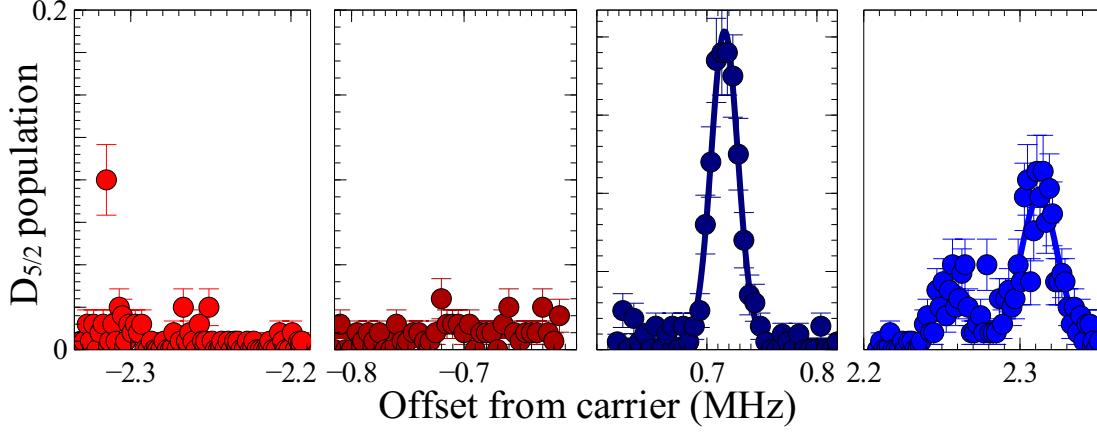


Figure 20: Measurement of the $S_{1/2}$ ($m_j = -1/2$) \rightarrow $D_{5/2}$ ($m_j = -5/2$) first-order sidebands for the $^{40}\text{Ca}^+$ ion by electron shelving. Red and blue sidebands are fit to a Gaussian of the same width but variable amplitude. Comparison of sideband heights yields an average mode occupation of $\bar{n}_z = 0.046 \pm 0.02$ ($T_z = 11.2 \pm 0.003 \mu\text{K}$) for the axial mode and $\bar{n}_x = 0.33 \pm 0.092$ ($T_x = 79.4 \pm 2.3 \mu\text{K}$) as well as $\bar{n}_y = 0.32 \pm 0.025$ ($T_y = 77.0 \pm 5.8 \mu\text{K}$) for the radial modes.

CHAPTER V

SYMPATHETIC SIDEBAND COOLING OF CaH^+

This chapter is based on the following article:

R. Rugango, J. E. Goeders, T. H. Dixon, J. M. Gray, N. Khanyile, G. Shu, R. J. Clark, and K. R. Brown, New. J. Phys. **17**, 03009 (2015).

With the ground state cooling of a single Ca^+ implemented, sympathetic sideband cooling of molecular ion motion to the ground state is one step closer. The Urabe trap had to be used for this experiment because of the faster reaction between Ca^+ and H_2 that were observed with this setup.

5.1 Trapping of the Coulomb crystal and normal mode measurement

Initially, we trap two $^{40}\text{Ca}^+$ ions and H_2 gas is leaked into the vacuum chamber using a manual leak valve (Kurt J. Lesker VZLVM967) (figure 29a). The reaction between $^{40}\text{Ca}^+$ and H_2 is photo-activated by exciting the $^{40}\text{Ca}^+$ ion from its $4\text{S}_{1/2}$ ground state to the $4\text{P}_{1/2}$ state [34]. A reaction with one of the atomic ions occurs typically five min after the addition of H_2 gas at pressures around 5×10^{-7} Pa. After the reaction, the newly formed dark CaH^+ molecule is sympathetically cooled through its Coulombic interaction with the remaining $^{40}\text{Ca}^+$ ion.

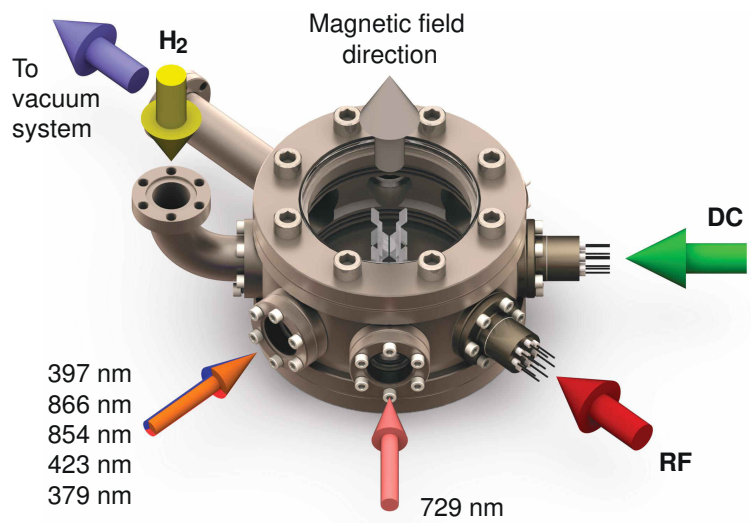


Figure 21: The experimental setup including the vacuum chamber and the trap is shown. The magnetic field of 1.4 Gauss is perpendicular to the trap axis and the direction of the lasers. DC connections include compensation voltages, endcap voltages, and oven current.

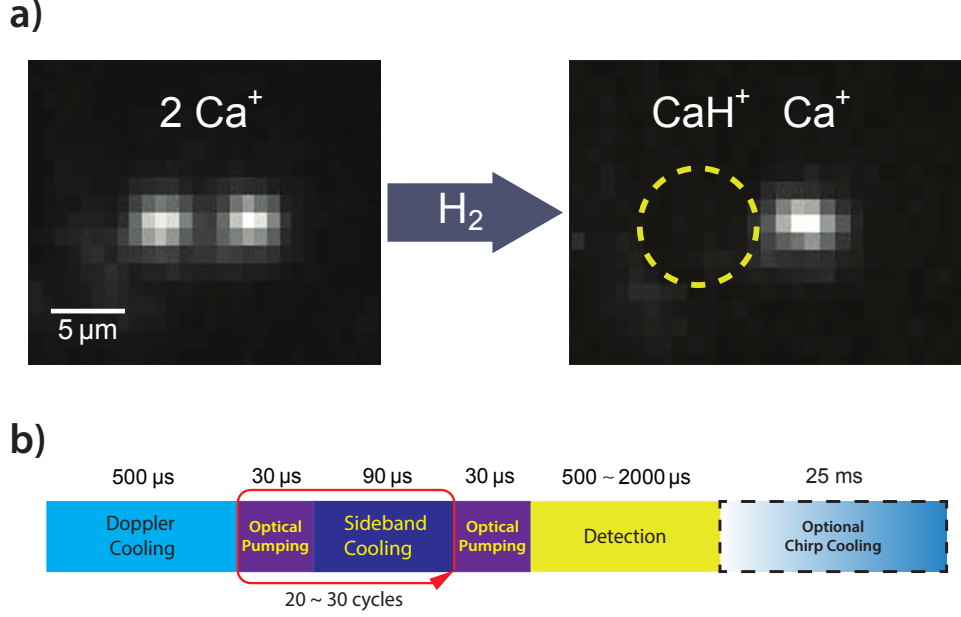


Figure 22: (a) One $^{40}\text{Ca}^+$ reacts with H_2 to make $^{40}\text{CaH}^+$ which is not fluorescent. (b) The experiment sequence begins by Doppler cooling the two-ion crystal followed by optical pumping and sideband cooling cycles. After sideband cooling, we perform electron shelving measurements on the motional sidebands and detect the atomic state.

The motional modes of the Coulomb crystal are precisely measured by exciting the $4\text{S}_{1/2} \rightarrow 3\text{D}_{5/2}$ quadrupole transition with the 729 nm laser and counting the number of electron shelving events [82]. With the 729 nm laser aligned in the axial direction, only the axial motional modes of the crystal can be detected. These modes correspond to a harmonic movement of the two ions in phase, also called the center of mass mode (COM), and out of phase, the breathing mode (BM).

The secular frequencies of the two-ion crystal are related to the axial

motional frequency of a $^{40}\text{Ca}^+$ ion by

$$\nu_{\pm}^2 = [(1 + \mu) \pm \sqrt{1 - \mu + \mu^2}] \nu_1^2, \quad (31)$$

where the ν_- and ν_+ correspond to the COM and BM respectively, ν_1 is the secular frequency for a single ion, and μ is the ratio of the mass of the reference atomic ion to the mass of the second ion. This relationship can be used to determine the mass of the molecular ion [30, 78] and deviations from this relationship can be used to measure stray electric fields [49, 78]. The measured COM frequency is 563 ± 4 kHz while the BM frequency is 976 ± 1 kHz. This is in good agreement with the expected values of 564 kHz and 978 kHz and inconsistent with other possible molecular species.

5.2 *Sideband cooling*

The sideband cooling scheme is similar to the one used on a single ion. The 729 nm excitation alternates between the red first order COM and BM sidebands for 6 ms with the 854 nm laser on. During the cooling process, the ion crystal occasionally suffers from collisions with residual background gas. Collisions during the sideband cooling procedure will melt the crystal and result in temperatures far above the Doppler cooling limit. Cooling lasers close to resonance may not completely bring the crystal back to temperatures near the Doppler limit within the normal cooling period. Collision events are detected by observing below normal fluorescence during the regular Doppler cooling stage. After detection of a collision, a short frequency

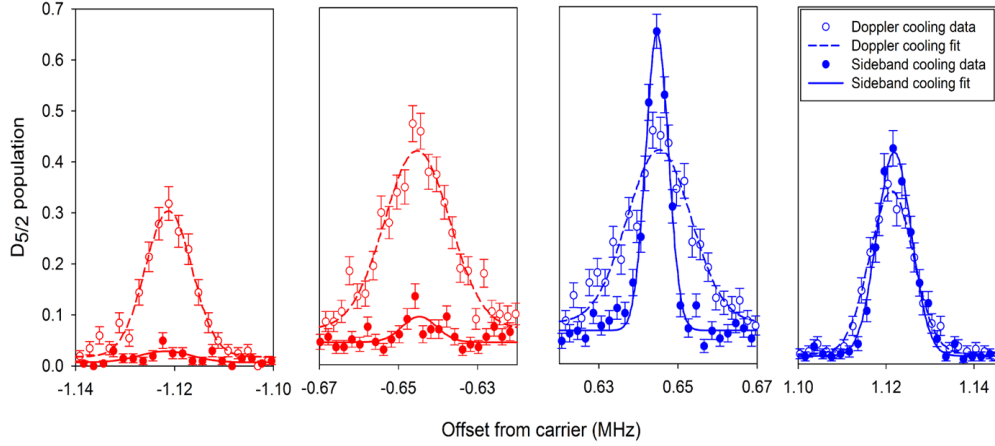


Figure 23: Measurement of the $S_{1/2} (m_j = -1/2) \rightarrow D_{5/2} (m_j = -5/2)$ first-order axial sidebands for the $^{40}\text{Ca}^+ - ^{40}\text{CaH}^+$ crystal by electron shelving. Red and blue sidebands are fit to a Gaussian of the same width but variable amplitude. The hollow circles correspond to the Doppler cooling results, and the full circles are the sideband cooling data. Comparison of sideband heights yields an average mode occupation of $\bar{n}_{\text{COM}} = 0.09 \pm 0.04$ for the center of mass mode and $\bar{n}_{\text{BM}} = 0.06 \pm 0.03$ for the breathing mode.

chirped Doppler cooling pulse is applied that recrystallizes the ion chain and achieves the desired initial temperature for performing sideband cooling. We discard the electron shelving data recorded coincident with the collision event from our final data set.

The experiment starts by optimizing the ground state cooling of a single atomic ion. After Doppler cooling, the sidebands are approximately the

same height. The temperature is measured to be $T = 0.75$ mK using the carrier Rabi oscillation decoherence method [58, 83], which is close to the Doppler cooling limit of $T = 0.53$ mK. Sideband cooling is performed on the axial mode and $\bar{n}_{\text{axial}} = 0.1$ is typically achieved as measured by the peak height comparison method [18]. Ground state cooling of the motion in three dimensions was not achieved due to an unusually high radial heating rate. We were only able to cool to $\bar{n}_{\text{radial}} = 1$ corresponding to 30% population in the ground state. This could be due to residual micromotion or stronger coupling between the fluctuating electric fields and the radial direction.

Our molecular ion results are presented in Fig. 23. After sideband cooling, we observe that the red peak height is greatly suppressed relative to the blue peak height. Peak height comparison reveals $\bar{n}_{\text{COM}} = 0.09 \pm 0.04$ and $\bar{n}_{\text{BM}} = 0.06 \pm 0.03$. To determine the temperature, we match the expected occupation of the oscillator as a function of temperature with the measured occupation. We find $T_{\text{COM}} = 12.6 \pm 0.02$ μK and $T_{\text{BM}} = 18.5 \pm 0.01$ μK , which is more than a factor of 3 below the Doppler cooling limit. The presented data is typical and similar results were seen even when imperfect compensation resulted in a shifted breathing mode frequency [49, 78].

5.3 Sideband cooling results

The sideband cooling results are an important step towards the implementation of quantum logic spectroscopy [51] or photon-recoil spectroscopy [57].

These techniques are limited by trap heating which acts as unwanted background that could mask the signal. For our current experiment, we measure a single ion background heating rate of 0.1 quanta/ms comparable with other experiments in similar scale traps [84]. The heating rate of the atomic and molecular ion on the center of mass mode was 0.3 quanta/ms. If this mode is used for spectroscopy, the heating rate provides an idea of how quickly the molecular ion must absorb or scatter photons to have a detectable signal.

5.4 *Summary*

We have shown sympathetic sideband cooling of $^{40}\text{CaH}^+$ co-trapped with a $^{40}\text{Ca}^+$ ion. We achieve $<16\ \mu\text{K}$ translational temperature for a molecular ion by demonstrating the sideband cooling of both axial modes. The similar masses of $^{40}\text{CaH}^+$ and $^{40}\text{Ca}^+$ maximizes the sympathetic cooling efficiency [24]. However, this method is general and can be extended to any combination of two ions with μ between 0.2 and 5 [85]. As an example of the range of the technique, the sympathetic ground state cooling of an amino acid (57-186 amu) by Ca^+ or small peptides containing up to ten amino acids by Yb^+ is possible.

The sideband cooling of molecules enables the high precision spectroscopy of molecular ions required for tests of fundamental physics. Our experiments make possible the measurement of rovibrational lines of $^{40}\text{CaH}^+$ to search for time variation in the ratio of the mass of the electron to the mass of the proton [36]. For these experiments, only a single, well-cooled normal mode is

required, and our observation of the near ground-state cooling of both axial modes of motion is more than sufficient.

CHAPTER VI

VIBRONIC SPECTROSCOPY OF CaH^+

This Chapter is based on the following article:

R. Rugango, A. T. Calvin, S. S. Janardan, G. Shu, and K. R. Brown, *ChemPhysChem* **17** (2016).

The large rotational constants of diatomic hydrides [66, 67, 68, 69] which slows blackbody rethermalization after rotational cooling combined with the availability of atomic coolants of similar masses make these molecular ions particularly well-suited to high precision spectroscopy measurements. Homonuclear diatomic molecular ions allow almost complete decoupling from blackbody radiation and are also a promising route towards tests of fundamental constants [86, 87, 88].

The detection of neutral CaH radicals in sun spots [89] suggests possible solar presence of CaH^+ . However, the spectroscopy vital to the detection of this molecular ion has been absent in contrast to other neutral metal hydrides. Short storage times and weak absorption and dispersion signals [90] pose intrinsic challenges to molecular beam spectroscopy, a limitation that has contributed to the lack of experimental data on CaH^+ . Within the last few decades, new trapping and laser-cooling techniques have made it possible to generate metal hydride ions with quantum state-controlled

chemical reactions between laser-cooled trapped atomic ions and molecular hydrogen [29, 34, 91]. These techniques have created a new opportunity for the spectroscopy of CaH^+ with the observation of a dissociative electronic transition [92] and ground state vibrational overtones [42].

Apart from being of astronomical interest, CaH^+ has much potential as a candidate for testing the time variation of fundamental physical constants. Vibrational and rotational transitions in molecules have different dependencies on the electron-to-proton mass ratio, $\sqrt{m_e/m_p}$ and m_e/m_p , respectively [8, 38, 39]. By comparing these transitions within one system, many systematic errors can be canceled. It has been previously proposed that the uncertainty in rovibrational frequency measurement in CaH^+ is on the order of the predicted astronomical time variation of m_e/m_p [93].

Despite the lack of experimental data, CaH^+ spectroscopy has been the subject of many previous theoretical studies. *Ab initio* calculations of vibrational dipole moments of metal hydrides [94] by Abe *et al.*, and subsequent calculations of potential energy curves of the electronic ground and excited states of the CaH^+ [36, 95] have offered theoretical guidance for our experiments. We report our measurement of the $1^1\Sigma \rightarrow 2^1\Sigma$ vibronic transitions by resonance enhanced dissociation between 370 nm and 421 nm.

6.1 Resonance enhanced multi-photon dissociation (REMPD) of CaH^+ ions

The setup used in this experiment was described in section 3.2. Photoionization of sublimed neutral Ca allows the trapping of a few hundred Ca^+ ions. Addition of H_2 gas to the vacuum chamber through a manual leak valve promotes the formation of CaH^+ through photo-activated reactions between Ca^+ and H_2 . Upon addition of hydrogen gas, the pressure in the chamber goes from 1.2×10^{-10} Torr to around 3×10^{-8} Torr. At these pressures, decrease in fluorescence on the photomultiplier tube (PMT) (Hamamatsu H7360-02) accompanied by the darkening of a large part of the Coulomb crystal on the CCD camera (Princeton Instruments Cascade 1K) indicates 50 to 100 reactions within a few minutes. The molecular ions are excited using a frequency-doubled Ti:sapphire laser. We achieve a 10% efficiency in laser power after doubling the IR beam through a 0.1 mm thick Foctek BBO crystal. The doubled beam enters along the trap axis, and dissociation of the molecular ions is detected by the increase in fluorescence, as well as the reappearing of the bright Ca^+ ions. Figure 24 outlines the transitions used for Doppler cooling Ca^+ ions.

The frequency-doubled Ti:sapphire is tuned between 370 and 421 nm. Theoretical calculations predicted [36, 95] that the $1^1\Sigma \rightarrow 2^1\Sigma$ transition would occur in this range, Figure 24. The bandwidth of pulses is measured for different wavelengths by an Ocean Optics spectrometer (model HR2000+)

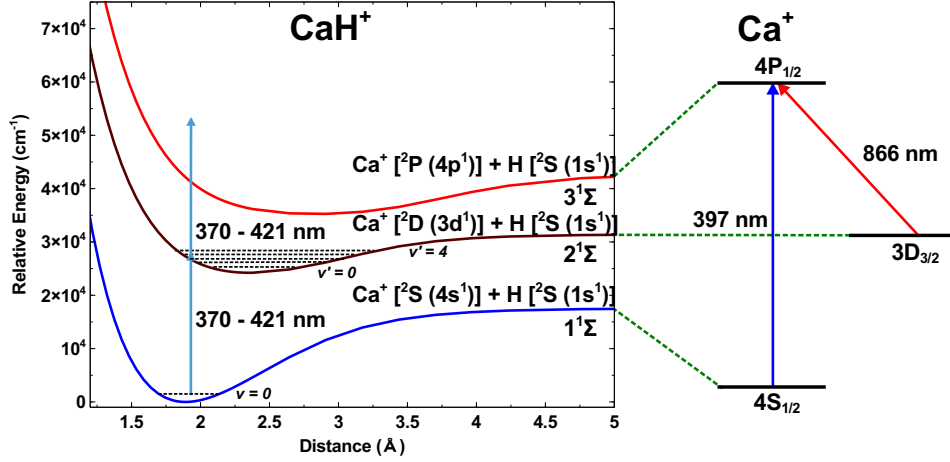


Figure 24: The three lowest $1^1\Sigma$ potential energy curves for CaH^+ are shown [36]. We measure vibrational lines using resonance enhanced dissociation. The first photon excites the molecules on the $1^1\Sigma \rightarrow 2^1\Sigma$ transition. A second photon could then dissociate the ion. The atomic asymptotes of the plotted molecular potentials lead to Ca^+ in different electronic states and H in the ground state. A simplified Ca^+ energy level diagram shows the states involved in Doppler cooling and how they correspond to the limits of the molecular states (energy not to scale). The 397 nm laser is the main Doppler cooling laser and the 866 nm laser repumps the metastable $D_{3/2}$ state.

and corresponds to a pulse length of 300 fs. The power is maintained at 20 mW for all wavelengths.

We measured the spectrum by repeatedly exciting the ions for 4 ms before detecting the fluorescence on the PMT for 2 ms as shown in Figure 25. The photon count is recorded as a function of time and the data is fit to a first order reaction rate equation to deduce the dissociation rate:

$$A_t = A_\infty - (A_\infty - A_0)e^{-\Gamma(\lambda)t}, \quad (32)$$

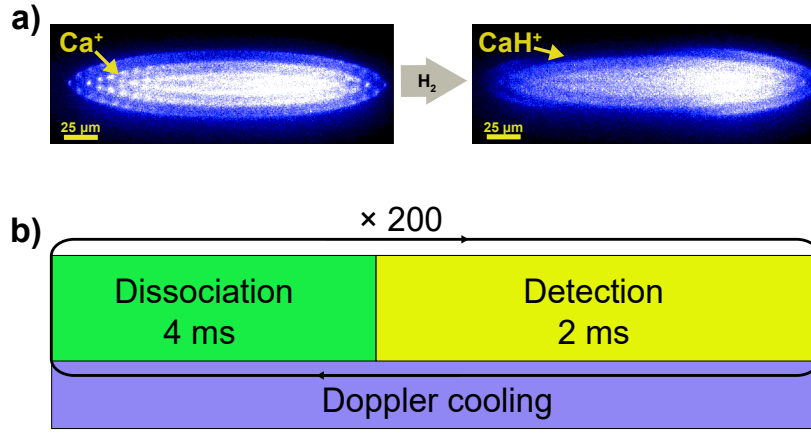


Figure 25: a) Coulomb crystal containing a few hundred Ca^+ ions react with H_2 to make 50 to 100 CaH^+ ions. The reaction is indicated by the darkening of the left side of the crystal. The asymmetry seen in the Coulomb crystal is due to the 397 nm radiation pressure on Ca^+ ions. b) The pulse sequence used to dissociate the molecular ions is shown. The Doppler cooling lasers remain on to avoid ion heating and losses. An AOM switches the dissociation beam.

where A_t is the fluorescence at time t , A_∞ is the steady-state fluorescence after dissociation, $\Gamma(\lambda)$ is the wavelength dependent rate, and A_0 is the initial fluorescence. An acoustic-optical modulator (AOM) switches the excitation beam on and off, but the wavelength is scanned manually. Figure 26 shows example fluorescence data for two different excitation wavelengths.

6.2 The vibronic spectrum

The spectrum acquired is based on the dissociation rate and we measured the four vibronic transitions shown in Figure 27. Every single point is an average of five measurements. These rates are repeatable for every wavelength with

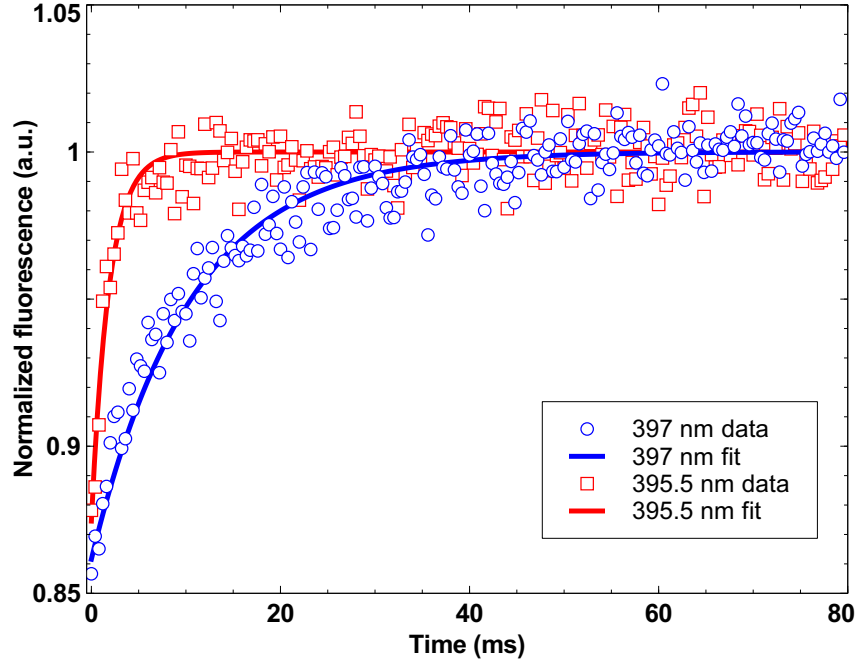


Figure 26: The measured fluorescence recovery curves for excitation at 395.5 nm and 397 nm are shown. The data is fit with a single exponential (Equation 32) and the fluorescence is normalized to the steady-state fluorescence parameter, A_{∞} , from the fit.

Table 1: Comparison of experimentally measured vibronic transition frequencies, $1\ ^1\Sigma(v = 0) \longrightarrow 2\ ^1\Sigma(v')$, and theoretical calculations. Experimental peaks were assigned based on agreement with theoretical predictions. With this assignment, the transition to $v' = 0$ was not measured and the experimental value is extrapolated from the measured peaks (Equation 36)

v'	$\nu_{0v'}$		
	CASPT2 [96]	CPP-CI [97]	Experiment
0	23887	23826	(23828)
1	24674	24594	24624 ± 13
2	25449	25330	25399 ± 19
3	26206	26067	26156 ± 14
4	26942	26782	26891 ± 6

low standard deviation between experiments as shown in the plot. To avoid variations in raw fluorescence data, we preferred using larger crystals than ion chains with the dissociation beam aligned along the axis of the trap for more homogeneous dissociation across the crystal.

Future single-molecule experiments could be performed in the same fashion as in Ref. [42]. For these experiments a single molecular ion would be cooled using one or two atomic ions. The dissociation laser would be applied and the time to dissociation measured. An average dissociation rate for each excitation wavelength is determined by collecting statistics from a series of single molecular ion experiments. The rate of data collection is slow compared to the large crystal approach used in this paper, but the high signal-noise ratio of the single molecular ion experiment can be advantageous for measuring slow dissociation rates.

We assigned peaks based on theoretical predictions in the literature using

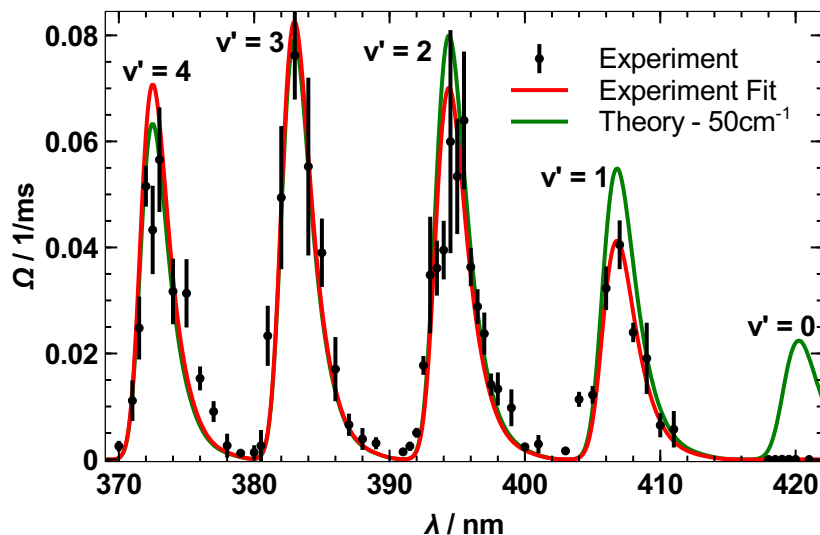


Figure 27: The dissociation rate as a function of excitation wavelength. The error bars are standard deviations over the five measurements. A model that assumes the dissociation rate is limited by the absorption of the first photon is used to plot the theoretical curves and to find the experimental fit. The theory model is based on CASPT2 [31] but all peaks are red shifted by a constant 50 cm⁻¹.

a complete-active-space approach (CASPT2) [96] and a core pseudopotential - configuration interaction approach (CCP-CI) [97]. The CASPT2 transition frequencies are blue-shifted and the CCP-PI transition frequencies are red-shifted relative to the data, Table 1. The CASPT2 predicted transition frequencies differed from the measured transition frequencies by a consistent $\approx 50 \text{ cm}^{-1}$, which is well within the expected theoretical error based on differences between the calculated asymptotes and the measured atomic spectra of $\approx 100 \text{ cm}^{-1}$ [98]. The difference between the CPP-CI transitions and the measured transitions was less consistent and varied between 30 and 110 cm^{-1} . Using this assignment, the $1^1\Sigma, \nu = 0 \longrightarrow 2^1\Sigma, \nu' = 0$ transition was not observed. The experimental peaks showed the expected asymmetry for a system with a smaller rotational constant in the excited state.

6.2.1 Theoretical model for estimation of experimental parameters

In order to determine the bare vibrational frequency, we modeled our predicted spectra assuming the ion starts in the ground electronic and vibrational state, but a thermal distribution of rotational states. We truncate the rotational states at $J = 15$ which is expected to only have a population of 0.003% at room temperature. We then calculate the excitation rate using Einstein B coefficients and the spectral density of the doubled Ti:Sapphire. The molecular ion is assumed to instantaneously dissociate after it is excited to the $2^1\Sigma$ state.

The rate is calculated as the sum of individual rotational absorption rates multiplied by the thermal probability of being in that state:

$$\Gamma(\lambda) = \sum_{J,v',J'} B_{0,J,v',J'}(\lambda) p(0, J) \quad (33)$$

where B is the Einstein stimulated absorption coefficient when the laser is at wavelength λ and $p(0, J)$ is the probability of being in the ground vibrational state with the rotational state J assuming a Boltzmann distribution. The Einstein B coefficient is given by:

$$B_{0,J,v',J'}(\lambda) = \frac{I_\lambda(f)}{c} \frac{A_{x,0}}{8\pi h f^3}, \quad (34)$$

where $I_\lambda(f)$ is the intensity of laser at frequency F , f is the transition frequency from $1^1\Sigma, v = 0, J \longrightarrow 2^1\Sigma, \nu', J'$, and $A_{v',J',0,J}$ is the Einstein A coefficient. Each Einstein A is calculated as:

$$A_{v',J',0,J} = \frac{16\pi^3 S(J, J')}{3\varepsilon_0 h} f^3 \mu_{v',0}^2, \quad (35)$$

where J is the ground state rotational quantum number, $S(J, J')$ is Hönl-London factor for a rotational transition $J \longrightarrow J'$, and μ is the transition dipole moment.

The data for the laser profile was determined by measurement and fitting to a Gaussian profile commonly used to describe femtosecond laser pulses [99, 100]. The fitting yielded a full width at half maximum of 180 ± 10 cm^{-1} . The maximum laser intensity for the calculation was left as a free

parameter to scale the theory to the data. The scaled intensity accounted for uncertainties in the laser beam shape at the ion crystal and the theoretical transition dipole moments. The rotational constants for the excited vibronic levels were calculated using the LEVEL8.2 program [101] and the potential energy surfaces of Ref. [96]. All other constants were provided by [96]. Initially, nearly all molecular ions are in the vibronic ground state which means only the $\nu = 0$ vibrational state is needed for calculations.

Figure 27 shows the expected theoretical plots for the CASPT2 with a 50 cm^{-1} red shift. One observes quantitative agreement with the experimental peak positions and almost quantitative agreement with the peak heights with the notable exception of the $v' = 0$ state. Our hypothesis is that this is due to the second part of the dissociation process which needs to be further investigated.

To find our experimental fit, we set the rotational constants to the theoretical values and allow the vibrational transition frequency and dipole matrix element (which controls the peak height) to vary. The nonlinear regression was done by applying Nelder-Mead Minimization Algorithm [102] to the χ^2 value using a C++ library [103]. This yields our experimentally determined transition frequencies (Table 1).

6.2.2 Experimental spectroscopic constants

From our experimental calculation, we determine the anharmonicity constant ($\omega_e x_e$) of the molecular ion in the $2^1\Sigma$ state. We fitted both the theoretical

vibronic frequencies and our measured spectra to the following equation to determine $\omega_e x_e$ as shown in Figure 28:

$$\nu_{0v'} = \nu_{00} + \omega_e v' - \omega_e x_e v'(v' + 1), \quad (36)$$

where $E(n)$ is the total vibronic energy, and ν_{00} is the energy of the $\nu = 0 \rightarrow \nu' = 0$ transition; and ω_e is the harmonic constant for the $2^1\Sigma$ state. The theoretical vibronic frequencies used in the fit are from Ref. [96]. Table 2 shows our calculated value for the $\omega_e x_e$ and how it compares to the CASPT2 theoretical results. The fit in Figure 28 yielded a value of $10.0 \pm 0.2 \text{ cm}^{-1}$ for the anharmonicity constant, which is similar to the deduced theoretical prediction of $8.6 \pm 0.3 \text{ cm}^{-1}$. The harmonic constant turned out to be $815.8 \pm 1.3 \text{ cm}^{-1}$; comparable to the theoretical value of $807 \pm 1.7 \text{ cm}^{-1}$. This value also matches the most recent calculations by Aymar and Dulieu [95]. Furthermore, the fit in Figure 28 predicts the ν_{00} frequency to be $23828 \pm 1.2 \text{ cm}^{-1}$ but we did not observe a signal at this frequency.

Our results are a step closer to the the implementation of rotational cooling on CaH^+ as well as quantum logic spectroscopy on rovibrational transitions in the molecule.

6.3 Summary

We have measured the vibronic spectrum of the $1^1\Sigma \rightarrow 2^1\Sigma$ transition in CaH^+ using resonance enhanced dissociation. The observed peaks were assigned based on previous calculations, which are a reasonable match to

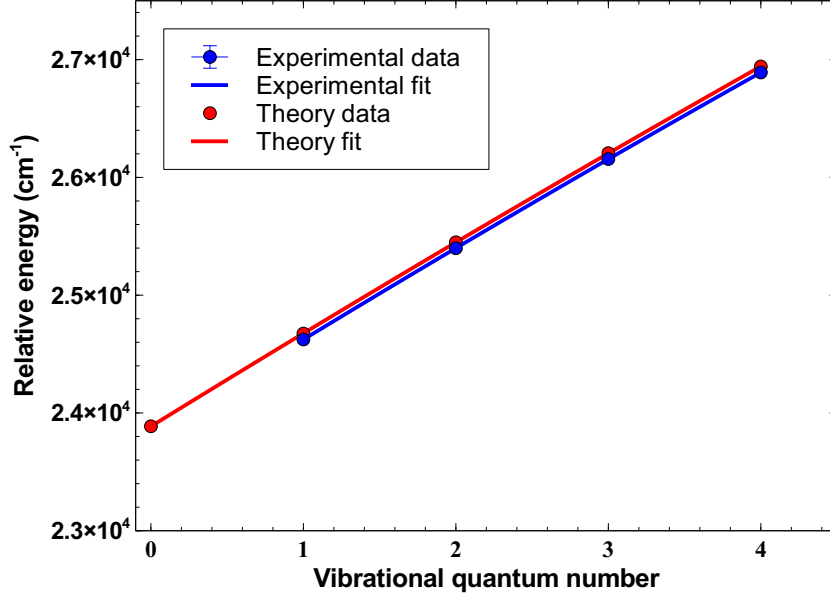


Figure 28: Theoretical and experimental values for $\omega_e x_e$ and ω_e for the the $2^1\Sigma$ state of CaH^+ were calculated by fitting the plotted transition energies for $1^1\Sigma(v=0) \rightarrow 2^1\Sigma(v')$. The *ab initio* theoretical energies are taken from Ref. [96].

Table 2: Table comparing the experimental and theoretical values of the anharmonicity constant as well as the harmonic constant for the $2^1\Sigma$ state of CaH^+ based on fitting Equation 36 to the first five states. The uncertainties are the errors from the fit. We observe good agreement between the experimental and theoretical values for all the constants.

Constant	Experiment	CASPT2 [96]
$\omega_e x_e$	$10.0 \pm 0.2 \text{ cm}^{-1}$	$8.6 \pm 0.3 \text{ cm}^{-1}$
ω_e	$815.8 \pm 1.3 \text{ cm}^{-1}$	$807 \pm 1.8 \text{ cm}^{-1}$
ν_{00}	$23828 \pm 1.2 \text{ cm}^{-1}$	$23886 \pm 1.2 \text{ cm}^{-1}$

the measured results for both the energy spacing between peaks and the expected widths. Our own theoretical modeling of the relative peak intensities agrees with the experimental results with the notable exception of the $\nu = 0 \longrightarrow \nu' = 0$ transition. We attribute this discrepancy to the inaccuracy of theoretical methods.

KH is isoelectronic to CaH^+ and the lowest vibrational states of the $2^1\Sigma$ state have not been observed by absorption or fluorescence due to small transition moments [104, 105, 106]. These missing vibrational peaks initially resulted in a misassignment of the vibrational levels. The correct assignment required measuring the KD spectra and comparing the experimentally derived potential energy surfaces for KH and KD [104, 106]. We measured the vibronic spectrum of CaD^+ (section 8.1), which allowed us to revise our peak assignments for CaH^+ .

Experimental and theoretical studies on possible dissociation pathways from the $2^1\Sigma$ state could shed more light on relative peak intensities. One theory is the dissociation process involves excitation to the $2^1\Sigma$ state followed by photon emission back to an excited vibrational $1^1\Sigma$ state before photodissociation. Alternatively, the dissociation could be due to predissociation [107] from the $2^1\Sigma$ state to the $1^1\Sigma$ state, but we expect this rate to be slower than fluorescence. In order to unravel these possible pathways, one can look for laser-induced fluorescence when driving these vibronic transitions and also design experiments to measure the electronic state of the dissociated Ca^+ .

We also extended our measurement technique to observe rovibronic lines

in CaH^+ by narrowing the spectrum of our laser source (section 8.2). The measurement of rotational lines is vital for testing the preparation of the molecular ions in their rotational ground state using optical pumping methods. This internal state control, combined with our previous realization of the ground state cooling of axial modes of molecular motion [108], will facilitate the implementation of quantum logic spectroscopy on CaH^+ . In addition, our experimental method can be used to measure the rovibronic spectrum of other alkali-earth monohydride ions with the appropriate laser-cooling ion, as well as the deuterated forms of these molecules.

Regarding state preparation, some optical pumping schemes for rotational cooling will require a good knowledge of the rovibrational spectrum for the ground electronic state. By using a $1+2'$ resonance enhanced multi-photon dissociation scheme, it is possible to measure the fundamental rovibrational transitions in the $1^1\Sigma$ state by sweeping the frequency of the first photon from a $6.9\text{ }\mu\text{m}$ laser. The second photon would excite to one of the $2^1\Sigma$ vibrational states, and the third photon would dissociate the molecules [37, 109]. An IR laser source with a wide tuning frequency would enable the measurement of multiple overtones as well.

CHAPTER VII

TRAPPING AND SYMPATHETIC COOLING OF BORON IONS

This Chapter is based on the following article:

R. Rugango, M. Sinhal, G. Shu, and K. R. Brown, arXiv:1609.09521 [physics.atom-ph] (2016).

Boron atomic ions, with their Be-like electronic structure, are a potential candidate for a high precision atomic clock [110] with a predicted blackbody uncertainty close to 1×10^{-18} at room temperature [111]. Directly laser-cooling B^+ is challenging due to the required short wavelengths to drive the transitions. A B^+ ion clock could be built using another laser-cooled atomic ion for both cooling and readout following the success of the Al^+ clock [51, 52, 53]. The four-electron closed-shell electronic structure of B^+ ions also makes them good candidates as sensors for the analysis of astrophysical plasmas [112]. Boron clusters and boron-hydrides are also of wide interest due to the importance of B in materials fabrication [113, 114]. B_n^+ ions have been previously loaded into ion traps using ablation of a boron target [115, 116, 117] and we use this method to load B_n ions into a trap containing laser-cooled Ca^+ ions.

Here we present the sympathetic cooling and trapping of B^+ , B_2^+ , and B_3^+

by Ca^+ ions. The B_n^+ ions are produced by ablating a target of pure elemental B and the ions are identified by modulating the fluorescence through resonant excitation of the motion. Peaks compatible with boron hydride ions are also occasionally observed, but not reliably produced. In the next section we describe our production and characterization techniques. In section 7.2 we discuss our observations and the relative occurrence of different ion species. Finally we conclude with some remarks on future experiments.

7.1 Loading and detection of boron ions

The experimental setup is the same as the one in the previous Chapter. We typically use a RF voltage of 198 V oscillating at 19.35 MHz to confine ions radially. At this frequency, low Mathieu q values for both stable $^{11}\text{B}^+$ ($q_{B^+} = 0.23$) and $^{40}\text{Ca}^+$ ($q_{\text{Ca}^+} = 0.064$) ions are achieved. These trap parameters result in a radial secular frequency of 0.44 MHz for Ca^+ . The trap voltage is varied between 148 V and 198 V corresponding to secular frequencies of 0.33 to 0.44 MHz. The Mathieu a parameter is estimated to be <0.001 for Ca^+ .

The Ca^+ ions are loaded by photoionizing neutral, thermally-evaporated Ca with 423 nm and 379 nm lasers or by ablating a Ca target using a 355 nm nanosecond YAG laser (Continuum minilite II) [118]. The boron ions are subsequently trapped by ablating the target mounted next to the Ca target. We monitor the power of the YAG to avoid too many hot boron ions that would destabilize the already trapped Ca^+ crystal. We maintain the power around 6 mW corresponding to 6 mJ/pulse for fast loading of boron

ions and to prevent loss of the Ca^+ crystal. A CCD camera (Princeton Instruments Cascade 1K) and a photomultiplier tube (Hamamatsu H7360-02) are used to image and count the fluorescence of the Ca^+ ions. The Ca^+ ions sympathetically cool the B^+ ions and facilitate their trapping.

The dark boron ions are detected using the motional resonance coupling method [8, 119] by applying an oscillating voltage on the top center electrode of the trap and observing changes in the fluorescence as function of the oscillation frequency. The radial motion of a single ion scales as the charge to mass ratio, Q/m , and in a crystal ions of different mass form bands near the bare resonance frequency. This method has been used to observe many sympathetically-cooled species such as HD^+ [120], BeH^+ [33], C_{60}^+ [121], $\text{C}_6\text{H}_5\text{NH}_2^+$ [122], Zn^+ , $^{44}\text{Ca}^+$, and Ga^+ [25]. Typical shifts in terms of $\Delta(Q/M)$ of up to 25 % due to both Coulombic interaction and around 10 % due to stray-fields mixing modes [123] have been observed. To minimize these shifts, we compensate for stray fields using the time-average average position and the fluorescence modulation techniques [81, 124] and weakly confine the ions in the axial direction to reduce the strength of the Coulomb interaction. In addition, compensation for excess electric fields reduces heating due to driven RF motion, known as micromotion.

7.2 Results and Discussion

Our reference for mass determination is a single $^{40}\text{Ca}^+$ ion with a secular frequency set between 0.33 MHz and 0.44 MHz. Initial ablation of Ca^+ yields

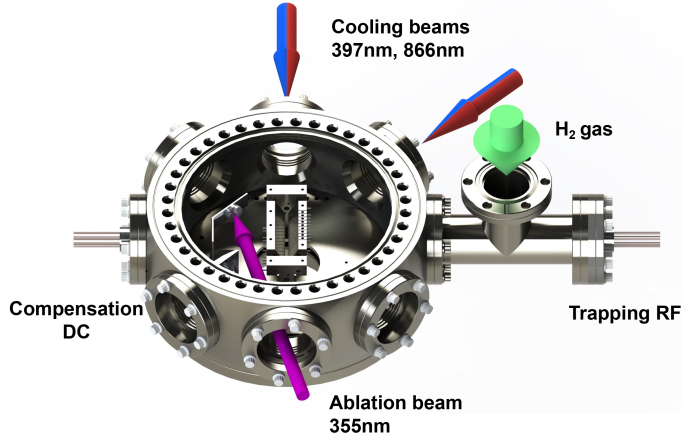


Figure 29: The experimental setup including the main vacuum chamber and the trap is shown. The 355 nm YAG minilite II is focused on B target is mounted right next to the Ca target about 40 cm from the trap center. The cooling beams (397 nm and 866 nm) used to Doppler cool the ions enter the trap axially and radially.

a motional frequency spectrum with a single band at the expected location with a width of 3 kHz for a typical applied excitation voltage of 0.35 V. Ablation of the B target then introduces extra peaks into the spectrum. An example of motional frequency spectra before and after ablating the boron target are shown in Fig. 30. We consistently see two weak peaks and a strong peak with a shoulder. These features are consistent with $^{10}\text{B}^+$, $^{11}\text{B}^+$, B_2^+ , and B_3^+ . The secular frequencies that we measure after trapping boron species are within 10 % of the expected values. Since the frequency spacing scales as $\Delta M/M_1 M_2$ for singly charged ions, the resolution is better for lighter ions and prevents us from distinguishing isotopically distinct molecular ions.

The mass of the trapped ions determines their stability in the trap as well

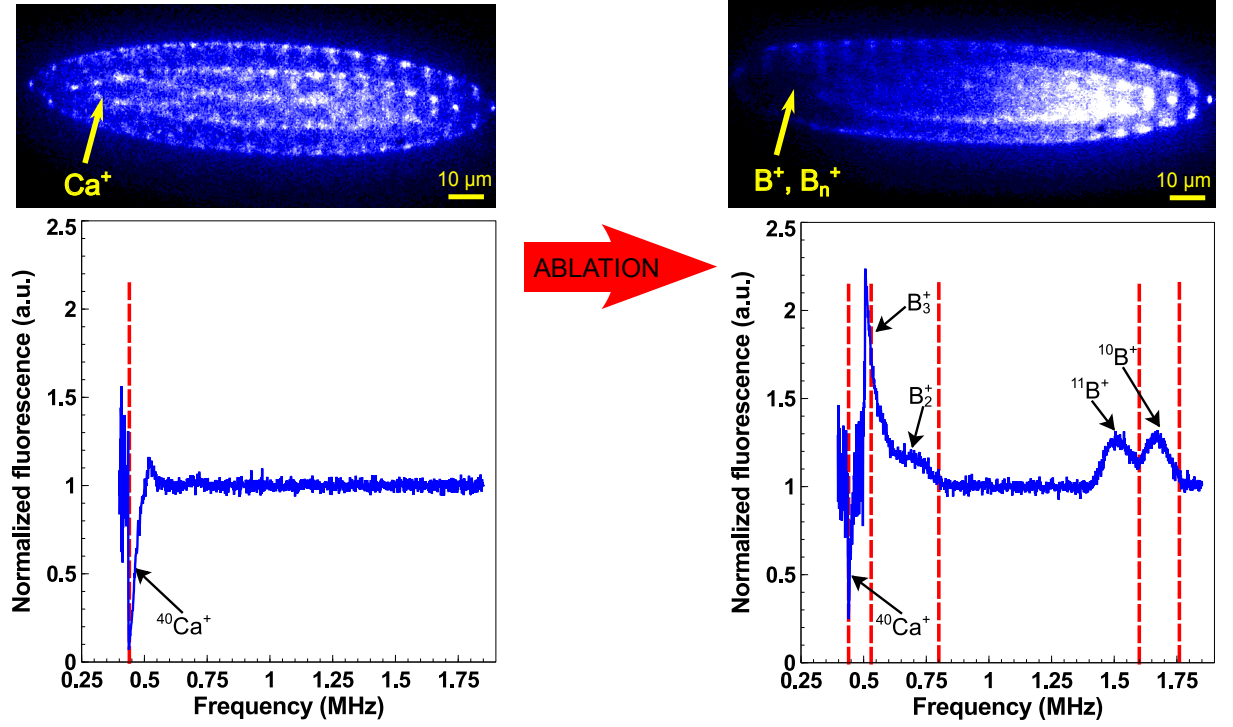


Figure 30: Ion crystals containing about 200 Ca^+ ions with their corresponding motional resonance scans before and after ablation of the boron target. The boron species are located towards the center of the crystal due to a lower mass-to-charge ratio, and the secular frequencies for different ions are inversely proportional to their m/q . The vertical bar are the predicted secular frequencies for each ion. One can observe that the peak positions are within 10% of their predicted values. In this figure, ω_{Ca^+} is set to 0.44 MHz and $q_{\text{B}^+}=0.23$

Table 3: A table showing the trapping of different ion species by ablation and their occurrence for 10 consecutive loading events. The last column shows how many times a species is observed out of ten motional resonance scans on different crystals. The peak observed between 13.6 and 14.6 amu has not been identified but could correspond to BH_2^+ . The $^{10}\text{B}^+$ isotope appears less frequently and its peak is usually shorter than that of $^{11}\text{B}^+$. The shifts from the predicted peak positions are due to Coulombic interactions between the ions.

Assignment	Predicted (MHz)	Actual (MHz)	Mass range (amu)	Occurrence
$^{10}\text{B}^+$	1.48	1.40	10.2 - 11.0	6
$^{11}\text{B}^+$	1.34	1.28	11.0 - 12.3	10
B_2^+	0.67	0.62	21.1 - 27.9	8
B_3^+	0.45	0.45	30.8 - 37.9	10
Ca^+	0.37	0.37	38.0 - 42.2	10
Unknown	-	1.05	13.4 - 14.9	1

as sympathetic cooling efficiency. Consequently, those with masses similar to that of $^{40}\text{Ca}^+$ are the most stable. Fig 30 shows typical motional resonance scans before and after loading boron species. We observe a strong signal from B_3^+ due to its mass similarity with Ca^+ . Furthermore, previous studies on B_3^+ have also shown it to be a relatively stable cluster compared to its lighter counterpart (B_2^+) [115]. We are also occasionally able to detect both isotopes of boron as shown in Fig. 30, but we are unable to resolve or detect the clusters based on both isotopes.

To determine the reliability of the ablation method for producing different B_n^+ species, we performed 10 consecutive experiments where a new Ca^+ ion crystal of 200-300 ions was loaded before the boron target was ablated. The resulting mass excitation spectrum are shown in Fig. 31 and the summary of detected species is presented in Table. 3. We have found the atomic and molecular boron ions are consistently loaded. In addition an unassigned peak that could correspond to BH_2^+ [125, 126] was observed. The $^{10}\text{B}^+$ isotope is loaded less frequently but at a rate higher than its natural abundance. Such isotope enrichment in ablation plumes has been previously noted for boron targets and other species like titanium, zinc, copper, and gallium [127, 128].

We have observed that the detected peaks change dynamically with time. First, we have observed that the $^{11}\text{B}^+$ ions are stable at both $q_{B^+} = 0.23$ and $q_{B^+} = 0.18$. Shorter lifetimes for $^{11}\text{B}^+$ ions are occasionally observed when collisions with background gas surge. A titanium sublimation pump is used to lower the rate of those collisions. Second, although we normally

observe the shoulder feature that we associate with B_2^+ directly after ablation, it occasionally grows in at longer times (Fig. 32). We have not seen a correlation between the growth of this shoulder and loss of signal in other peaks. One possible explanation could include dissociation or ionization of B_4^+ ions that are hidden by the Ca^+ transition or charge exchange of Ca^+ with background gases. A complete understanding of the process requires improved Q/M resolution in this region. Finally, we also occasionally see a broadening of the B^+ peak that could represent BH^+ (Fig. 32). Out of hundreds of loading events, we have only observed such a peak twice. Increasing H_2 pressure up to 1×10^{-7} Torr did not yield additional BH^+ .

BH^+ has an internal structure that is potentially suitable for Doppler cooling with a few lasers [62], but its gas phase production has been limited by the high melting point of elemental B [129] and the high activation energies needed for reactions [130]. Also, unlike other metal hydrides ions which can be produced from photoactivated reactions between laser cooled atomic ions and H_2 [29, 33, 34], B^+ has not been laser cooled yet. Previous methods of BH^+ production in the gas phase relied on hazardous precursors such as B_2H_6 [131] and BF_3 [130]. An alternate method has been used to generate neutral BH molecules [132] from reactions between laser ablated atoms and H_2 . In this process, atoms are excited to higher electronic states where collision reactions with H_2 are energetically favorable [132, 133]. At the H_2 pressures tested here, we were unable to reliably generate BH^+ .

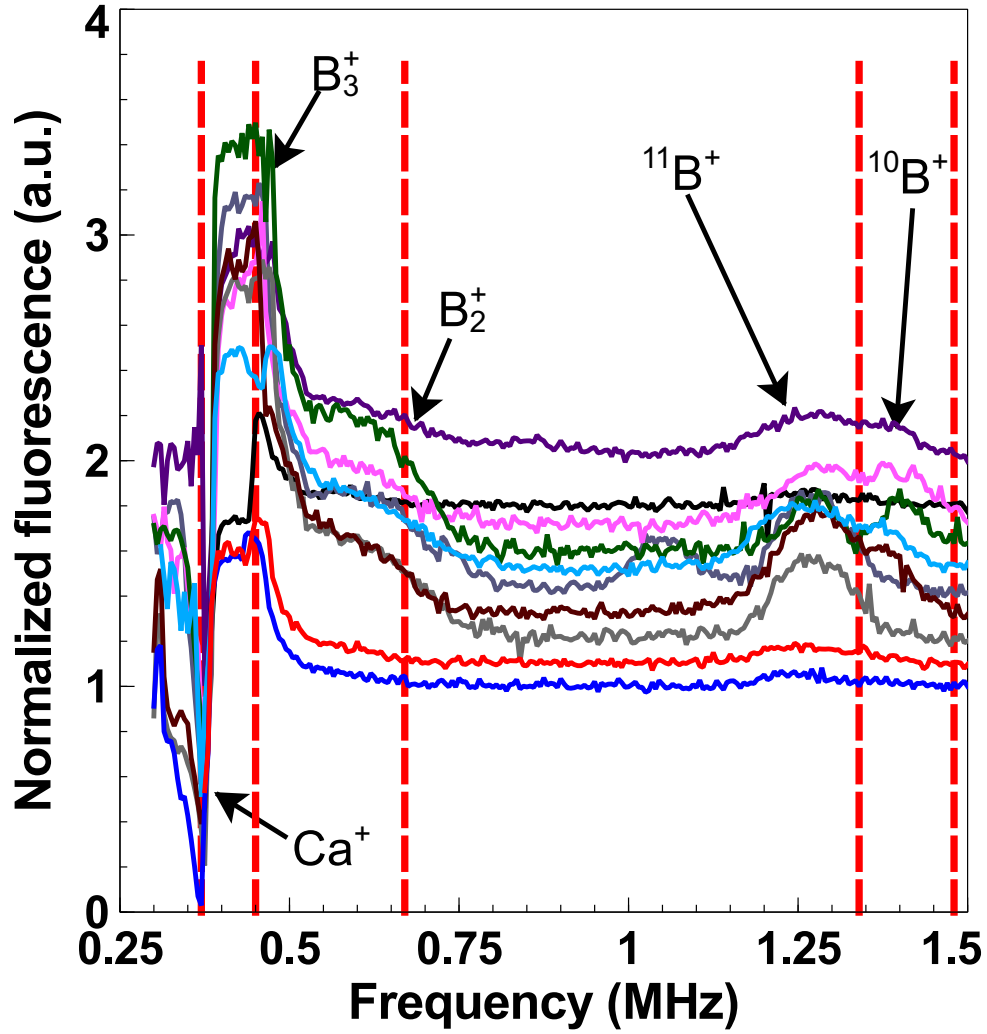
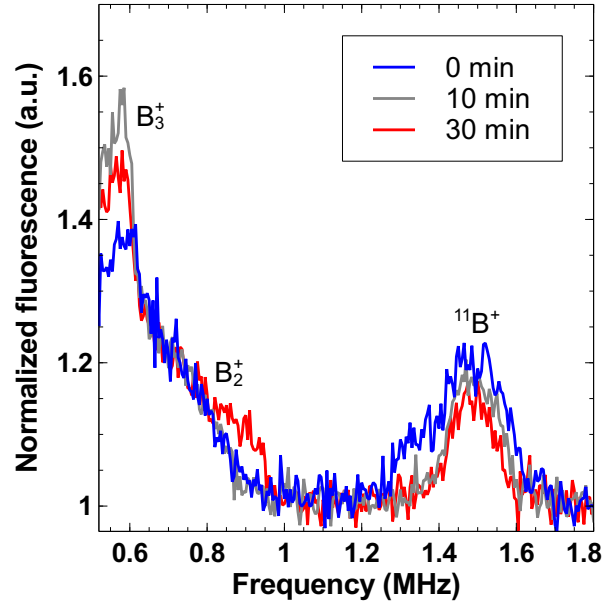
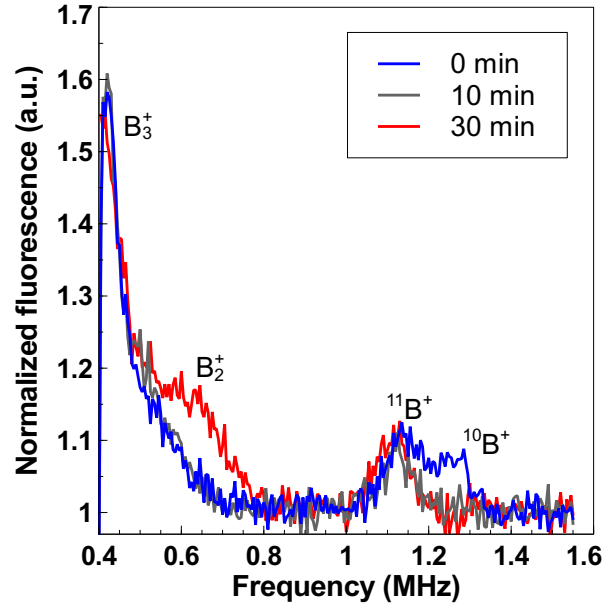


Figure 31: Motional excitation scans are depicted for 10 consecutive experiments. For each experiment, a new Ca^+ crystals is loaded and the B target is ablated 10 times. On the y-axis the plots are offset from each other by 0.1 units. The features corresponding to B_3^+ and $^{11}\text{B}^+$ are observed in every scan. The difference in peak heights between different scans stems from the fact that ablation does not allow control over the amount of dark ions loaded in each crystal.



(a) $q = 0.23$



(b) $q = 0.18$

Figure 32: The motional excitation can change with trapping time. As seen in a) and b), the shoulder feature that we associate with B_2^+ can appear a long time after ablation. This could be either due to dissociation of B_4^+ whose presence is hidden by the Ca^+ line or charge exchange with background gas. The shoulder off the $^{11}B^+$ peak in a) is compatible with BH^+ but the feature has a short lifetime and is rare. The features corresponding to B^+ and B_3^+ are observed to be relatively stable over thirty minutes.

7.3 *Summary*

We have demonstrated the trapping and sympathetically cooling of B^+ ions by laser ablation. We confirm their presence non-destructively using the motional resonance coupling method. We have also generated various molecular ions (B_2^+ , and B_3^+). Our findings provide new opportunities for experiments on a B^+ ion-based atomic clock. With the help of theoretical predictions [134, 135], these crystals could be used to explore the spectroscopy of the cluster ions.

The sensitivity and resolution of our measurement method can be enhanced by addition of a time-of-flight mass spectrometer (TOF) to our system [136]. The TOF would provide a quantitative measure of the number and types of trapped ions. This will be critical for understanding the trap dynamics that we have observed.

The lifetime and sympathetic cooling of B^+ within Ca^+ crystals suggest that this system will be good for performing high-precision spectroscopy of BH^+ as the next steps towards direct Doppler cooling of BH^+ ions. The report of neutral AlH from laser vaporization of $LiAlH_4$ [137] suggests that ablation of $NaBH_4$ will result in neutral BH that can then be photoionized [131]. In this case, ionized species generated from laser ablation would be kept out of the trap using an electric field outside the trap.

CHAPTER VIII

CONCLUSIONS, CURRENT AND FUTURE PROJECTS

This thesis presents different experimental results geared towards high precision rovibrational spectroscopy of molecular ions. First, we have demonstrated the cooling of all three normal modes of a single Ca^+ to μK temperatures. Our sideband cooling of the refrigerant atomic ion allowed us to move forward to the ground state cooling of a molecular ion. In addition, the quality of sideband cooling in the radial directions can help us to fine-tune our compensation for excess micromotion. Secondly, we achieved the ground state cooling of CaH^+ to the coldest temperature ever recorded for molecular ion motion. This result is important for doing quantum logic or photon recoil spectroscopy of molecular ions. Next, we showed the first-ever measured vibronic transitions in CaH^+ in an effort to provide some preliminary frequencies for our future spectroscopic endeavors. Our results, combined with our sideband cooling results, make photon recoil spectroscopy on CaH^+ much more feasible. In addition to our work on CaH^+ , we have demonstrated some progress towards trapping and laser-cooling BH^+ ions by first trapping and sympathetically cooling B^+ ions. Boron cluster ions which have also been produced as side-products. Our current results have permitted us to

complete a few other projects and anticipate other experiments in the future.

8.1 Vibronic spectroscopy of CaD^+ ions and peak re-assignment for CaH^+

The vibronic spectrum of CaH^+ ions shown in Chapter 6 leaves an unanswered question of why the $v' = 0$ peak was unobserved as predicted by theoretical calculations. One of the plausible explanations to this discrepancy between theory and experiment is missassignment due to inaccuracy in theoretical predictions of the potential energy curves. Although unexpected for such a small molecule, a similar trend has been previously observed with isoelectronic KH. The vibronic spectra of KH were initially missassigned and were corrected only after vibronic spectroscopy of KD molecules [104].

For this reason, we have measured vibronic lines in CaD^+ to determine the correct vibronic numbering of the $1^1\Sigma \rightarrow 2^1\Sigma$ in $\text{CaH}^+/\text{CaD}^+$ ions. We use the same scheme outlined in fig. 25 to measure dissociation rates. The results we got point to an initial misnumbering of the vibronic lines in Chapter 6 thus confirming that the $v' = 0$ had been detected by our method. In figure 33, the old peak assignment resulted in two different shifts between experiments and theory for CaH^+ and CaD^+ molecular ions. For CaH^+ spectra, the experimental spectrum is 50 cm^{-1} red-shifted from theoretical spectra while the experimental CaD^+ spectra are blue-shifted by 100 cm^{-1} from theoretical calculations. By blue-shifting both experimental spectra by 687 cm^{-1} , we observe a good match with theoretical spectra on both fronts.

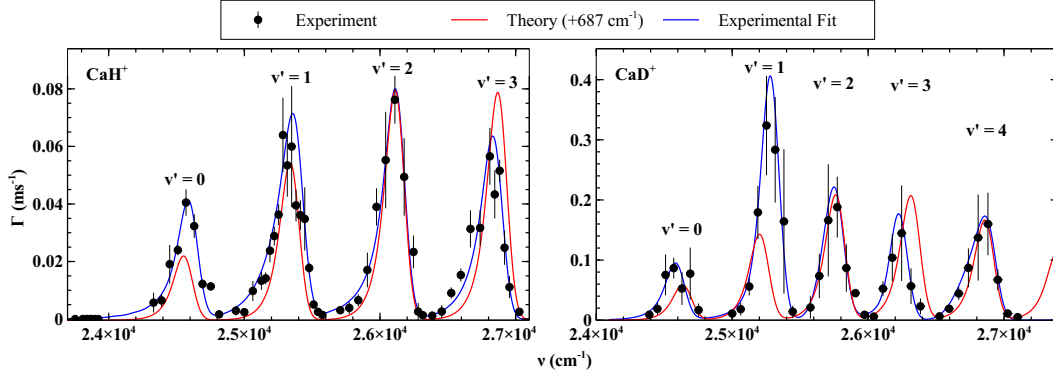


Figure 33: Plot used to assign vibronic peaks in both CaH^+ and CaD^+ ions. The red plot is the theoretical spectra adjusted to fit both CaH^+ and CaD^+ vibronic experimental data. The blue plot is the experimental fit. The 687 cm^{-1} shift on the theoretical spectra matches both experimental spectra and is consistent with a reassignment of the vibronic peaks.

This result suggests renumbering our previous peak assignment by lowering every quantum number by one.

8.2 Measurement of rovibronic transitions in CaH^+

Our results on the vibrational spectrum of CaH^+ are unable to resolve rotational transitions because of the broad linewidth of the frequency-doubled Ti-Sapphire beam ($\sim 180 \text{ cm}^{-1}$). The linewidth of pulsed lasers can be narrowed by means of pulse shaping techniques.

8.2.1 Pulse shaping techniques

Multiple techniques have been at the forefront of pulse narrowing in the last few decades. Initial applications of pulse shaping methods were first demonstrated for picosecond pulses by Froehly using a dispersive grating

pair for spatial filtering [138]. A non-dispersive apparatus was later used on femtosecond lasers by Weiner *et al.* achieving a resolution of higher than 1000 [139]. Higher resolution have been reported using spatial light modulators (SLM) [140]. The spectrally narrow waveform is generated by spatially clipping the spatially dispersed frequency spectrum of the pulsed laser. A diffraction grating spatially separates the individual frequency components of the incident beam by angle and focuses them on diffraction limited spots on a convex lens. This lens performs a Fourier transform from angular separation to spatial dispersion. At this point, amplitude and phase masks (or narrow slit) manipulate or select different Fourier optical components before a second lens (preferably of the same focal lens as the first one) and another grating recombines all the frequencies into a collimated beam. This technique is called Fourier transform femtosecond pulse shaping and is currently being used in our lab to gather rovibronic spectra of CaH^+ . Our experiment is slightly modified from the above description in that it only uses one grating (Thorlabs GH25 with 3600 lines/mm), one cylindrical lens ($f = 500$ mm), and an additional mirror positioned behind a $76\text{ }\mu\text{m}$ slit.

The frequency spectrum of the outgoing beam is measured using an Ocean optics spectrometer mentioned in Chapter 6, but with limited resolution (around 1 nm). To measure the frequency of the pulse shaped beam more precisely, we use a calibration curve which shows the change in center frequency on the spectrometer as the position of the slit is moved horizontally in the direction perpendicular to the beam. The calibration data points are fitted

to linear function which is used for calculating the frequency of the beam at a given slit position.

8.2.2 Rovibronic lines using REMPD

This experimental scheme is very similar to the one described in fig. 25. The pulse shaped laser beam dissociates the CaH^+ ions for 80 ms, and the change in fluorescence is repeatedly measured and fitted to equation 32. The longer dissociation time is required to compensate for the loss of power after pulse shaping. Typical powers of 100 μW are used for these measurements. The frequency is changed to address different rotational lines by changing the slit position horizontally along the cross-section of the beam.

8.2.3 The rovibronic spectrum

We assign experimental rotational lines based on theoretical peak positions generated using the following equation:

$$F(J) = B_v J(J + 1) - D_v [J(J + 1)]^2 \quad (37)$$

where $F(J)$ is the rotational energy of a given rotational state, B_v and D_v are the rotational constant and the distortion constant of the vibronic state respectively. The theoretical molecular constants were calculated using the LEVEL8.2 program [101]. To find experimental molecular constants we used the Nelder-Mead Minimization Algorithm [102] to the χ^2 value (difference between theoretical and experimental rovibronic peak positions) using a C++ library [103].

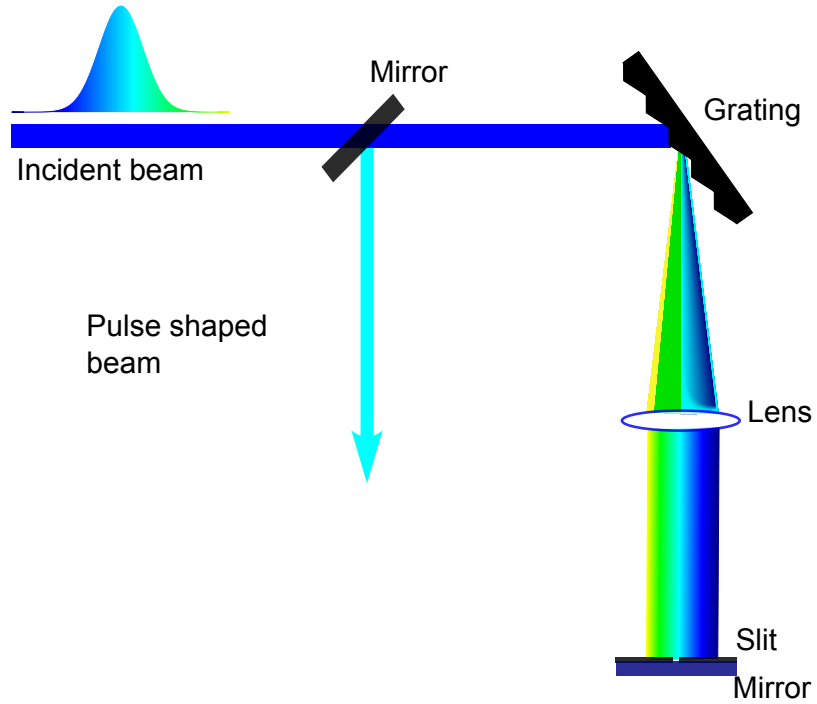


Figure 34: A schematic shows a simplified apparatus for pulse-shaping. An incident pulsed beam with a Gaussian frequency profile is diffracted by a grating, and a cylindrical lens focuses the individual Fourier components onto a slit or mask. A mirror behind the slit reflects the beam back through the lens to the grating, which recombines the frequency components of pulse shaped beam. The position of the slit is moved horizontally along the cross-section of the beam to select narrow frequency components.

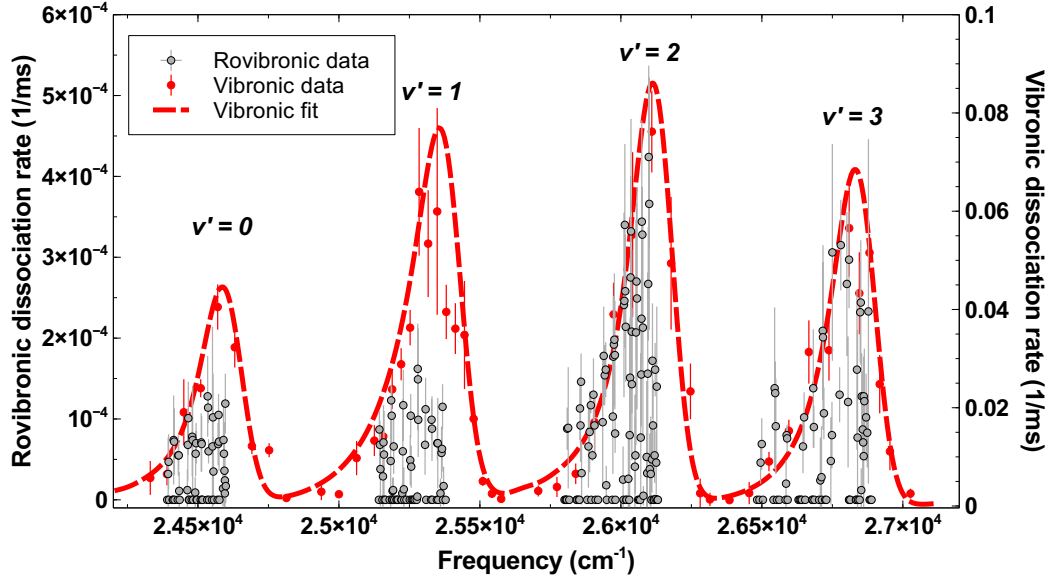


Figure 35: Rovibronic lines within the $v'=0, 1, 2, 3$ vibronic transitions shown with the vibronic spectrum of CaH^+ . The rovibronic spectrum matches well the envelope of the vibronic spectrum.

Our analysis shows good agreement on peak positions between theory and experiment. The molecular constants for the ground and first excited states are shown in table 4. Also, the deduced experimental rotational are a good match to theoretical values. We, however, observe large variations in distortion constants and an increase in rotational constant from $v'=3$ to $v'=4$. This reversed trend might be due to distortions in the potential energy curves of CaH^+ previously predicted in isoelectronic KH [106]. The discrepancy between our results and theory on distortion constants might also be a result of limited resolution or uncertainty in the frequency of the measured rovibronic lines.

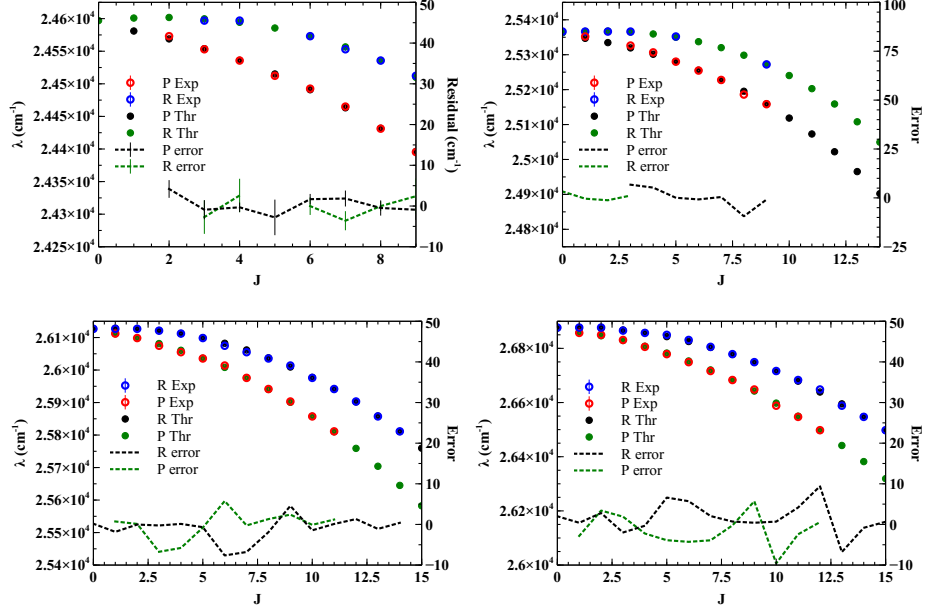


Figure 36: Assignment of rovibronic lines within the $v' = 0, 1, 2, 3$ vibronic transitions. The percent error is calculated as $error = \frac{|experiment - theory|}{experiment} \times 100$ and is small for all measured lines.

Table 4: Rotational and distortion constants for vibrational states in $1^1\Sigma$ and $2^1\Sigma$ electronic states. They are determined using a Nelder-Mead Minimization Algorithm [102] to the χ^2 value (difference between theoretical and experimental rovibronic peak positions) using a C++ library [103]. Large variations in deduced distortion constants are observed.

Electronic	Vibrational	B_v (theory)	B_v (experiment)	D_v (theory)	D_v (experiment)
$1^1\Sigma$	$v = 0$	4.71	4.65 ± 0.0012	0.00020	$0.0018 \pm 5.03 \times 10^{-6}$
	$v = 1$	3.05	3.31 ± 0.0033	0.00018	$0.0016 \pm 1.45 \times 10^{-8}$
$2^1\Sigma$	$v = 0$	2.94	3.23 ± 0.0041	0.00017	$0.0016 \pm 1.45 \times 10^{-8}$
	$v = 2$	2.88	2.76 ± 0.0026	0.00017	$0.00019 \pm 7.03 \times 10^{-7}$
	$v = 3$	2.80	2.79 ± 0.0022	0.00018	$0.00050 \pm 4.65 \times 10^{-8}$

8.2.4 Quantum heating rovibronic spectroscopy

The current rovibronic spectroscopy results on CaH^+ are a good starting point for high precision spectroscopy. The REMPD technique has a major downside of being destructive. Thus, every step of the measurement process requires reassociation to reform molecular ions which makes the experiment much slower. This drawback can be alleviated by doing non-destructive spectroscopy with a much smaller sample of ions.

Quantum heating spectroscopy, also called photon recoil spectroscopy, indirectly measures the strength of a transition in a sympathetically-cooled ion by detecting the induced heating on the refrigerant ion. The induced heating on the Coulomb crystal is maximized when the frequency of the absorbed photon is one FWHM blue-detuned with respect to the transition resonance frequency. For an optimal signal to noise ratio, the Coulomb crystal is cooled to the motional ground state as outlined in Chapter 5. We have observed that the breathing mode of the Ca^+-CaH^+ has a much lower heating rate, which would substantially reduce noise in our measurement.

The spectroscopy scheme would begin by sympathetically sideband cooling the breathing mode of the Coulomb crystal and measuring the temperature using the ratio of red to blue sidebands. A pulse-shaped frequency-doubled Ti-Sapphire beam would then excite the molecule for a few ms, and a 729 nm red sideband pulse (RSB) would excite the Ca^+ ion to the metastable $D_{5/2}$ state. The probability of shelving the logic ion reflects the

probability of exciting the molecular ion with the spectroscopy laser which can be measured by deshelling the ion with a 854 pulse and counting the number of 393 nm emitted photons. The change in the number of emitted photons as a function of spectroscopy laser frequency would yield the rovibronic peak, which would be adjusted by half its FWHM to get the real resonance frequency. The excitation frequency could be selected to match any of the rovibronic lines measured with REMPD, but it is more beneficial to start with strongest transitions.

One could worry about the dissociation of the molecular ion by the spectroscopy laser or the 397 nm laser used to cool the atomic ions during the experiment, but this problem can be addressed by using moderate laser powers for both lasers and short excitation times. Furthermore, the dissociation rate observed for rovibronic lines are slower than the proposed timescale for this experiment. Another problem is the observed asymmetry of the frequency profile of the pulse-shaped beam. Given that the frequency resolution is limited by the width of the laser is what limits the resolution, the measured peak would not be symmetric, and the adjustment to find the real resonance frequency could be erroneous. As a result, it is more beneficial to use a cw laser, which would also increase the resolution.

The sensitivity of this method heavily depends on the number of photons absorbed by the molecule. For most molecular ions, the lack of closed transitions does not permit fast absorption-emission cycles with few lasers. Consequently, the induced heating on the logic ion (atomic coolant) has to

come from a single photon absorption by the molecule because multiple photon absorption-emission cycles demand waiting times up to tens of seconds. These long time gaps would lead to a gain of hundreds of quanta in motional energy that would compromise the signal to noise ratio of the measurement. The probability of motional excitation on the logic ion after exciting the spectroscopy transition in the molecule can be approximated as [57]:

$$p_e \sim 1 - \exp(-N_a^2 \eta^2), \quad (38)$$

where N_a represents the number of absorbed photons, and η is the Lamb-Dicke parameter expressed in equation 20. For our sideband cooling experiments, typical values for η are on the order of 0.1 which correspond to a probability of 0.01 for motionally exciting the logic ion. This signal would be hardly detectable, and without rotational cooling, a more sensitive method such as quantum logic spectroscopy [51] or a similar approach using coherent motion state detection [56] would be needed.

8.2.5 Quantum heating using an optical dipole force

The estimated natural linewidth for the rovibronic transitions that we measured is around 3 MHz, and quantum logic spectroscopy is only applicable to transitions much narrower than that. This limitation is due to the fact that during quantum logic spectroscopy, excitation on the spectroscopy ion takes place on the resolved blue sideband. To get around this problem, a

recent technique used an optical dipole force from two off-resonant counter-propagating beams. This approach was used both on an atomic ion Al^+ [56] and most recently on a MgH^+ molecular ion [60]. It is based on Stark-shifted transitions that prevent photon scattering and thus avoid the relaxation of the ion into the wrong rovibrational state. The gradient of the Stark effect induces a force that depends on the detuning from the transition resonance.

Using a two-level electronic system of a molecular ion, the Stark shift resulting from the interaction between the molecule and the laser can be derived using second-order perturbation theory and is given by [141]:

$$\delta E = \frac{\mu_{ge}^2 E^2 \omega}{2(\omega^2 - \nu^2)}, \quad (39)$$

where E is the magnitude of the electric field of the laser, μ_{ge} represents the transition dipole moment, ω is the resonance frequency of the transition between the ground state $|g\rangle$ and the excited state $|e\rangle$, and ν is the frequency of the laser. The spatial derivative of the induced Stark effect generates a static force that can increase the motion of the ion. Coherent motional excitation can be achieved by using two counter-propagating beams of slightly different wavelengths ν_1 and ν_2 and wavevectors k_1 and k_2 . These two beams form a standing wave that travels along the z direction whose resulting electric field resembles [142]:

$$E_t = E \cos\left(\frac{1}{2}(\nu_1 + \nu_2)t\right) \cos\left(\frac{\Delta k}{2}z - \frac{1}{2}(\Delta\nu t)\right). \quad (40)$$

The term with difference in wavelength $\Delta\nu = \nu_1 - \nu_2$ creates an additional oscillation of the force. If $\Delta\nu$ is resonant with the motional frequency of the

ion coherent motional excitation can happen. The resulting oscillating force can be expressed as:

$$F = -\nabla(\delta E) \equiv -\nabla\left(\frac{\mu_{ge}^2 E^2 \omega}{(\omega^2 - \nu^2)} \cos^2\left(\frac{\Delta k}{2} z - \frac{\Delta \nu}{2} t\right)\right) \quad (41)$$

To perform non-destructive rovibronic state detection on CaH^+ using an optical dipole force, we can use a scheme similar to the procedure outlined in the previous section. One of the beams used to excite the spectroscopy ion can be frequency-controlled using an AOM. To reduce unwanted heating on the atomic ion, the $1^1\Sigma, v = 0 \rightarrow 2^1\Sigma, v = 4$ vibronic transition should be used for a detuning close to 50 THz from the atomic cooling transition. The rovibronic spectrum would correspond to the change in Rabi frequency as the detuning of the spectroscopy laser is changed. The Rabi frequency for each detuning frequency can be deduced by fitting equation 30 to the variation of sideband strength ratio as a function of interaction time between the Coulomb crystal and the optical dipole force.

8.2.6 Rotational cooling of CaH^+ ions

As previously mentioned, the implementation of quantum logic spectroscopy on molecular ions is hampered by the inability to control the rotational state of the ion especially after photon scattering processes. This barrier can be alleviated by the rotational cooling techniques using either rovibronic or rovibrational transitions in the ground electronic state.

One cooling scheme would need preliminary rovibrational spectroscopy in the ground electronic state. This can be achieved using a broadband source

within the wavelength range of $6.9\ \mu\text{m}$ to excite the molecules on the fundamental vibrational transitions. State detection would use a REMPD-based approach through 1+1 photon excitation from the first excited vibrational state. Upon measuring the first few rovibrational transitions, one of them would suffice for rotational state preparation of similar efficiency as previously shown in other molecules [66, 67].

The cooling process would start by exciting the molecular ions on the $v = 0, J = 2 \longrightarrow v = 1, J = 1$ transition and then dissociating the molecular ions from the $v = 0, J = 0$ state after a wait time of several seconds to allow relaxation. Figure 37 shows the rotational cooling scheme.

8.3 Spectroscopy on BH^+

8.3.1 Production of BH^+ molecular ions

Our attempt to produce BH^+ ions by reacting ablated boron ions with Hydrogen gas, a technique previously used to produce BH molecules [132], has not been successful. An alternative method is to react B^+ ions with H atoms. Hydrogen atoms would be produced by thermally dissociating molecular hydrogen in a hot tungsten capillary tube [143]. Such hydrogen atom sources are commercially available and compatible with our experimental setup. Although producing molecular ions in this manner would be fast and efficient it is a more costly method and makes the generation and trapping of pure samples of ions challenging. One way to get around this problem is to produce

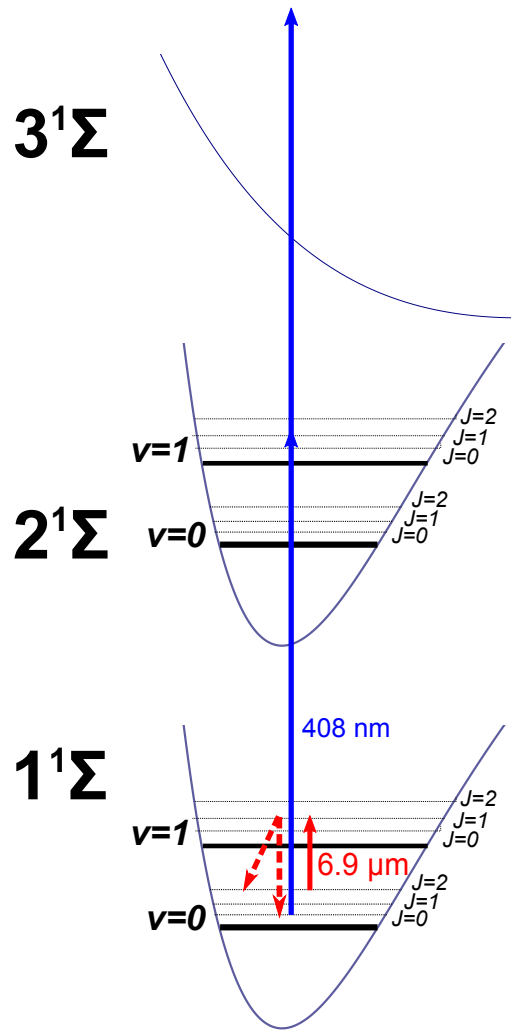


Figure 37: A diagram shows the simplified structure that will be used for rotational cooling (not to scale). The ions are excited on the $v = 0, J = 2 \rightarrow v = 1, J = 1$ transition using a 6.9 μm laser. The vibrational relaxation puts the ions either in the $v = 0, J = 2$ state or the $v = 0, J = 0$ state, but the $v = 0, J = 2$ gets ultimately depleted because of continuous excitation. Its depletion instigates rotational decay from higher rotational states, and the repeated process puts nearly all the population in the ground rovibrational state. The two 408 nm detection photons are used to measure the population in the $v = 0, J = 0$ state before and after rotational cooling. Bluer vibronic transitions can also be used for detection.

BH neutrals and photoionize them using a 2+1' resonance enhanced multi-photon ionization (REMPI) scheme. The first two 433 nm photons can be generated from a diode laser or a frequency-doubled Ti-Sapphire laser and the third photon would come from a 300 nm UV diode lamp. There are no strict frequency requirements on the third photon as long as it is shorter than 310 nm.

To produce BH neutral molecules various methods can be employed. First, one can ablate a piece of NaBH_4 to generate the neutral molecules. This approach is promising since a similar experiment has generated AlH molecules by ablating AlH_4 [137]. Another technique that has also been used to make AlH molecules [144] can be applied to the production of BH neutral molecules. This technique uses ablation of the elemental target (in this case B) while high pressure Hydrogen gas is being pulsed on the target. Such a system demands an additional chamber separated by a skimmer to isolate the high pressure gas from the main chamber. In addition, differential pumping would also avoid pressure compromises in the main vacuum vessel.

In case none of the above methods succeeds, we can resort to a more popular method which produces the neutral molecules via photolysis of diborane gas using a 193 nm beam from an excimer. This way of producing BH molecules has been replicated in multiple experiments [131, 145] but is not preferable due to the safety hazards diborane gas poses [146].

8.3.2 Laser induced fluorescence

As previously mentioned BH^+ fits the profile of a few other molecules that have been directly laser-cooled [63, 64, 147]. The vibronic structure that all these molecules possess allows for closed rovibronic transitions. This property exhibited mostly by atomic particles is fundamental to a high signal to noise ratio in fluorescence detection. A molecule with closed transitions will scatter many detectable photons before decaying to a dark rovibrational state.

For BH^+ , in addition to the main pump 379 nm laser one can expect two repumper lasers to fully close the $X^2\Sigma, v = 0, K = 1 \rightarrow A^2\Pi, v = 0, K = 1$ rovibronic transitions. The first repumper (417 nm) would excite from the $X^2\Sigma, v = 1, K = 1$ state, and the second would be a 4 μm laser to address parity flips in the $X^2\Sigma, v = 0$ state. Two EOMs can cover spin states within the first two vibrational states in the ground electronic state. We predict the spin splittings to be 0.81(13) GHz and 0.72(13) GHz for $v = 0$ and $v = 1$ respectively. Alternatively, two frequency-doubled Ti:Sapphire beams with a frequency bandwidth of a few THz can replace the EOMs.

The branching to higher vibrational states is very small, and they may not need to be repumped. The main cooling beam as well as the repumper laser can be supplied using ECDLs that have already been setup. The IR beam will be generated by a an optical parametric oscillator (OPO) system (Aculight model 2400) pumped by a fiber laser at 1064 nm (NKT Photonics Koheras AdjustiK Y10) and amplified using an optical parametric amplifier

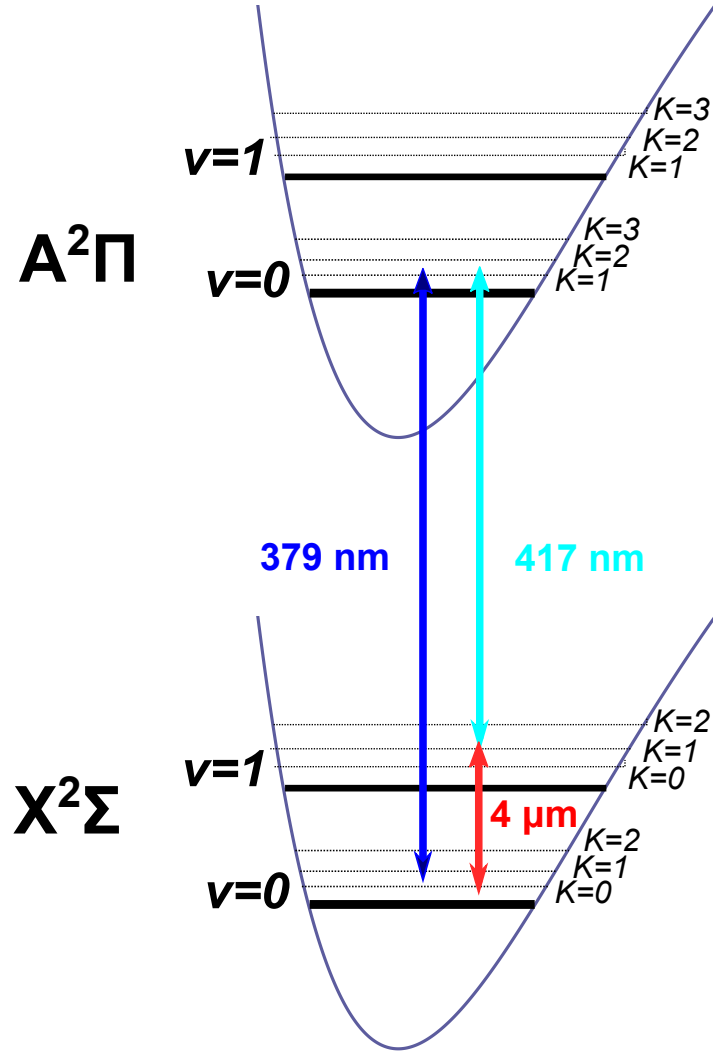


Figure 38: A scheme for the laser induced fluorescence of BH^+ ions is shown. The main cooling laser is the 379 nm which would continuously excite the ions on the $X^2\Sigma, v = 0, K = 1 \rightarrow A^2\Pi, v = 0, K = 1$. The initial $K = 1$ rotational state is judiciously chosen to avoid rotational branching. The 417 nm laser repumps the $v = 1$ state and the $4 \mu\text{m}$ laser repopulates the $K = 1$ in case there is decay to any of the even parity states from $v = 1$. The $4 \mu\text{m}$ laser frequency will also need the same modulation as the 379 nm . This scheme would also result in rotational cooling.

(OPA) (IPG Photonics YAR 10K-1064-LP-SF).

With the above laser configuration, we expect $10^4/\text{s}$ to be scattered per ion [62]. Given the photon collection efficiency of 0.1 % for our current setup, the number of photons detected per ion will be around 10. With careful alignment of the 379 nm beam through the trap to avoid background scatter, this number would be barely above the noise level. We can enhance the fluorescence signal by using a large crystal of molecular ions sympathetically cooled by Ca^+ ions. A crystal or cloud containing 100 BH^+ ions would be easily detectable on the PMT and visible on the CCD camera. The signal can be enhanced by two orders of magnitude by using two frequency-doubled femtosecond lasers for both the 379 nm and 417 nm beams.

Without initial rotational state preparation in $K = 1$, the number of photons scattered would be reduced by a factor of six considering the population of the state as shown in figure 39. In case femtosecond lasers are used, we can achieve over 90 % of the population in $K = 0$ in a few ms by exciting from the $K = 2$ state [68]. A two-photon excitation using the IR laser and the 417 nm followed by relaxation from the A state would subsequently shift nearly all the population into the $K = 1$ state.

The detection of fluorescence from BH^+ molecules is essential for the realization of non-destructive molecular spectroscopy. Diagonal Franck-Condon factors of BH^+ molecules make them promising candidates for photon recoil spectroscopy experiments. They are expected to scatter around 70 photons before they spontaneously decay to a higher vibrational state. With this

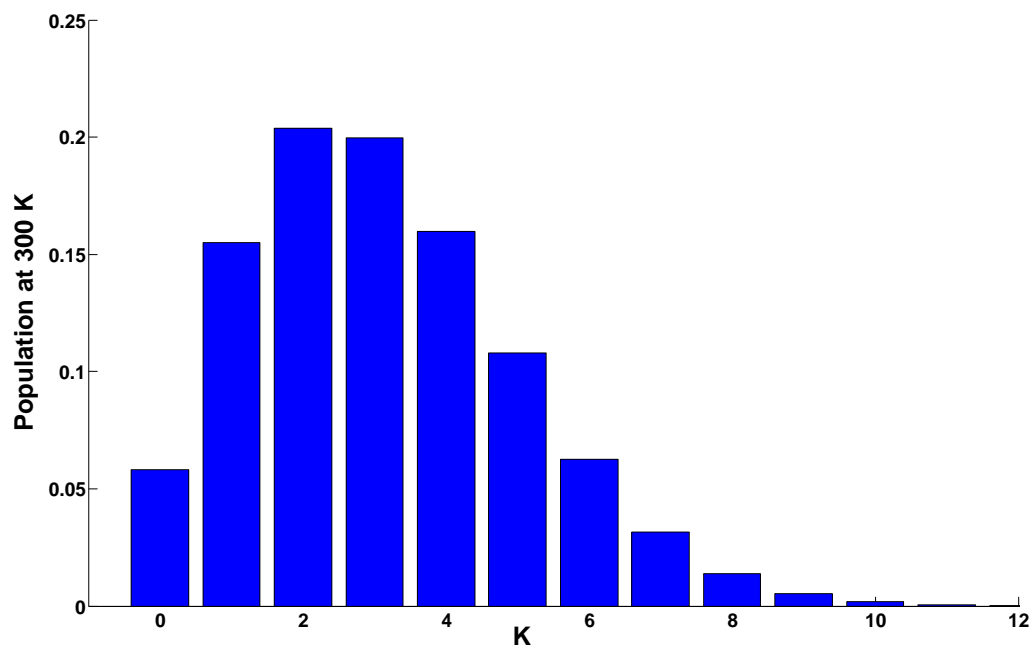


Figure 39: The rotational population distribution at 300 K in the $X^2\Sigma, v = 0$ state is shown. The quantum number K is the total angular momentum not including the spin of the electron. The population for every state is calculated using a Boltzmann distribution function. The large rotational constant (B) of the BH^+ molecule pushes the population distribution to the low-lying states.

many photons scattered, it becomes possible to detect motional excitation on the logic ion upon probing the molecular ion with the spectroscopy laser.

This thesis has focused on various projects that will lead to the realization of quantum logic spectroscopy of molecular ions. Achieving the kind of precision offered by QLS measurements will certainly impact various areas of science in chemistry and physics. Apart from providing some answers to various questions of cosmology, high precision laser-cooled molecular ions will also enable the implementation of other sophisticated techniques such as blackbody thermometry in atomic ion optical clocks [148]. In addition, the localization and isolation of laser cooled-molecular ions could allow the realization of structural determination experiments using few-tightly-focused femtosecond X-ray lasers thus reducing the interaction time and avoiding any modification of sample molecules [149]. These experiments would improve the structural study of biological molecules. In summary, the applications of laser-cooled molecular ions are set to impact many areas of science in the future.

APPENDIX A

ELECTRONIC AND VIBRATIONAL LIFETIMES OF BH^+

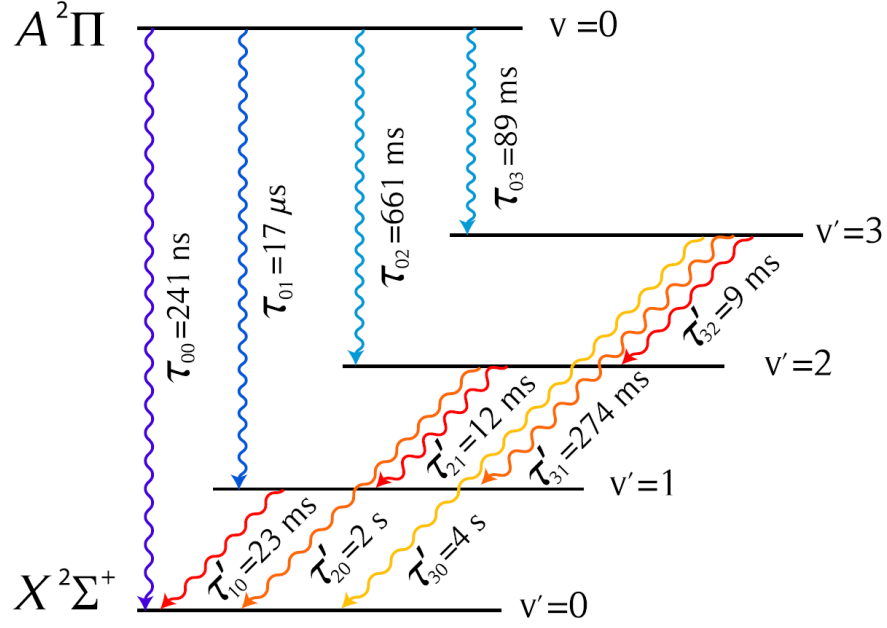
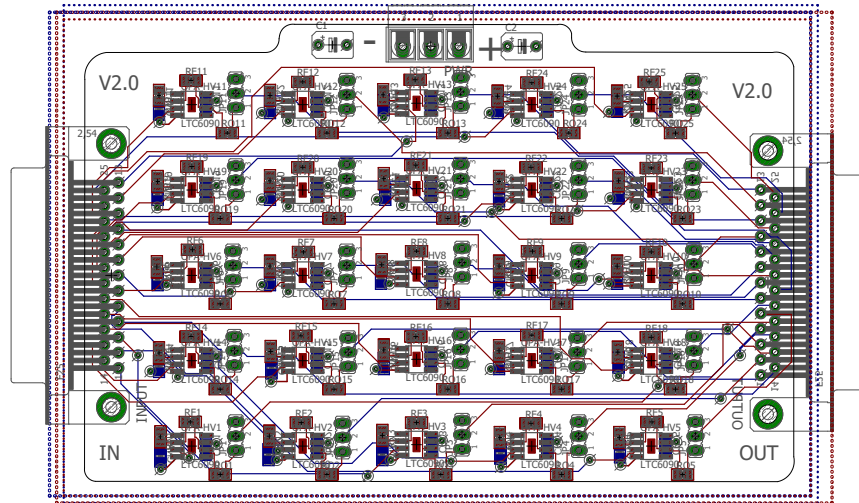


Figure 40: The vibrational and electronic transition lifetimes of the BH⁺ molecule are shown. The lifetimes of the X-A vibronic transitions are denoted by τ and the vibrational lifetimes in the X state by τ' [62].

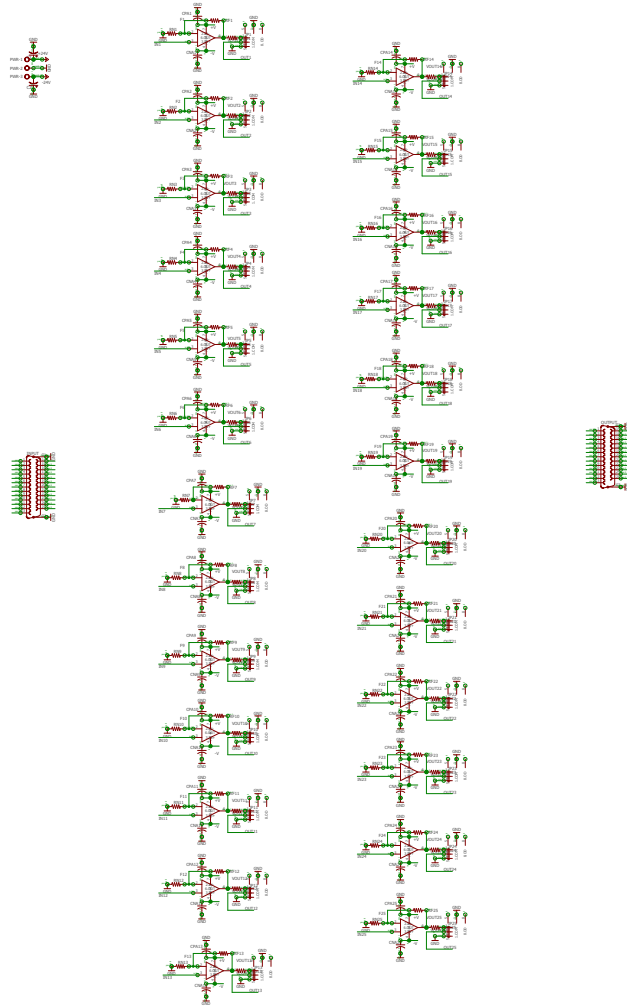
APPENDIX B

CIRCUIT BOARDS DIAGRAMS



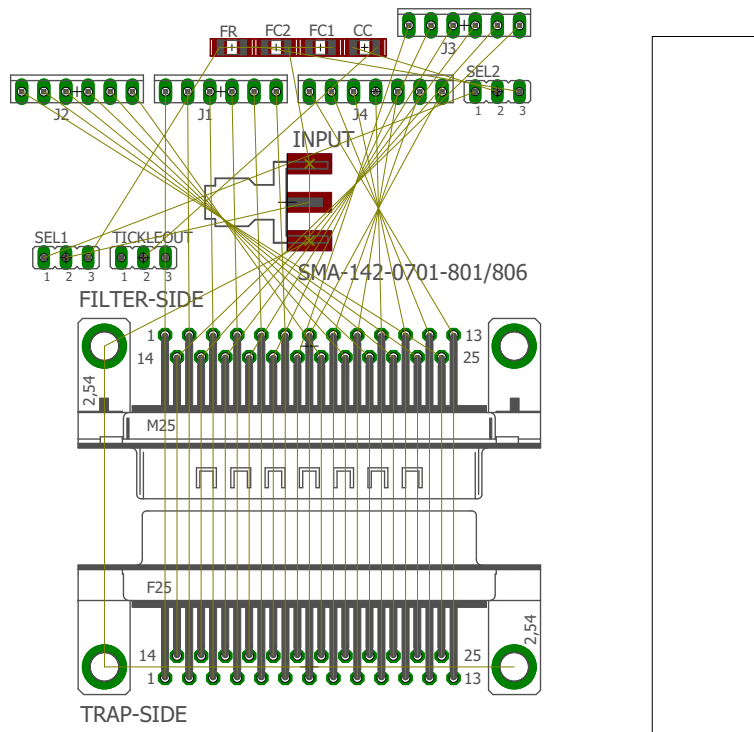
8/10/2016 11:15 AM f=1.60 C:\Users\brownlab\Pictures\sch.brd

Figure 41: The amplifier board used for DC voltages on the improved Goeders setup is shown.



8/10/2016 11:36 AM f=0.50 C:\Users\brownlab\Pictures\sch.sch (Sheet: 1/1)

Figure 42: The schematic of the amplifier board used for DC voltages on the improved Goeders setup is shown.



8/10/2016 12:18 PM f=2.30 C:\Users\brownlab\AppData\Local\Temp\Rar\$Dla0.413\TickleInjector.brd

Figure 43: The board used for injecting the RF voltage for motional resonance experiments is shown.



113

Bibliography

- [1] G. Herzberg, Ann. Rev. Phys. Chem. **36**, 1 (1985).
- [2] G. Herzberg, Chem. Soc. Rev. **25**, 455 (1971).
- [3] R. Saykally and R. C. Woods, Ann. Rev. Phys. Chem. **32**, 403 (1981).
- [4] W. H. Wing, G. A. Ruff, W. E. Lamb, and J. J. Spezeski, Phys. Rev. Lett. **36**, 1488 (1976).
- [5] G. Herzberg, Chem. Phys. J. **70**, 4806 (1979).
- [6] L. Andrews, Ann. Rev. Phys. Chem. **30**, 79 (1979).
- [7] J. M. Doyle, B. Fridrich, J. Kim, and D. Patterson, Phys. Rev. A **52**, R2515 (1995).
- [8] R. Krems, F. Bretonisch, and W. C. Stwalley, *Cold Molecules: Theory, Experiment, Applications* (CRC Press, 2009).
- [9] F. M. Penning, Physica **3**, 873 (1936).
- [10] W. Paul and H. Steinwedel, Z. Naturforsch **A3**, 448 (1953).
- [11] C. B. Richardson, K. B. Jefferts, and H. G. Dehmelt, Phys. Rev. **165**, 80 (1968).
- [12] F. J. Grieman, B. H. Mahan, and A. O’Keefe, J. Chem. Phys **72**, 4246 (1980).
- [13] F. J. Grieman, B. H. Mahan, A. O’Keefe, and J. S. Winn, Discuss. Faraday Soc. **71**, 191 (1981).
- [14] B. H. Mahan and A. O’Keefe, J. Chem. Phys **74**, 5606 (1981).
- [15] W. Neuhauser, M. Hohenstatt, and P. E. Toschek, Appl. Phys. **17**, 123 (1978).
- [16] D. Wineland, R. E. Drullinger, and F. L. Walls, Phys. Rev. Lett. **40**, 1639 (1978).

- [17] W. Neuhauser, M. Hohenstatt, P. E. Toschek, and H. Dehmelt, Phys. Rev. A **22**, 1137 (1980).
- [18] F. Diedrich, J. C. Bergquist, W. M. Itano, and D. J. Wineland, Phys. Rev. Lett. **64**, 403 (1989).
- [19] D. J. Wineland, W. I. Itano, and J. C. Bergquist, Opt. Lett. **12**, 389 (1987).
- [20] A. A. Madej and J. D. Sankey, Opt. Lett. **11**, 634 (1990).
- [21] S. Urabe, H. Imajo, K. Hayasaka, and M. Watanabe, J. Mod. Opt. **39**, 417 (1992).
- [22] H. A. Klein, A. S. Bell, G. P. Barwood, and P. Gill, Appl. Phys. B **50**, 13 (1990).
- [23] D. J. Larson, J. C. Bergquist, J. J. Bollinger, W. M. Itano, and D. J. Wineland, Phys. Rev. Lett. **57**, 70 (1986).
- [24] K. Bowe, L. Hornekær, C. Brodersen, M. Drewsen, and J. S. Hangst, Phys. Rev. Lett. **82**, 76 (1999).
- [25] Y. Kai, K. Toyoda, M. Watanabe, and S. Urabe, J. Appl. Phys. **40**, 5136 (2001).
- [26] M. Drewsen, Physica B **460**, 105 (2015).
- [27] T. Baba and I. Waki, J. Appl. Phys. **35**, L1134 (1996).
- [28] T. Baba and I. Waki, J. Chem. Phys. **116**, 1858 (2002).
- [29] K. Mølhave and M. Drewsen, Phys. Rev. A **62**, 011401 (2000).
- [30] M. Drewsen, A. Mortensen, R. Martinussen, P. Sta anum, and J. L. Sørensen, Phys. Rev. Lett. **93**, 243201 (2004).
- [31] E. K. Campbell, M. Holz, D. Gerlich, and J. P. Maier, Nature **523**, 322 (2015).
- [32] O. Asvany, M. K. Yamada, S. Bruken, A. Potapov, and S. Schlemmer, Science **347**, 1346 (2015).

- [33] B. Roth, P. Blythe, H. Wenz, H. Daerr, and S. Schiller, *Phys. Rev. A* **73**, 04271 (2006).
- [34] N. Kimura, K. Okada, T. Takayanagi, M. Wada, S. Ohtani, and H. A. Schuessler, *Phys. Rev. A* **83**, 033422 (2011).
- [35] L. Hornekær, Ph.D. thesis, University of Aarhus (2000).
- [36] M. Kajita, M. Abe, M. Hada, and Y. Moriwaki, *J. Phys. B: At. Mol. Opt. Phys.* **44**, 025402 (2011).
- [37] U. Bressel, A. Borodin, J. Shen, M. Hansen, I. Ernsting, and S. Schiller, *Phys. Rev. Lett.* **108**, 183003 (2012).
- [38] U. Flöhlich, B. Roth, P. Antonini, C. L. Ammerzahl, A. Wicht, and S. Schiller, *Lect. Notes Phys.* **648**, 297 (2004).
- [39] B. Roth, J. Koelemeij, S. Schiller, L. Hilico, and J. P. Karr, *Lect. Notes Phys.* **745**, 205 (2008).
- [40] B. Roth, J. C. J. Koelemeij, P. Blythe, H. Daerr, and S. Schiller, *Phys. Rev. A* **74**, 040501(R) (2006).
- [41] P. F. Sta anum, K. Højbjerg, P. S. Skyt, A. K. Hansen, and M. Drewsen, *N. J. Phys.* **11**, 055026 (2009).
- [42] N. B. Khanyile, G. Shu, and K. R. Brown, *Nature Commun.* **6**, 7825 (2015).
- [43] H. Loh, K. C. Cossel, M. C. Grau, K.-K. Ni, E. R. Meyer, J. L. Bohn, J. Ye, and E. A. Cornell, *Science* **342**, 1220 (2013).
- [44] A. E. Leanhardt, J. L. Bohn, H. Loh, P. Maletinsky, E. R. Meyer, L. C. Sinclair, R. P. Stutz, and E. A. Cornell, *J. Mol. Spec.* **270**, 1 (2011).
- [45] E. R. Meyer and J. L. Bohn, *Phys. Rev. A* **78**, 010502 (2008).
- [46] A. N. Petrov, N. S. Mosyagin, T. A. Isaev, and A. V. Titov, *Phys. Rev. A* **76**, 030501 (2007).
- [47] V. V. Flambaum, D. DeMille, and M. G. Kozlov, *Phys. Rev. Lett.* **113**, 103003 (2014).

- [48] D. E. Morrissey and M. J. Ramsey-Musolf, N. J. Phys. **14**, 125003 (2012).
- [49] M. D. Barrett, B. DeMarco, T. Schaetz, V. Meyer, D. Leibfried, J. Britton, J. Chiaverini, W. M. Itano, B. Jelenkovic, J. D. Jost, et al., Phys. Rev. A **68** (2003).
- [50] J. D. Jost, J. P. Home, J. M. Amini, D. Hanneke, R. Ozeri, C. Langer, J. J. Bollinger, D. Leibfried, and D. J. Wineland, Nature **459**, 683 (2009).
- [51] P. O. Schmidt, T. Rosenband, C. Langer, W. M. Itano, J. C. Bergquist, and D. J. Wineland, Science **309**, 749 (2005).
- [52] T. Rosenband, D. B. Hume, P. O. Schmidt, C. W. Chou, A. Brusch, L. Lorini, W. H. Oskay, R. E. Drullinger, T. M. Fortier, J. E. Stalnaker, et al., Science **319**, 1808 (2008).
- [53] C. W. Chou, D. B. Hume, J. C. J. Koelemeij, D. J. Wineland, and T. Rosenband, Phys. Rev. Lett. **104**, 070802 (2010).
- [54] C. R. Clark, J. E. Goeters, Y. K. Dodia, R. C. Viteri, and K. R. Brown, Phys. Rev. A **81**, 043428 (2010).
- [55] Y.-W. Lin, S. Williams, and B. C. Odom, Phys. Rev. A **87**, 011402 (2013).
- [56] D. B. Hume, C. W. Chou, D. R. Leibbrandt, M. J. Thorpe, D. J. Wineland, and T. Rosenband, Phys. Rev. Lett. **107**, 243902 (2011).
- [57] Y. Wan, F. Gebert, J. B. Wäbbena, N. Scharnhorst, S. Amairi, I. D. Leroux, B. Hemmerling, N. Lärch, K. Hammerer, and P. O. Schmidt, Nat. Commun. **5**, 3096 (2014).
- [58] C. F. Roos, Ph.D. thesis, University of Innsbruck (2000).
- [59] Y. Wan, F. Wolf, F. Gebert, and P. O. Schmidt, Phys. Rev. A **91**, 043425 (2015).
- [60] F. Wolf, Y. Wan, J. C. Heip, F. Gebert, C. Shi, and P. O. Schmidt, Nature **530**, 457 (2016).

- [61] J. H. V. Nguyen and B. Odom, Phys. Rev. A **83**, 053404 (2011).
- [62] J. H. V. Nguyen, C. R. Viteri, E. G. Hohenstein, C. D. Sherrill, K. R. Brown, and B. Odom, N. J. Phys. **13**, 063023 (2011).
- [63] E. S. Shuman, J. F. Barry, and D. DeMille, Nature **467**, 820 (2010).
- [64] M. T. Hummon, M. Yeo, B. K. Stuhl, A. L. Collopy, Y. Xia, and J. Ye, Phys. Rev. Lett. **110**, 143001 (2013).
- [65] X. Tong, A. H. Winney, and S. Willitsch, Phys. Rev. Lett. **105**, 143001 (2010).
- [66] P. F. Sta anum, K. Højbjørre, P. S. Skyt, A. K. Hansen, and M. Drewsen, Nat. Phys. **6**, 271 (2010).
- [67] T. Schneider, B. Roth, H. Duncker, I. Ernsting, and S. Schiller, Nat. Phys. **6**, 275 (2010).
- [68] C. Lien, C. Seck, Y. Lin, J. Nguyen, D. A. Tabor, and B. C. Odom, Nat. Commun. **5**, 4783 (2014).
- [69] A. K. Hansen, O. O. Versolato, L. Klosowski, A. Gingell, M. Schwarz, A. Windberger, J. Ullrich, L. Crespo, and M. Drewsen, Nature **508**, 76 (2014).
- [70] W. G. Rellergert, S. T. Sullivan, S. J. Schowalter, S. Kotochigova, K. Chen, and E. R. Hudson, Nature **495**, 490 (2013).
- [71] W. Paul, Rev. Mod. Phys. **62**, 531 (1990).
- [72] T. Jones, *Mathieu's equations and the ideal rf trap*, URL <http://www.physics.drexel.edu/~tim/open/mat/mat.pdf>.
- [73] D. Leibfried, R. Blatt, C. Monroe, and D. Wineland, Rev. Mod. Phys. **75**, 282 (2003).
- [74] H. J. Metcalf and P. v. d. Straten, *Laser Cooling and Trapping* (Springer-Verlag New York, Inc., 1999).
- [75] M. O. Scully and S. Zubairy, *Quantum optics* (Cambridge University Press, 1997).

- [76] M. Guggemos, D. Heinrich, O. Herrera-Sancho, R. Blatt, and C. Roos, *New J. Phys.* **17**, 103001 (2015).
- [77] L. R. Churchill, Ph.D. thesis, Georgia Institute of Technology (2010).
- [78] J. E. Goeders, C. R. Clark, G. Vittorini, K. Wright, R. C. Viteri, and K. R. Brown, *J. Phys. Chem. A* **117**, 9725 (2013).
- [79] N. B. Khanyile, Ph.D. thesis, Georgia Institute of Technology (2015).
- [80] J. E. Goeders, Ph.D. thesis, Georgia Institute of Technology (2013).
- [81] D. J. Berkeland, J. C. Miller, W. M. Itano, and D. J. Wineland, *J. Appl. Phys.* **83**, 5025 (1998).
- [82] H. C. Nägerl, C. Roos, D. Leibfried, H. Rohde, G. Thalhammer, J. Eschner, F. Schmidt-Kaler, and R. Blatt, *Phys. Rev. A* **61**, 023405 (2000).
- [83] G. Shu, G. Vittorini, A. Buikema, C. S. Nichols, C. Volin, D. Stick, and K. R. Brown, *Phys. Rev. A* **89**, 062308 (2014).
- [84] C. Roos, T. Zeiger, H. Rohde, H. C. Nägerl, J. Eschner, D. Leibfried, F. Schmidt-Kaler, and R. Blatt, *Phys. Rev. Lett.* **83**, 4713 (1999).
- [85] J. B. Wübbena, S. Amairi, O. Mandel, and P. O. Schmidt, *Phys. Rev. A* **85**, 043412 (2012).
- [86] S. Schiller, D. Bakalov, A. K. Bekbaev, and V. I. Korobov, *Phys. Rev. A* **89**, 052521 (2014).
- [87] M. Germann, X. Tong, and S. Willitsch, *Nat. Phys.* **10**, 820 (2014).
- [88] M. Kajita, G. Gopakumar, M. Abe, M. Hada, and M. Keller, *Phys. Rev. A* **89**, 032509 (2014).
- [89] A. Eagle, *Astrophys. J.* **30**, 231 (1909).
- [90] A. A. Mills, B. M. Siller, M. W. Porambo, M. Perera, H. Kreckel, and B. J. McCall, *J. Chem. Phys.* **135**, 224201 (2011).
- [91] B. Roth, H. Wenz, H. Daerr, and S. Schiller, *Phys. Rev. A* **73**, 042712 (2006).

- [92] A. K. Hansen, M. A. Sørensen, P. F. Staantum, and M. Drewsen, *Angew. Chem. Int. Ed.* **51**, 7960 (2012).
- [93] M. Kajita and M. Abe, *J. Phys. B: At. Mol. Opt. Phys.* **45**, 185401 (2012).
- [94] M. Abe, M. Kajita, M. Hada, and Y. Moriwaki, *J. Phys. B: At. Mol. Opt. Phys.* **43**, 245102 (2010).
- [95] M. Aymar and O. Dulieu, *J. Phys. B: At. Mol. Opt. Phys.* **45**, 215103 (2012).
- [96] M. Abe, Y. Moriwaki, M. Hada, and M. Kajita, *Chem. Phys. Lett.* **521**, 31 (2011).
- [97] H. Habli, H. Ghalla, B. Oujia, and F. Gadéa, *Eur. Phys. J. D* **64**, 5 (2011).
- [98] K. Matsubara, K. Hayasaka, Y. Li, Y. Ito, S. Nagano, M. Kajita, and M. Hosokawa, *App. Phys. Exp.* **1**, 067011 (2008).
- [99] K. Mori, T. Yusuke, M. Obara, and K. Midorikawa, *J. Appl. Phys.* **83**, 2915 (1998).
- [100] V. Krylov, A. Rebane, A. G. Kalintsev, H. Schwöerer, and U. P. Wild, *Opt. Lett.* **20**, 198 (1995).
- [101] R. J. L. Roy, University of Waterloo Chemical Physics Research Report **CP-663** (2014).
- [102] J. Nelder and R. Mead, *Comput. J.* **7**, 308 (1965).
- [103] R. O'Neill, *J. Appl. Stat.* **20**, 338 (1971).
- [104] I. R. Bartky, *J. Mol. Spec.* **20**, 299 (1966).
- [105] A. Pardo, J. J. Camacho, J. M. L. Potayo, and E. Martín, *Chem. Phys.* **117**, 149 (1987).
- [106] W. C. Stwalley, W. T. Zemke, and S. C. Yang, *J. Phys. Chem. Ref. Data* **20**, 153 (1991).

- [107] C. Carlsund-Levin, N. Elander, A. Nunez, and A. Scrinzi, *Physica Scripta* **65**, 306 (2002).
- [108] R. Rugango, J. E. Goeders, T. H. Dixon, J. M. Gray, N. Khanyile, G. Shu, R. J. Clark, and K. R. Brown, *New. J. Phys.* **17**, 035009 (2015).
- [109] O. O. Versolato, M. Schwarz, A. K. Hansen, A. D. Gingell, A. Windberger, L. Klosowski, J. Ullrich, F. Jensen, L. Crespo, and M. Drewsen, *Phys. Rev. Lett.* **111**, 053002 (2013).
- [110] A. D. Ludlow, M. M. Boyd, J. Ye, E. Peik, and P. Schmidt, *Rev. Mod. Phys.* **87**, 637 (2015).
- [111] M. S. Safronova, M. G. Kozlov, and C. W. Clark, *IEEE Trans. Ultrason., Ferroelect., Freq. Control* **59**, 439 (2012).
- [112] A. Müller, S. Schippers, R. A. Phaneuf, A. L. D. Kilcoyne, H. Bräuning, A. S. Schlachter, M. Lu, and B. M. McLaughlin, *J. Phys. B: At. Mol. Opt. Phys.* **43**, 225201 (2010).
- [113] T. Aoyamal, M. Fukudal, Y. Wall, Nara, S. Umisedo, N. Hamamoto, M. Hinds, Tanjo, and T. Nagayama, in *Proc. Int. Workshop Junction Technol.* (2005), pp. 27–30.
- [114] S. Mukherjee and P. Thilagar, *Chem. Commun* **52**, 1070 (2016).
- [115] L. Hanley and S. L. Anderson, *J. Phys. Chem* **91**, 5161 (1987).
- [116] M. B. Sowa-Resat, J. Smolanoff, A. Lapicki, and S. L. Anderson, *J. Chem. Phys.* **106**, 9511 (1997).
- [117] S. A. Ruatta, L. Hanley, and S. L. Anderson, *J. Chem. Phys.* **91**, 226 (1989).
- [118] K. Zimmermann, M. V. Okhapkin, A. Herrera-Sancho, and E. Peik, *Appl. Phys. B* **107**, 883889 (2012).
- [119] T. Baba and I. Waki, *Phys. Rev. Lett.* **89**, 4592 (2001).
- [120] P. Blythe, B. Roth, U. Fröhlich, H. Wenz, and S. Schiller, *Phys. Rev. Lett.* **95**, 183002 (2005).

- [121] V. L. Ryjkov, X. Zhao, and H. A. Schuessler, Phys. Rev. A **74**, 023401 (2006).
- [122] K. Højbjerg, D. Offenber, C. Z. Bisgaard, H. Stapelfeldt, P. F. Staantum, A. Mortensen, and M. Drewsen, Phys. Rev. A **77**, 030702 (2008).
- [123] B. Roth, Blythe, and S. Schiller, Phys. Rev. A **75**, 023402 (2007).
- [124] K. Pyka, N. Herschbach, J. Keller, and T. E. Mehlstäubler, Appl. Phys. B **114**, 231 (2014).
- [125] J. Nichols, M. Gutowski, S. J. Cole, and J. Simons, J.Phys.Chem. **96**, 644 (1992).
- [126] V. Dryza, B. L. J. Poad, and E. J. Bieske, J.Phys.Chem. **130**, 12986 (2008).
- [127] P. P. Pronko, P. A. VanRompay, Z. Zhang, and J. A. Nees, Phys. Rev. Lett. **83**, 2596 (1999).
- [128] M. Joseph and P. Manoravi, Appl. Phys. A **76**, 153156 (2003).
- [129] D. R. Ride, ed., *CRC Handbook of Chemistry and Physics* (CRC Press, Inc., 1992-1993).
- [130] C. Ottinger and J. Reichmuth, J. Chem. Phys. **74**, 928 (1981).
- [131] R. C. Viteri, A. T. Gilkison, and E. R. Grant, J. Chem. Phys. **136**, 214312 (2012).
- [132] T. J. Tague and L. Andrews, J. Am. Chem. Soc. **116**, 4970 (1994).
- [133] S. Amoruso, R. Bruzzese, N. Spinelli, and R. Velotta, J. Phys. B: At. Mol. Opt. Phys. **32**, R131 (1999).
- [134] C. Yang and Z. Zhu, J. Mol. Struct. **571**, 225 (2001).
- [135] C. Yang, Z. Zhu, R. Wang, and X. Liu, J. Mol. Struct. **548**, 47 (2001).
- [136] S. J. Schowalter, K. Chen, W. G. Rellergert, S. T. Sullivan, and E. R. Hudson, Rev. Sci. Instrum. **83**, 043103 (2012).

- [137] I. Labazan, N. Krstulović, and S. Milošović, Chem. Phys. Lett. **428**, 13 (2006).
- [138] T. Oksenhendler and N. Forget, *Pulse-Shaping Techniques Theory and Experimental Implementations for Femtosecond Pulses* (2010).
- [139] A. M. Weiner, J. P. Heritage, and E. M. Kirschner, Opt. Soc. Am. B **5**, 63 (1988).
- [140] A. M. Weiner, Rev. Sci. Instrum. **71**, 1929 (2000).
- [141] N. B. Delone and V. P. Krainov, Physics-Uspekhi **42**, 669 (1999).
- [142] D. J. Wineland, C. Monroe, W. M. Itano, D. Leibfried, B. E. King, and D. M. Meekhof, J. Res. Natl. Inst. Stand. Technol. **103**, 259 (1998).
- [143] K. G. Tschersich, J. P. Fleischhauer, and H. Schuler, J. Appl. Phys. **104**, 034908 (2008).
- [144] M. G. Kokish, M. R. Dietrich, and B. C. Odom, J. Phys. B: At. Mol. Opt. Phys. **49**, 035301 (2016).
- [145] R. J. Hendricks, D. A. Holland, S. Truppe, B. E. Sauer, and M. R. Tarbut, arXiv:1404.6174v2 [physics.atom-ph] (2014).
- [146] C. for Disease Control and Prevention, *Diborane*, URL <http://www.cdc.gov/niosh/ipcsneng/neng0432.html>.
- [147] V. Zhelyazkova, A. Cournol, T. E. Wall, A. Matsushima, J. J. Hudson, E. A. Hinds, M. R. Tarbutt, and B. E. Sauer, Phys. Rev. A **89**, 053416 (2014).
- [148] J. C. J. Koelemeij, B. Roth, and S. Schiller, Phys. Rev. A **76**, 023413 (2007).
- [149] S. Kahra, G. L. Leschhorn, M. Kowalewski, A. Schiffrin, E. Bothschafter, W. Fusz, R. de Vivie-Riedle, R. Ernstorfer, F. Krausz, R. Kienberger, et al., Nat. Phys. **8**, 238 (2012).

Bibliography

- [1] G. Herzberg, Ann. Rev. Phys. Chem. **36**, 1 (1985).
- [2] G. Herzberg, Chem. Soc. Rev. **25**, 455 (1971).
- [3] R. Saykally and R. C. Woods, Ann. Rev. Phys. Chem. **32**, 403 (1981).
- [4] W. H. Wing, G. A. Ruff, W. E. Lamb, and J. J. Spezeski, Phys. Rev. Lett. **36**, 1488 (1976).
- [5] G. Herzberg, Chem. Phys. J. **70**, 4806 (1979).
- [6] L. Andrews, Ann. Rev. Phys. Chem. **30**, 79 (1979).
- [7] J. M. Doyle, B. Fridrich, J. Kim, and D. Patterson, Phys. Rev. A **52**, R2515 (1995).
- [8] R. Krems, F. Bretonisch, and W. C. Stwalley, *Cold Molecules: Theory, Experiment, Applications* (CRC Press, 2009).
- [9] F. M. Penning, Physica **3**, 873 (1936).
- [10] W. Paul and H. Steinwedel, Z. Naturforsch **A3**, 448 (1953).
- [11] C. B. Richardson, K. B. Jefferts, and H. G. Dehmelt, Phys. Rev. **165**, 80 (1968).
- [12] F. J. Grieman, B. H. Mahan, and A. O’Keefe, J. Chem. Phys **72**, 4246 (1980).
- [13] F. J. Grieman, B. H. Mahan, A. O’Keefe, and J. S. Winn, Discuss. Faraday Soc. **71**, 191 (1981).
- [14] B. H. Mahan and A. O’Keefe, J. Chem. Phys **74**, 5606 (1981).
- [15] W. Neuhauser, M. Hohenstatt, and P. E. Toschek, Appl. Phys. **17**, 123 (1978).
- [16] D. Wineland, R. E. Drullinger, and F. L. Walls, Phys. Rev. Lett. **40**, 1639 (1978).

- [17] W. Neuhauser, M. Hohenstatt, P. E. Toschek, and H. Dehmelt, Phys. Rev. A **22**, 1137 (1980).
- [18] F. Diedrich, J. C. Bergquist, W. M. Itano, and D. J. Wineland, Phys. Rev. Lett. **64**, 403 (1989).
- [19] D. J. Wineland, W. I. Itano, and J. C. Bergquist, Opt. Lett. **12**, 389 (1987).
- [20] A. A. Madej and J. D. Sankey, Opt. Lett. **11**, 634 (1990).
- [21] S. Urabe, H. Imajo, K. Hayasaka, and M. Watanabe, J. Mod. Opt. **39**, 417 (1992).
- [22] H. A. Klein, A. S. Bell, G. P. Barwood, and P. Gill, Appl. Phys. B **50**, 13 (1990).
- [23] D. J. Larson, J. C. Bergquist, J. J. Bollinger, W. M. Itano, and D. J. Wineland, Phys. Rev. Lett. **57**, 70 (1986).
- [24] K. Bowe, L. Hornekær, C. Brodersen, M. Drewsen, and J. S. Hangst, Phys. Rev. Lett. **82**, 76 (1999).
- [25] Y. Kai, K. Toyoda, M. Watanabe, and S. Urabe, J. Appl. Phys. **40**, 5136 (2001).
- [26] M. Drewsen, Physica B **460**, 105 (2015).
- [27] T. Baba and I. Waki, J. Appl. Phys. **35**, L1134 (1996).
- [28] T. Baba and I. Waki, J. Chem. Phys. **116**, 1858 (2002).
- [29] K. Mølhave and M. Drewsen, Phys. Rev. A **62**, 011401 (2000).
- [30] M. Drewsen, A. Mortensen, R. Martinussen, P. Sta anum, and J. L. Sørensen, Phys. Rev. Lett. **93**, 243201 (2004).
- [31] E. K. Campbell, M. Holz, D. Gerlich, and J. P. Maier, Nature **523**, 322 (2015).
- [32] O. Asvany, M. K. Yamada, S. Bruken, A. Potapov, and S. Schlemmer, Science **347**, 1346 (2015).

- [33] B. Roth, P. Blythe, H. Wenz, H. Daerr, and S. Schiller, *Phys. Rev. A* **73**, 04271 (2006).
- [34] N. Kimura, K. Okada, T. Takayanagi, M. Wada, S. Ohtani, and H. A. Schuessler, *Phys. Rev. A* **83**, 033422 (2011).
- [35] L. Hornekær, Ph.D. thesis, University of Aarhus (2000).
- [36] M. Kajita, M. Abe, M. Hada, and Y. Moriwaki, *J. Phys. B: At. Mol. Opt. Phys.* **44**, 025402 (2011).
- [37] U. Bressel, A. Borodin, J. Shen, M. Hansen, I. Ernsting, and S. Schiller, *Phys. Rev. Lett.* **108**, 183003 (2012).
- [38] U. Flöhlich, B. Roth, P. Antonini, C. L. Ammerzahl, A. Wicht, and S. Schiller, *Lect. Notes Phys.* **648**, 297 (2004).
- [39] B. Roth, J. Koelemeij, S. Schiller, L. Hilico, and J. P. Karr, *Lect. Notes Phys.* **745**, 205 (2008).
- [40] B. Roth, J. C. J. Koelemeij, P. Blythe, H. Daerr, and S. Schiller, *Phys. Rev. A* **74**, 040501(R) (2006).
- [41] P. F. Sta anum, K. Højbjerg, P. S. Skyt, A. K. Hansen, and M. Drewsen, *N. J. Phys.* **11**, 055026 (2009).
- [42] N. B. Khanyile, G. Shu, and K. R. Brown, *Nature Commun.* **6**, 7825 (2015).
- [43] H. Loh, K. C. Cossel, M. C. Grau, K.-K. Ni, E. R. Meyer, J. L. Bohn, J. Ye, and E. A. Cornell, *Science* **342**, 1220 (2013).
- [44] A. E. Leanhardt, J. L. Bohn, H. Loh, P. Maletinsky, E. R. Meyer, L. C. Sinclair, R. P. Stutz, and E. A. Cornell, *J. Mol. Spec.* **270**, 1 (2011).
- [45] E. R. Meyer and J. L. Bohn, *Phys. Rev. A* **78**, 010502 (2008).
- [46] A. N. Petrov, N. S. Mosyagin, T. A. Isaev, and A. V. Titov, *Phys. Rev. A* **76**, 030501 (2007).
- [47] V. V. Flambaum, D. DeMille, and M. G. Kozlov, *Phys. Rev. Lett.* **113**, 103003 (2014).

- [48] D. E. Morrissey and M. J. Ramsey-Musolf, N. J. Phys. **14**, 125003 (2012).
- [49] M. D. Barrett, B. DeMarco, T. Schaetz, V. Meyer, D. Leibfried, J. Britton, J. Chiaverini, W. M. Itano, B. Jelenkovic, J. D. Jost, et al., Phys. Rev. A **68** (2003).
- [50] J. D. Jost, J. P. Home, J. M. Amini, D. Hanneke, R. Ozeri, C. Langer, J. J. Bollinger, D. Leibfried, and D. J. Wineland, Nature **459**, 683 (2009).
- [51] P. O. Schmidt, T. Rosenband, C. Langer, W. M. Itano, J. C. Bergquist, and D. J. Wineland, Science **309**, 749 (2005).
- [52] T. Rosenband, D. B. Hume, P. O. Schmidt, C. W. Chou, A. Brusch, L. Lorini, W. H. Oskay, R. E. Drullinger, T. M. Fortier, J. E. Stalnaker, et al., Science **319**, 1808 (2008).
- [53] C. W. Chou, D. B. Hume, J. C. J. Koelemeij, D. J. Wineland, and T. Rosenband, Phys. Rev. Lett. **104**, 070802 (2010).
- [54] C. R. Clark, J. E. Goeders, Y. K. Dodia, R. C. Viteri, and K. R. Brown, Phys. Rev. A **81**, 043428 (2010).
- [55] Y.-W. Lin, S. Williams, and B. C. Odom, Phys. Rev. A **87**, 011402 (2013).
- [56] D. B. Hume, C. W. Chou, D. R. Leibbrandt, M. J. Thorpe, D. J. Wineland, and T. Rosenband, Phys. Rev. Lett. **107**, 243902 (2011).
- [57] Y. Wan, F. Gebert, J. B. Wäbbena, N. Scharnhorst, S. Amairi, I. D. Leroux, B. Hemmerling, N. Lärch, K. Hammerer, and P. O. Schmidt, Nat. Commun. **5**, 3096 (2014).
- [58] C. F. Roos, Ph.D. thesis, University of Innsbruck (2000).
- [59] Y. Wan, F. Wolf, F. Gebert, and P. O. Schmidt, Phys. Rev. A **91**, 043425 (2015).
- [60] F. Wolf, Y. Wan, J. C. Heip, F. Gebert, C. Shi, and P. O. Schmidt, Nature **530**, 457 (2016).

- [61] J. H. V. Nguyen and B. Odom, Phys. Rev. A **83**, 053404 (2011).
- [62] J. H. V. Nguyen, C. R. Viteri, E. G. Hohenstein, C. D. Sherrill, K. R. Brown, and B. Odom, N. J. Phys. **13**, 063023 (2011).
- [63] E. S. Shuman, J. F. Barry, and D. DeMille, Nature **467**, 820 (2010).
- [64] M. T. Hummon, M. Yeo, B. K. Stuhl, A. L. Collopy, Y. Xia, and J. Ye, Phys. Rev. Lett. **110**, 143001 (2013).
- [65] X. Tong, A. H. Winney, and S. Willitsch, Phys. Rev. Lett. **105**, 143001 (2010).
- [66] P. F. Sta anum, K. Højbjørre, P. S. Skyt, A. K. Hansen, and M. Drewsen, Nat. Phys. **6**, 271 (2010).
- [67] T. Schneider, B. Roth, H. Duncker, I. Ernsting, and S. Schiller, Nat. Phys. **6**, 275 (2010).
- [68] C. Lien, C. Seck, Y. Lin, J. Nguyen, D. A. Tabor, and B. C. Odom, Nat. Commun. **5**, 4783 (2014).
- [69] A. K. Hansen, O. O. Versolato, L. Klosowski, A. Gingell, M. Schwarz, A. Windberger, J. Ullrich, L. Crespo, and M. Drewsen, Nature **508**, 76 (2014).
- [70] W. G. Rellergert, S. T. Sullivan, S. J. Schowalter, S. Kotochigova, K. Chen, and E. R. Hudson, Nature **495**, 490 (2013).
- [71] W. Paul, Rev. Mod. Phys. **62**, 531 (1990).
- [72] T. Jones, *Mathieu's equations and the ideal rf trap*, URL <http://www.physics.drexel.edu/~tim/open/mat/mat.pdf>.
- [73] D. Leibfried, R. Blatt, C. Monroe, and D. Wineland, Rev. Mod. Phys. **75**, 282 (2003).
- [74] H. J. Metcalf and P. v. d. Straten, *Laser Cooling and Trapping* (Springer-Verlag New York, Inc., 1999).
- [75] M. O. Scully and S. Zubairy, *Quantum optics* (Cambridge University Press, 1997).

- [76] M. Guggemos, D. Heinrich, O. Herrera-Sancho, R. Blatt, and C. Roos, *New J. Phys.* **17**, 103001 (2015).
- [77] L. R. Churchill, Ph.D. thesis, Georgia Institute of Technology (2010).
- [78] J. E. Goeders, C. R. Clark, G. Vittorini, K. Wright, R. C. Viteri, and K. R. Brown, *J. Phys. Chem. A* **117**, 9725 (2013).
- [79] N. B. Khanyile, Ph.D. thesis, Georgia Institute of Technology (2015).
- [80] J. E. Goeders, Ph.D. thesis, Georgia Institute of Technology (2013).
- [81] D. J. Berkeland, J. C. Miller, W. M. Itano, and D. J. Wineland, *J. Appl. Phys.* **83**, 5025 (1998).
- [82] H. C. Nägerl, C. Roos, D. Leibfried, H. Rohde, G. Thalhammer, J. Eschner, F. Schmidt-Kaler, and R. Blatt, *Phys. Rev. A* **61**, 023405 (2000).
- [83] G. Shu, G. Vittorini, A. Buikema, C. S. Nichols, C. Volin, D. Stick, and K. R. Brown, *Phys. Rev. A* **89**, 062308 (2014).
- [84] C. Roos, T. Zeiger, H. Rohde, H. C. Nägerl, J. Eschner, D. Leibfried, F. Schmidt-Kaler, and R. Blatt, *Phys. Rev. Lett.* **83**, 4713 (1999).
- [85] J. B. Wübena, S. Amairi, O. Mandel, and P. O. Schmidt, *Phys. Rev. A* **85**, 043412 (2012).
- [86] S. Schiller, D. Bakalov, A. K. Bekbaev, and V. I. Korobov, *Phys. Rev. A* **89**, 052521 (2014).
- [87] M. Germann, X. Tong, and S. Willitsch, *Nat. Phys.* **10**, 820 (2014).
- [88] M. Kajita, G. Gopakumar, M. Abe, M. Hada, and M. Keller, *Phys. Rev. A* **89**, 032509 (2014).
- [89] A. Eagle, *Astrophys. J.* **30**, 231 (1909).
- [90] A. A. Mills, B. M. Siller, M. W. Porambo, M. Perera, H. Kreckel, and B. J. McCall, *J. Chem. Phys.* **135**, 224201 (2011).
- [91] B. Roth, H. Wenz, H. Daerr, and S. Schiller, *Phys. Rev. A* **73**, 042712 (2006).

- [92] A. K. Hansen, M. A. Sørensen, P. F. Staantum, and M. Drewsen, *Angew. Chem. Int. Ed.* **51**, 7960 (2012).
- [93] M. Kajita and M. Abe, *J. Phys. B: At. Mol. Opt. Phys.* **45**, 185401 (2012).
- [94] M. Abe, M. Kajita, M. Hada, and Y. Moriwaki, *J. Phys. B: At. Mol. Opt. Phys.* **43**, 245102 (2010).
- [95] M. Aymar and O. Dulieu, *J. Phys. B: At. Mol. Opt. Phys.* **45**, 215103 (2012).
- [96] M. Abe, Y. Moriwaki, M. Hada, and M. Kajita, *Chem. Phys. Lett.* **521**, 31 (2011).
- [97] H. Habli, H. Ghalla, B. Oujia, and F. Gadéa, *Eur. Phys. J. D* **64**, 5 (2011).
- [98] K. Matsubara, K. Hayasaka, Y. Li, Y. Ito, S. Nagano, M. Kajita, and M. Hosokawa, *App. Phys. Exp.* **1**, 067011 (2008).
- [99] K. Mori, T. Yusuke, M. Obara, and K. Midorikawa, *J. Appl. Phys.* **83**, 2915 (1998).
- [100] V. Krylov, A. Rebane, A. G. Kalintsev, H. Schwöerer, and U. P. Wild, *Opt. Lett.* **20**, 198 (1995).
- [101] R. J. L. Roy, University of Waterloo Chemical Physics Research Report **CP-663** (2014).
- [102] J. Nelder and R. Mead, *Comput. J.* **7**, 308 (1965).
- [103] R. O'Neill, *J. Appl. Stat.* **20**, 338 (1971).
- [104] I. R. Bartky, *J. Mol. Spec.* **20**, 299 (1966).
- [105] A. Pardo, J. J. Camacho, J. M. L. Potayo, and E. Martín, *Chem. Phys.* **117**, 149 (1987).
- [106] W. C. Stwalley, W. T. Zemke, and S. C. Yang, *J. Phys. Chem. Ref. Data* **20**, 153 (1991).

- [107] C. Carlsund-Levin, N. Elander, A. Nunez, and A. Scrinzi, *Physica Scripta* **65**, 306 (2002).
- [108] R. Rugango, J. E. Goeders, T. H. Dixon, J. M. Gray, N. Khanyile, G. Shu, R. J. Clark, and K. R. Brown, *New. J. Phys.* **17**, 035009 (2015).
- [109] O. O. Versolato, M. Schwarz, A. K. Hansen, A. D. Gingell, A. Windberger, L. Klosowski, J. Ullrich, F. Jensen, L. Crespo, and M. Drewsen, *Phys. Rev. Lett.* **111**, 053002 (2013).
- [110] A. D. Ludlow, M. M. Boyd, J. Ye, E. Peik, and P. Schmidt, *Rev. Mod. Phys.* **87**, 637 (2015).
- [111] M. S. Safronova, M. G. Kozlov, and C. W. Clark, *IEEE Trans. Ultrason., Ferroelect., Freq. Control* **59**, 439 (2012).
- [112] A. Müller, S. Schippers, R. A. Phaneuf, A. L. D. Kilcoyne, H. Bräuning, A. S. Schlachter, M. Lu, and B. M. McLaughlin, *J. Phys. B: At. Mol. Opt. Phys.* **43**, 225201 (2010).
- [113] T. Aoyamal, M. Fukudal, Y. Wall, Nara, S. Umisedo, N. Hamamoto, M. Hinds, Tanjo, and T. Nagayama, in *Proc. Int. Workshop Junction Technol.* (2005), pp. 27–30.
- [114] S. Mukherjee and P. Thilagar, *Chem. Commun* **52**, 1070 (2016).
- [115] L. Hanley and S. L. Anderson, *J. Phys. Chem* **91**, 5161 (1987).
- [116] M. B. Sowa-Resat, J. Smolanoff, A. Lapicki, and S. L. Anderson, *J. Chem. Phys.* **106**, 9511 (1997).
- [117] S. A. Ruatta, L. Hanley, and S. L. Anderson, *J. Chem. Phys.* **91**, 226 (1989).
- [118] K. Zimmermann, M. V. Okhapkin, A. Herrera-Sancho, and E. Peik, *Appl. Phys. B* **107**, 883889 (2012).
- [119] T. Baba and I. Waki, *Phys. Rev. Lett.* **89**, 4592 (2001).
- [120] P. Blythe, B. Roth, U. Fröhlich, H. Wenz, and S. Schiller, *Phys. Rev. Lett.* **95**, 183002 (2005).

- [121] V. L. Ryjkov, X. Zhao, and H. A. Schuessler, Phys. Rev. A **74**, 023401 (2006).
- [122] K. Højbjerg, D. Offenberger, C. Z. Bisgaard, H. Stapelfeldt, P. F. Staunum, A. Mortensen, and M. Drewsen, Phys. Rev. A **77**, 030702 (2008).
- [123] B. Roth, Blythe, and S. Schiller, Phys. Rev. A **75**, 023402 (2007).
- [124] K. Pyka, N. Herschbach, J. Keller, and T. E. Mehlstäubler, Appl. Phys. B **114**, 231 (2014).
- [125] J. Nichols, M. Gutowski, S. J. Cole, and J. Simons, J.Phys.Chem. **96**, 644 (1992).
- [126] V. Dryza, B. L. J. Poad, and E. J. Bieske, J.Phys.Chem. **130**, 12986 (2008).
- [127] P. P. Pronko, P. A. VanRompay, Z. Zhang, and J. A. Nees, Phys. Rev. Lett. **83**, 2596 (1999).
- [128] M. Joseph and P. Manoravi, Appl. Phys. A **76**, 153156 (2003).
- [129] D. R. Ride, ed., *CRC Handbook of Chemistry and Physics* (CRC Press, Inc., 1992-1993).
- [130] C. Ottinger and J. Reichmuth, J. Chem. Phys. **74**, 928 (1981).
- [131] R. C. Viteri, A. T. Gilkison, and E. R. Grant, J. Chem. Phys. **136**, 214312 (2012).
- [132] T. J. Tague and L. Andrews, J. Am. Chem. Soc. **116**, 4970 (1994).
- [133] S. Amoruso, R. Bruzzese, N. Spinelli, and R. Velotta, J. Phys. B: At. Mol. Opt. Phys. **32**, R131 (1999).
- [134] C. Yang and Z. Zhu, J. Mol. Struct. **571**, 225 (2001).
- [135] C. Yang, Z. Zhu, R. Wang, and X. Liu, J. Mol. Struct. **548**, 47 (2001).
- [136] S. J. Schowalter, K. Chen, W. G. Rellergert, S. T. Sullivan, and E. R. Hudson, Rev. Sci. Instrum. **83**, 043103 (2012).

- [137] I. Labazan, N. Krstulović, and S. Milošović, Chem. Phys. Lett. **428**, 13 (2006).
- [138] T. Oksenhendler and N. Forget, *Pulse-Shaping Techniques Theory and Experimental Implementations for Femtosecond Pulses* (2010).
- [139] A. M. Weiner, J. P. Heritage, and E. M. Kirschner, Opt. Soc. Am. B **5**, 63 (1988).
- [140] A. M. Weiner, Rev. Sci. Instrum. **71**, 1929 (2000).
- [141] N. B. Delone and V. P. Krainov, Physics-Uspekhi **42**, 669 (1999).
- [142] D. J. Wineland, C. Monroe, W. M. Itano, D. Leibfried, B. E. King, and D. M. Meekhof, J. Res. Natl. Inst. Stand. Technol. **103**, 259 (1998).
- [143] K. G. Tschersich, J. P. Fleischhauer, and H. Schuler, J. Appl. Phys. **104**, 034908 (2008).
- [144] M. G. Kokish, M. R. Dietrich, and B. C. Odom, J. Phys. B: At. Mol. Opt. Phys. **49**, 035301 (2016).
- [145] R. J. Hendricks, D. A. Holland, S. Truppe, B. E. Sauer, and M. R. Tarbut, arXiv:1404.6174v2 [physics.atom-ph] (2014).
- [146] C. for Disease Control and Prevention, *Diborane*, URL <http://www.cdc.gov/niosh/ipcsneng/neng0432.html>.
- [147] V. Zhelyazkova, A. Cournol, T. E. Wall, A. Matsushima, J. J. Hudson, E. A. Hinds, M. R. Tarbutt, and B. E. Sauer, Phys. Rev. A **89**, 053416 (2014).
- [148] J. C. J. Koelemeij, B. Roth, and S. Schiller, Phys. Rev. A **76**, 023413 (2007).
- [149] S. Kahra, G. L. Leschhorn, M. Kowalewski, A. Schiffrin, E. Bothschafter, W. Fusz, R. de Vivie-Riedle, R. Ernstorfer, F. Krausz, R. Kienberger, et al., Nat. Phys. **8**, 238 (2012).